Study of new porous materials by NMR

Shrikant Kunjir

Normandie Université

THESE

Pour obtenir le diplôme de doctorat

Spécialité Chimie

Préparée au sein de l'ENSICAEN et de l'UNICAEN

Study of new porous materials by NMR

Présentée et soutenue par
Shrikant KUNJIR

Thèse soutenue publiquement le 17 janvier 2018 devant le jury composé de		
Mme MARTINEAU-CORCOS Charlotte	Maître de Conférence-HDR, Université de Versailles Saint-Quentin-en-Yvelines	Rapporteur
M. LE POLLES Laurent	Maître de Conférence-HDR, Institut des Sciences Chimiques de Rennes	Rapporteur
M. FAYON Franck	Directeur de Recherche CNRS, CEMHTI Orléans	Examinateur
Mme MINTOVA Svetlana	Directeur de Recherche CNRS, Université de Caen Normandie	Examinateur
Mme VICENTE Aurélie	Maître de Conférence, Université de Caen Normandie	Examinateur
M. FERNANDEZ Christian	Professeur des Universités, Université de Caen Normandie	Directeur de thèse

Thèse dirigée par Christian FERNANDEZ, Laboratoire Catalyse et Spectrochimie (LCS)

UNIVERSITÉ CAEN NORMANDIE

ENSICAEN
ÉCOLE PUBLIQUE D'INGÉNIEURS
CENTRE DE RECHERCHE

ED 508

LCS

Abstract

Study of novel porous materials by ^{129}Xe NMR

The zeolites are 'molecular sieves' known for their numerous applications in adsorption, ion exchange, and catalysis. In this thesis, we focused on the study of some questions related to zeolite synthesis and post-synthesis, which are not yet resolved by other techniques. NMR was the primary tool in this work, as it gives access to local structural information on nanocrystals even when diffraction techniques found their limits. NMR can also be used to study porosity using probe molecules adsorption, and in particular, xenon is known as a good molecule for this purpose. Indeed, the isotope ^{129}Xe can be hyperpolarized to increase the detection sensitivity, and interestingly it presents a wide chemical shift range depending on its confinement and thus the porosity of studied material. Two studies are reported in this manuscript: (i) In the first study, the initial steps during the crystallization of nano-faujasite (FAU) type materials were investigated using classical NMR (mainly by ^{29}Si and ^{23}Na MAS NMR) and advanced NMR (^{129}Xe HP NMR). It was shown that crystallization starts at much earlier synthesis stages than those observed by other classical techniques (XRD, SEM, N_2 adsorption...). The first SBU seems to be the hexagonal prisms, prior to the sodalite cages, which rapidly form confined environment and then supercages. Moreover, it has been proved by ^{129}Xe HP NMR and 2D EXSY that nano-faujasite zeolite presents opened sodalite cages and a more flexible structure than in micro-faujasite zeolite. (ii) The second study is an investigation on the recrystallization phenomena occurring during hierarchization process of zeolite and which could explain the homogenous distribution of the mesopore sizes. As a remarkable result, it has been shown in this work that during the hierarchization of beta zeolite with TPAOH, the recrystallization lead to the formation of tiny MFI particles, formed at the surface of the mesopores (^{1}H MAS NMR, ^{129}Xe HP NMR and 2D EXSY).

Key words: Zeolite, Porosity, Structure, Solid-state NMR, ^{129}Xe NMR, hyperpolarization, 2D EXSY.

Résumé

Etude de nouveaux matériaux poreux par Résonance Magnétique Nucléaire du ^{129}Xe

Les zéolites sont des «tamis moléculaires» connus pour leurs nombreuses applications en adsorption, échange d'ions et catalyse. Dans cette thèse, nous nous sommes concentrés sur l'étude de quelques questions liées à la synthèse et à la post-synthèse de la zéolithe, qui ne sont pas encore résolues par d'autres techniques. La RMN a été l'outil principal dans ce travail, donnant accès à des informations structurales locales sur les nanocristaux même lorsque les techniques de diffraction trouvent leurs limites. Elle peut également être utilisée pour étudier la porosité en utilisant l'adsorption de molécules sondes, et en particulier, le xénon est connu comme une bonne molécule pour cet objectif. En effet, l'isotope ^{129}Xe peut être hyperpolarisé pour augmenter la sensibilité de détection, et il présente une large plage de déplacement chimique en fonction du confinement et donc de la porosité du matériau étudié. (I) Dans la première étude, les étapes initiales de la cristallisation de nano-faujasite (FAU) ont été étudiées en utilisant la RMN classique (principalement par ^{29}Si and ^{23}Na MAS RMN) et la RMN avancée (^{129}Xe). RMN HP). Il a été montré que la cristallisation commence à des stades de synthèse bien antérieurs à ceux observés par d'autres techniques classiques (XRD, SEM, adsorption de N_2 ...). La première SBU semble être les prismes hexagonaux, avant les cages sodalite, qui forment rapidement un environnement confiné puis des supercages. De plus, il a été démontré par RMN ^{129}Xe HP et 2D EXSY que la zéolithe nano-faujasite présente des cages sodalite ouvertes et une structure plus souple que dans la zéolite de type micro-faujasite. (ii) La seconde étude est une recherche sur les phénomènes de recristallisation survenant au cours du processus de hiérarchisation de la zéolithe et qui pourrait expliquer la distribution homogène des tailles de mésopores. Comme résultat remarquable, il a été montré dans ce travail que lors de la hiérarchisation de la zéolithe bêta avec le TPAOH, la recristallisation conduisait à la formation de minuscules particules de MFI, formées à la surface des mésopores (RMN ^{1}H MAS, RMN ^{129}Xe HP et 2D EXSY).

Key words: Zeolithes, Porosité, Structure, RMN à l'état solide, RMN du ^{129}Xe, hyperpolarisation, 2D EXSY.

Résumé

Etude de nouveaux matériaux poreux par Résonance Magnétique Nucléaire du Xenon-129

Ce travail s'inscrit dans une recherche constante des premières étapes de synthèse de certaines structures zéolithiques (ici la faujasite) ainsi que la modification de la porosité (ici la BEA) pour des applications spécifiques. En effet lors de la synthèse de zéolithes, les premiers maillons de formation de la structure restent parfois au cœur de beaucoup de débat scientifiques, bien que la structure finale soit bien connue depuis plusieurs décennies.

Les zéolithes sont de matériaux poreux présentant une microporosité inférieure à 2 nm très employées dans l'industrie pour des propriétés de sélectivité de forme lors de réactions catalytiques conduisant à la formation de différents composés organiques, ou de stockage et/ou séparation de différentes molécules. Dans beaucoup de ces applications, la taille même des cristaux de zéolithe, souvent de l'ordre du micromètre, présente un inconvénient qui est lié à la diffusion des molécules à l'intérieur des cristaux. Ce problème de diffusion conduit à la désactivation du matériaux ou à de plus faible capacité d'adsorption de molécule au cœur de celui-ci, comparé à celle de sa surface. Une des possibilités est de contrôler, lors de la synthèse, la taille des cristaux et former des nano-cristaux. L'autre est de modifier les gros cristaux (couramment obtenus dans les synthèses commerciale) en incorporant une mesoporosité (2nm $<$ meso $<$50nm) pour diminuer le chemin diffusionnel des molécules.

Il faut aussi noter que les zéolithes sont généralement des aluminosilicates où la présence d'aluminium dans la structure crée une charge négative impérativement compensée par (a) un proton pour lui donner des propriétés acides ou par (b) des cations alcalins (tels que : Li, Na, K, Rb ou Cs) qui apportent alors différentes propriétés d'adsorption. Les différentes structures les plus utilisées dans l'industrie sont la structure faujasite, noté X ou Y en fonction de la teneur en aluminium, qui présente une porosité d'environ 1 nm.

Ici l'objectif est aussi d'avoir une analyse avancée, dès l'échelle nanométrique, de la structure des zéolithes. Il est connu que la RMN permet de déterminer l'environnement local des noyaux étudiés. Ainsi, l'analyse de certains noyaux comme le silicium (^{29}Si) et le sodium (^{23}Na) permet de remonter indirectement à la structure environnante. De plus, la technique de caractérisation de la porosité, connue sous le nom de ^{129}Xe hyperpolarisé, qui a été récemment développé

au laboratoire, s'adapte parfaitement à ces problématiques et les résultats obtenus démontrent l'intérêt important de cette technique.

Ce travail est divisé en deux parties :

1. La première partie porte sur (i) la caractérisation en continue lors de la synthèse d'une nano-faujasite, (ii) la localisation des différents cations après échange et (iii) la comparaison entre ces premières observations obtenues pour la nano-faujasite et d'autres nano-structures contenant les mêmes unités secondaire de construction SBU (secondary building units), c'est-à-dire une cavité sodalite.

   i) Dans cette section, nous nous sommes intéressés aux premières étapes de synthèse de matériaux de taille nanométrique (cristaux $<$ à 50 nm). Les différentes techniques de caractérisation des matériaux (notamment la DRX) nous ont permis de suivre la cinétique de formation des premiers cristaux afin de déterminer l'étape où la structure commence à s'édifier. Une étude plus poussée par RMN des différents noyaux de la structure (^{23}Na et ^{29}Si) viennent renforcer les premières observations et éclairer sur le premier maillon formé dans l'édifice. Toutefois seule la caractérisation par ^{129}Xe hyperpolarisé nous a permis de mettre en évidence qu'une porosité se forme bien avant qu'elle ne soit observable par des méthodes classiques. De plus, la structure de taille nanométrique présente une plus grande flexibilité que lorsque les cristaux sont de l'ordre du μm.

   ii) Des échanges cationiques sur cette même structure ont été possible sans détruire ni la structure ni la taille nanométrique de la faujasite. De plus la RMN du ^{23}Na et l'analyse par ^{129}Xe hyperpolarisé ont mis en évidence des résultats différents de la littérature lorsque l'échange se fait sur des cristaux micrométriques. Ainsi la localisation même des différents cations dépend du paramètre nanométrique des cristaux et peut donc conférer de nouvelles propriétés au matériau.

   iii) Enfin plusieurs structures possédants la même unité secondaire d'édifice (SBU secondary building units), *i.e.*, la sodalite dans SOD, LTA, FAU-X, FAU-Y et EMT ont fait l'objet d'une étude similaire. Une cavité sodalite est présente dans chacune de ces structures. La SOD ne possède que des cavités de type sodalite. Pour les autres structures, une seconde cavité de taille croissante est présente dans l'ordre LTA, FAU et EMT. L'échelle nanométrique de ces différentes zéolithes a conduit à observer les mêmes phénomènes que ceux observés dans la section i).

2. La seconde partie porte sur la modification d'une autre structure zéolithique, la zéolithe BEA, par incorporation de mesoporosité lors d'un post traitement du matériaux. En effet, il a déjà été démontré qu'il était possible de dissoudre une partie de la structure en créant des « trous » plus gros qui ont pour effet de diminuer le parcours moyen des molécules à travers la zéolithe. Les agents utilisés le plus souvent sont des solutions basiques types NaOH. Ici lors de la dissolution, un agent structurant est introduit (TPAOH) qui peut aussi être un agent structurant lors de la synthèse de zéolithes. Les différentes analyses montrent la formation de mesoporosité. Seules les expériences menées par RMN (1H NMR et 129Xe hyperpolarisé) ont mis en évidence la présence d'une nouvelle phase (probablement de la zéolithe MFI) déposée à la surface des mésopores par recristallisation du Si autour du cation TPA^+.

Acknowledgements

First and foremost I start with my supervisor Prof.Christian Fernandez for being very kind and supportive throughout these years of research. I must remember the early time when I had a trouble with Visa and who supported me to write Indian Embassy to sort out this issue otherwise this day never come in my life. In spite of his busy schedules, he always took time for guiding and helping me whenever needed. He is highly knowledgeable and experienced person. I feel very fortunate to get a chance to work with him.

I wanted to thank Dr.Aurélie Vicente who not only encouraged me for thesis but also built my confidence. Her encouragement and guidance during the final preparation of this thesis is overwhelming. Her advice on both research as well as on my career have been invaluable. And indeed, I will be going out to the professional world as a much more confident person than before.

I must thank Dr.Hussein Elsiblani and Baptiste Rigaud who taught me Xenon polarizer instrument in details with all the scientific principle involved in the process. Especially Dr.Hussein Elsiblani who gave me all the necessary technical advice and safety precautions working with gases and laser, with filling the rubidium in SEOP cell and to handle it. I must also thank Dr.Eddy Dib whose scientific advice and discussions were always productive. His jokes and fun in the lab are unforgettable. I also thank all my friends from the LCS, Caen. Thanks to our collaborators Dr. Hussein Awala, Dr.Ana Palcic, Dr.Sarah Komaty, Prof.Svetlana Mintova and Prof.Valentin Valtchev from LCS Caen and Dr.Danny Verboekend K.U. Leuven for zeolite samples. I would like to thank Universite de Caen for financial support for my doctoral thesis.

The very first NMR experiment I did was with Dr. P. R. Rajamohanan (NCL Pune), during my project assistant work in NMR. I would like to express my sincere gratitude to him. I would also like to thank Dr. T. G. Ajithkumar and Dr. Sapna Ravindranathan for their help, suggestions while working in NMR lab.

I would like to thank Dr. S. Ganapathy for his lectures on NMR theory; his guidance and support help me to get motivated for Ph.D. thesis. I would like to thank all the friends from previous research lab, NCL Pune (India).

Finally, my parents cannot be thanked enough for giving me the best education they could afford in their circumstances. I am very thankful to my family who motivated me to follow footsteps in science and research. Last but not the least, my gratitude also extends to my wife Vaishali Kunjir whose food and warmth helped me to combat the French weather.

Shrikant Kunjir

Contents

As the field of zeolite science is continually growing, due to its application in both industry and academic research. Among the various approaches used to study these systems, the techniques of magnetic resonance, in particular, nuclear magnetic resonance (NMR) have a special place because of their unique ability to elucidate the structure, dynamics, and function at the atomic and molecular level. Over the past years, countless NMR techniques have been developed to study complex organic, inorganic, and biological solid materials.

Unfortunately, "The sensitivity of conventional NMR techniques is fundamentally limited by the ordinarily low spin polarization achievable in even the strongest NMR magnets". In certain systems, however, the sensitivity of NMR spectroscopy and magnetic resonance imaging (MRI) can be greatly enhanced via optical pumping. In optical pumping, angular momentum can be transferred from laser photons to electronic and nuclear spins, thereby transiently enhancing the nuclear spin polarization in these systems by four to five orders of magnitude.

Keeping in mind the above challenges faced by the research communities, we the researchers at Catalysis and Spectrochemistry Laboratory (LCS), Caen has designed their own homebuilt xenon polarizer system, to follow the influence of porosity on the deactivation and reactivation of zeolite catalysts. As the ^{129}Xe NMR spectroscopic investigation of adsorbed xenon (Xe) atoms is a suitable method for the study of the pore architecture of molecular sieves.

The overall structure of the thesis takes the form of three chapters. Chapter 1 deals with the basics of hyperpolarized (HP) Xe NMR, its instrumentation details, applications and challenges involved in this technique.

Chapter 2 deals with the application of HP Xe NMR to study synthetic nano zeolites. This chapter is divided into three parts. Part A: A study of the crystallization mechanism of nanosized FAU-X zeolites by HP Xe NMR. Part B: A study of the effect of cation substitution (IA group) on the adsorption of Xe on nanosized FAU-X zeolite by HP Xe NMR.

Chapter 3 deals with recrystallization on alkaline treated beta (BEA) zeolite in presence of (TPA^+) pore directing agents. In this chapter, using mainly HP ^{129}Xe and ^{1}H NMR, we showed new information on the recrystallization mechanisms occurring during the mesopores formation in zeolites.

Chapter 1

Overview of Xenon NMR

1.1 Introduction

Ramsay and Travers discovered xenon in 1898.[1] Xenon is *d* block element having atomic number 54. Its electronic configuration is $[Kr]4d^{10}\ 5s^2\ 5p^6$.

As xenon is a noble gas, its external electronic orbital is completely occupied and that it is chemically inert. At standard temperature and pressure, xenon exists as a colorless and odorless gas. Commercially, it is often used in gas discharge lamps. Xenon is soluble to certain amount in many liquids and in non-polar organic solvents. It is soluble in aqueous solutions and emulsions.[2] As xenon dissolves in blood, hyperpolarized ^{129}Xe is promising for NMR imaging and spectroscopic applications, particularly for the brain and biological systems .[3]

Loewenstein and Brenman were the first who used xenon NMR for the investigation of liquid-crystalline systems in 1978.[4] There are 8 stable isotopes and over 40 unstable radioactive isotopes of xenon exist. Out of this 8 stable isotopes, only two have non-zero spin and thus can be studied using NMR: ^{129}Xe with I=1/2 and ^{131}Xe with I=3/2. The choice of ^{129}Xe isotope is easier to study as compared with ^{131}Xe because the latter is quadrupolar leaving some complication in NMR, e.g., regarding relaxation.[5]

In our work on porous materials, we have used only the^{129}Xe isotopes. It has been already proved to be an excellent atomic probe for NMR of such materials. For this purpose, it was first used in 1982 by Fraissard and Ito.[6] Due to its large electron cloud and large polarizability, the chemical shift of xenon is very sensitive to its chemical and physical environments, and can vary over several thousands of ppm. When xenon is adsorbed on microporous and mesoporous materials, its chemical shift ranges from 0 to 250 ppm with respect to the free gas, depending on the temperature, pressure and pore size. The signal of the gas phase is generally used as a chemical shift reference. In order to increase the sensitivity and speed-up the NMR experiments (in particular experiments such as two-dimensional exchange NMR spectroscopy), the use of hyperpolarization for signal enhancement is often necessary. This will be discussed below.

1.2 Methods for Hyperpolarization of Noble Gases

NMR spectroscopy is one of the most useful and powerful technique for probing the molecular structure with high resolution in both solid and solution state since many years. But the technique itself suffers inherently from low sensitivity owing to the extremely small energy separation existing between nuclear spin states in the presence of static magnetic field of NMR spectrometer.[7]

The process of significant polarization enhancement, well above that achieved at thermal equilibrium, is called hyperpolarization. This includes the use of sensitivity enhancing pulse sequences, higher magnetic fields, cryogenic cooled probes, ...[7] The main hyperpolarization techniques are reported in Scheme 1.1. With these techniques, NMR sensitivity can be enhanced by a factor of several orders of magnitude[9,10] for a wide range of nuclei including ^{1}H,[11] ^{3}He,[12] ^{13}C,[13] ^{15}N,[14] ^{83}Kr,[15] and ^{129}Xe.[16]

Hyperpolarized noble gases are typically used in Magnetic Resonance Imaging (MRI) of the lungs.[17] In case of metabolic imaging hyperpolarized small molecules are used, e.g., to track the metabolic conversion in real time, hyperpolarized metabolite can be injected into animals or patients.[18] In the case of materials study, the hyperpolarization of ^{129}Xe has been introduced in the group of Prof. Alexander pines lab at Berkeley in early 1991. The first experiment was conducted on graphitized carbon and on powder benzanthracene in which ^{129}Xe relaxation time and signal enhancement was studied.[19] Following work on ^{129}Xe was on thin film, where xenon frozen onto the surfaces of glass sample cells proved the line shape of adsorbed xenon signal

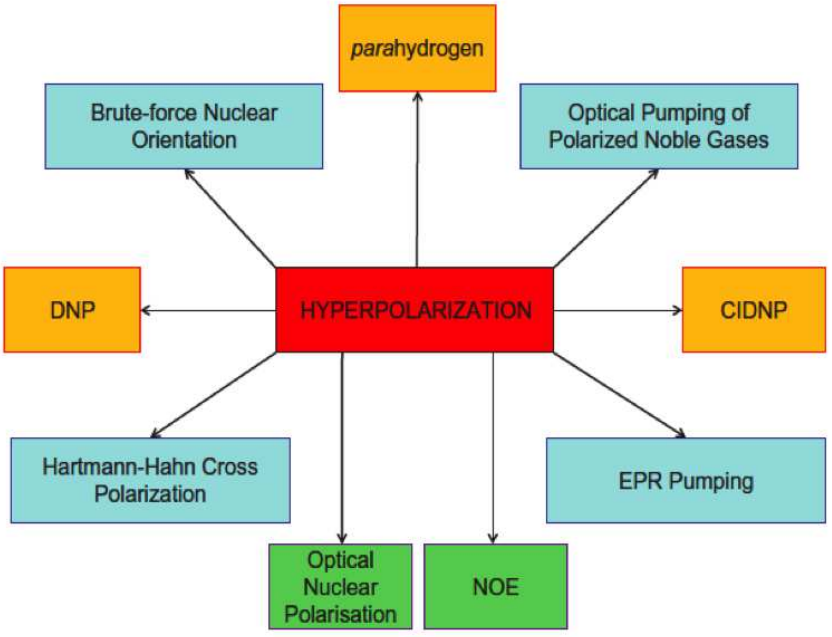

Scheme 1.1: Methods used for hyperpolarization transfer. Scheme adapted from ref.[8]

depends on film geometry.[20] Later, optically pumped ^{129}Xe NMR technique proved various applications in materials science.[21–23] Such as, to study the TiO_2 (anatase)- V_2O_5 catalyst with different loading of V_2O_5[24] and to probe the surface of Cds nanocrystal[25] studied by variable temperature ^{129}Xe hyperpolarization.

Hyperpolarization of noble gases can be achieved using a number of techniques including Brute Force polarization (BF), Dynamic nuclear polarization (DNP) or with Spin-Exchange of Optical Pumped (SEOP) alkali atoms.

1.2.1 Brute Force Hyperpolarization

Brute Force is the most straightforward method for producing a hyperpolarized state.[26] In the brute-force method, the nuclear magnetic sublevels are split by the application of an external magnetic field, and the nuclear spin temperature is lowered by establishing thermal equilibrium with the suitable thermal reservoir, so that the population differences given by the Boltzmann distribution appear between the sublevels.[27] For example by cooling down the sample to liquid helium temperature (4 K) at a field strength of 20 T, the polarization is increased by a factor of 1000.[28] John Owers-Bradley and co-workers used brute-force method as a method for the production of hyperpolarized HP-^{129}Xe gas.[29] This experiment was performed with a temperature of 10 mK and at 15.5 T magnetic field, and the obtained polarization was $\sim$ 41 % for ^{129}Xe.[29] This approach is however time consuming, and so further development are needed to reduce the longitudinal relaxation T_1 at very low temperature and to maintain the polarization state once the xenon has returned to room temperature.[30]

1.2.2 Dynamic Nuclear Polarization (DNP)

Dynamic Nuclear Polarization (DNP) consist of transfer of the polarization from highly polarized unpaired electrons to nuclear spins, mostly to protons of solvent molecules in the vicinity of electrons.[31] Due to their high magnetogyric ratio electrons are polarized to a much higher degree than nuclear spins at the same temperature and magnetic field strength. The polarization transfer takes place during irradiation with microwaves near or at the electronic paramagnetic resonance (EPR) frequency of the electrons.[32] Because most samples do not contain unpaired electrons, a doping of samples with radicals is necessary (often nitroxide or triaryl radicals are used)[33] The use of DNP, for the hyperpolarization of ^{129}Xe at room temperature, was proposed by Comment *et al.*[34] To hyperpolarize ^{129}Xe with this method, it has to be mixed in a glassy frozen matrix containing molecules with unpaired electron spins (*e.g.*, a stable radical or photoinduced radical). The matrix is placed at very low temperature (1 K) and at high magnetic field. Hence, the unpaired electrons obtain a near-unity spin polarization. The matrix is then

irradiated with microwaves in order to drive the high-spin polarization to the surrounding nuclei in the matrix allowing a high bulk nuclear spin polarization to accumulate over time. The matrix is then rapidly warmed, sublimating the xenon as a pure gas. Therefore, the technique is referred as "sublimation DNP".[35] With this approach, polarization enhancement of $\sim 30\%$ have been achieved in ~ 1.5 h.[35]

1.2.3 Spin Exchange with Optical Pumped Alkali-Metals

Both the two above-described methods are elegant, but none of them is widely used, until now. The most commonly used method for generating HP noble gases is the so-called Spin Exchange Optical Pumping (SEOP) technique. The pioneer of SEOP method was Kastler,[36] who was recognized with the Nobel Prize in physics for demonstrating that electronic spin order can be created in alkali metal vapors using circularly polarized laser light. Further this technique has been extensively explored by Happer, Cates, Walker[37–40] and many others for producing the large quantities of HP noble gases with very high nuclear spin polarization levels. This method will be explained in the following section.

1.3 Spin Exchange Optical Pumping (SEOP)

1.3.1 Introduction

The SEOP technique, which allows the production of gas with high polarization in large volumes, is a two steps process. In the first step, photon angular momentum is transferred from a circularly polarized laser light to the electron spins of an alkali metal vapor as shown in figure 1.1. To accomplish this, it is essential that the alkali atoms, usually Rb, are optically pumped in magnetic field at the wavelength (λ_{D1} =794.76 nm) of their D1 transitions ($5^2S_{1/2} \rightarrow 5^2P_{1/2}$). In a second step, these highly spin polarized Rb atoms are brought in contact with noble gas atoms (*e.g.*,^{129}Xe).[12] During this process, there is a transfer of polarization from the electron to the nuclear spin through a Fermi contact interaction. After this transfer, the depolarized Rb atoms are then continuously repolarized by optical pumping and the process repeats while the ^{129}Xe polarization built up.

Inside the SEOP production cell, there are numerous thermodynamics phenomena taking place[42]. Basically, under this steady state conditions, the ^{129}Xe polarization P_{Xe} can be written as ,

$$P_{Xe} = \frac{\gamma_{SE}}{\gamma_{SE} + \Gamma_{Xe}} P_{Rb} \tag{1.1}$$

where Γ_{Xe} is the ^{129}Xe relaxation rate and γ_{SE} is the spin exchange rate, which depends on the particular Rb-^{129}Xe gas combination used, and in particular on the density of Rb. For ^{129}Xe, the spin exchange rate γ_{SE} is pressure dependent. At high pressure, these interactions are dominated by binary collisions and, at low pressure, by the successive formation and break up of van der Waals molecules.[40]

P_{Rb} is the Rb polarization given by,

$$P_{Rb} = \frac{\gamma_{opt}}{\gamma_{opt} + \Gamma_{SD}} \tag{1.2}$$

Γ_{SD} is the electron spin polarization destruction rate, which depends on the gas density and composition. The major effects causing electron spin destruction apart from wall relaxation are Rb-Rb, Rb-Xe, Rb-He and Rb-N_2 collisions.[43–45] γ_{opt} is the optical pumping rate which is given as,

$$\gamma_{opt} = \int I(\nu)\sigma(\nu)d\nu \tag{1.3}$$

where $I(\nu)$ is the photon flux at frequency ν and $\sigma(\nu)$ is the photon absorption cross section for the D1 electronic transition in Rb.

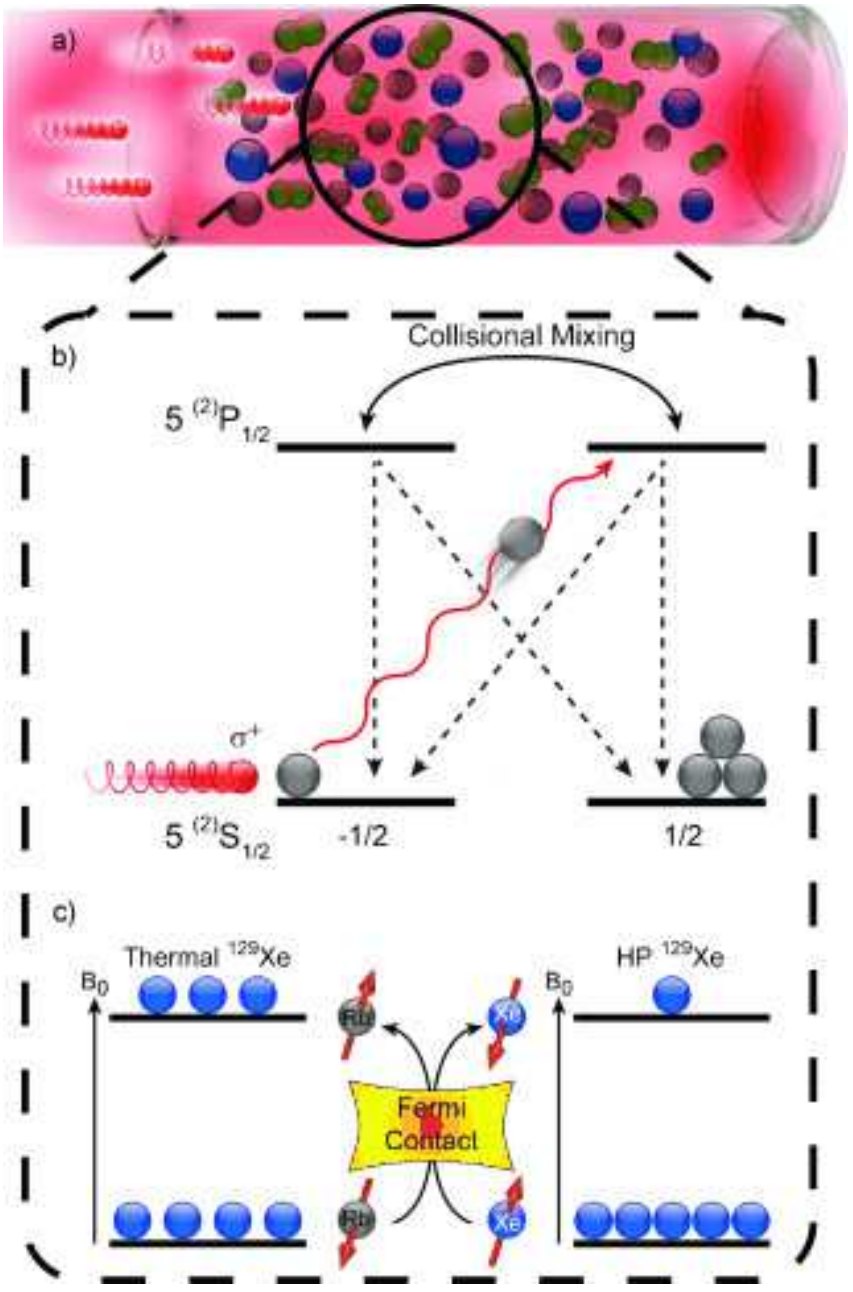

FIGURE 1.1: Schematic representation of SEOP method (a) SEOP cell with a mixture of a noble gas (Xe) , buffer gases (N2) and small quantity of vaporised alkali metal (Rb); the cell is irradiated by circularly polarized laser light that can be absorbed by alkali metal atoms. (b) First step of SEOP process, where angular momentum is transferred from circularly-polarized photons of light to alkali metal electrons (Rb) with optical pumping method from ground electronic state to excited state $^2S_{1/2}$ $\rightarrow$ $^2P_{1/2}$ (c) Second step of SEOP process where hyperpolarization of xenon take place by Rb-Xe spin exchange via fermi contact hyperfine interactions. Figure adapted from reference [41]

From the above equations, we can conclude that in order to achieve the highest P_{Xe}, three conditions need to be met:[46]

1. minimizing the alkali electron relaxation and ^{129}Xe nuclear relaxation
2. maximizing the absorbed photon flux
3. maximizing the spin exchange rate.

To maximize the polarization, there are numerous practical factors affecting the design of the polarizing system which needs to take into consideration. The pump cell design and its shape, the pump cell temperature which will be used during the experiment, the laser power and the gas mixture which used inside the pump cell.[47]

1.3.2 Instrumentation

As we have seen in previous section, the level of polarization depends on various experimental factors.[48] Therefore, one has to consider these factors during the design of Spin Exchange Optical Pumping - (SEOP) apparatus. There are various designs of apparatus for polarization by SEOP technique reported in literature.[19,47,49–54]

The researchers in the Catalysis and Spectrochemistry Laboratory has designed is own homebuilt xenon polarizer system, already described in the El Siblani phD's thesis.[55]

This SEOP apparatus was designed to work at pressure range one to two bar. The xenon polarizer is built up with several parts (figure 1.2):

- **Electromagnetic coils** The magnetic field required for hyperpolarization is generated by an assembly of five coaxial electromagnetic coils. These five electromagnetic coils are a combination of two Helmholtz coils and three maxwell coils. Each coil was designed and positioned in order to optimized the homogeneity of the field on the central axis where SEOP cell is placed. These coils are located at a distance equal to their radius in which equal current flow in the same direction. The magnetic field produced by coils is achieved by overlapping each coil field. With this arrangements current in all the coils flows in the same directions, thus the magnetic field induction obtained by each of the coils is almost uniform.
- **SEOP cell** SEOP cell is the heart of the xenon polarizer system. The cell is 30 cm long borosilicate glass with 3 cm diameter optical flats sealed to both end. The inner cylinder is 3 cm diameter and the outer is 5 cm. Hot silica oil is permitted to diffuse through glass cell to maintain cell at a desire temperature controlled by circulating bath with advanced digital

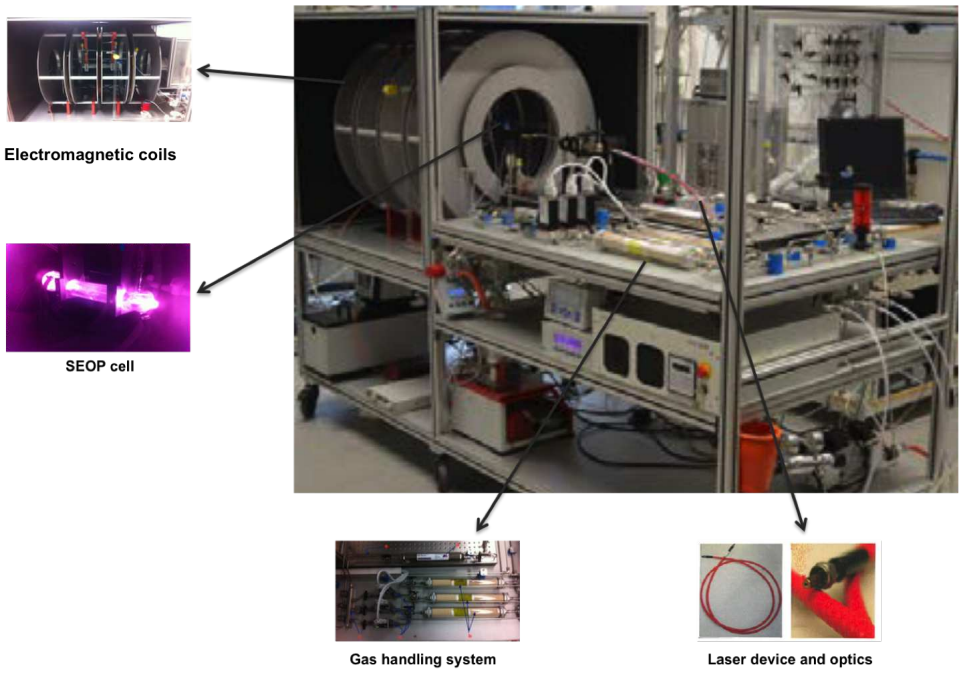

FIGURE 1.2: Xenon polarizer with instrumental parts such as Electromagnetic coils, SEOP cell, Gas handling system, Laser device and optics.

temperature controller system AD07H200-V12V. The inlet and outlet gas ports consist of 1 cm borosilicate tubing attached to each extremity and fitted with teflon stopcocks located 15 cm from the points of attachments to the pumping cell. The SEOP cell is mounted in such a way that its front window is facing to the laser beam where the gas flow enter from the rear side and exit from the front side. As paramagnetic oxygen atoms contained in the glass of SEOP cell contribute to the longitudinal relaxation of hyperpolarized ^{129}Xe due to collision with cell wall. To reduce the rate of this phenomena, the inner surface of the cell coated by using a solution of dichlorodimethylsilane (DDMS). During the optical pumping experiments rubidium in the metal form is introduced in this part with regulated temperature to control the rubidium vapour density. The cell is placed in an homogeneous magnetic field which is irradiated with a laser beam, parallel to the direction of magnetic field. A gas mixture containing Xe and buffer gases (He, N_2) flow through it at a given pressure

- **Gas handling system** is another important part of the polarization system, which is designed to provide a close circuit with a continuous stream of polarized ^{129}Xe gas mixture directly to sampling tube in the NMR probe. The gas mixture containing Xenon, Nitrogen and Helium is prepared from individual gas bottles and introduced directly in the circuit using control panel. Maximum flow rates are 200 sccm for Xe, 500 sccm for N_2 and 1000 sccm for He. Each gas line is equipped with a humidity trap at a entrance of the mass flow controller, once mixed the gas mixture pass through an oxygen trap to eliminate any trace of O_2 which could contaminate the rubidium metal. The main advantage of working in a

close circuit flow system is to reduce the amount of gases consumed during experiments which can avoid to reintroduce gas again in the system.

- **Laser device and optics** The SEOP apparatus incorporates a compact laser diode device air cooled version (provided by DILAS industrial laser systems) with capacity to generates an optical output power up to 100 W tuned to 794.7 nm figure by thermoelectric temperature control and narrow Full Width at Half-Maximum (FWHM) of 0.5 nm. Safety glasses are compulsory while working with laser to avoid accidents in laboratories. The components of this laser diode device are built in 19" rack mount technology with the parts such as 1)The laser diode module 2)operating and control elements 3)The cooling device 4)diode laser power supply and 5)necessary power supply units. Unlike other laser techniques laser diodes do not use a medium (e.g.laser gas, crystal rod) to generate the laser beam as they use a semiconductor element. The laser radiation is in the near infrared region of the light spectrum thus it is invisible. To align the laser beam at correct position on the laser polarizer,the laser diode device is optionally equipped with laser pilot. This pilot is built from a small laser diode with a low power and produces a visible red laser beam aligned to the main laser beam. It can be switched on/off at any time the device is operated. For better optical pumping of Rb vapor circular polarization of laser light is an essential requirements. To obtain a circularly polarized light an optical polarizer setup which includes light polarizing components need to be implemented.

To compare the ^{129}Xe NMR signal to noise (S/N) enhancement, two experiments were achieved: i) The first used a relatively large pressure of Xe in a glass tubes without SEOP, *i.e.*, using its natural thermal polarization at 300 K and ii) with samples in a continuous flow of hyperpolarized ^{129}Xe.

It is then clear that with the optical pumping methods, S/N signal to noise ratio shows improvements which is not possible in using thermally polarized xenon which clearly shown in figure 1.3

1.3.3 SEOP dependence parameters

The polarization of ^{129}Xe via Spin Exchange Optical Pumping depends on different parameters such as:

- The characteristics of the laser: The polarization of Rb electronic spins depends on the fraction of photon current adsorbed by rubidium vapor, this fraction itself depends on the power and the full width at half-maximum of its spectral output (FWHM) (this parameter is fixed for a given laser source and should be negotiated before ordering the laser)

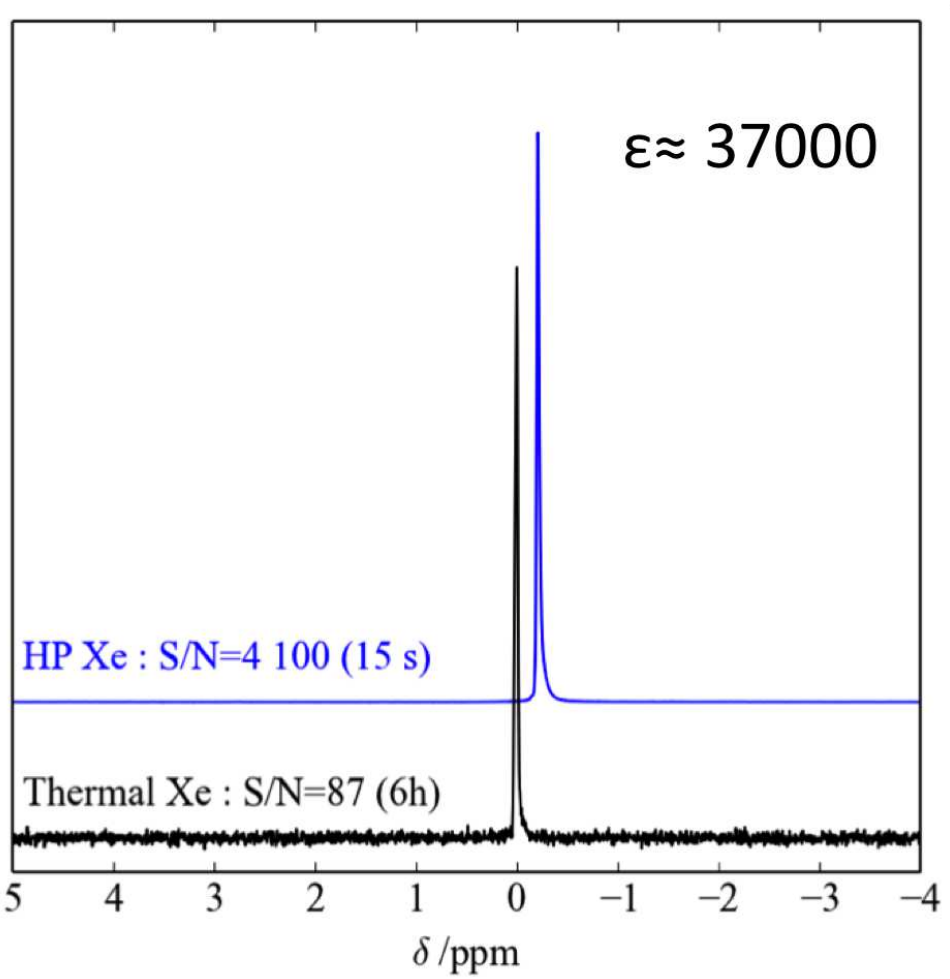

FIGURE 1.3: Gas phase ^{129}Xe NMR spectra showing the clear difference between the S/N ratio for both hyperpolarized xenon and thermally polarized nuclei

- The density of Rb vapor, this parameter depends on the quantity of Rb metal introduced and could be controlled by the temperature of the pumping cell.

  $[Rb] \quad \nearrow \quad \longmapsto \quad \gamma_{se} \quad \nearrow \quad \longmapsto P_{Xe} \quad \nearrow$

- The homogeneity of the external magnetic field.

- The gas mixture: its composition, flow rate (F), and pressure.

In general, the use of high pressure (≈ MPa) is needed in order to increase the optical absorption by pressure broadening of the Rb resonance line. However, by using reduced laser line width, the highest values of polarization could be achieved at lower pressure, which is advantageous since Rb spin destruction is reduced.

By appropriate choice of these parameters, the final polarization of ^{129}Xe gas can be optimized to maximum. In the following paragraph we outline how to experimentally determine the polarization enhancement factor of HP ^{129}Xe, and some optimization parameters in order to have the best enhancement.

The ^{129}Xe nuclear polarization enhancement factor, ε, is defined as a ratio of the enhanced polarization P_z to the thermal equilibrium $P_z^{ref} = 6.83 \times 10^{-6}$ (at room temperature). Knowing that the maximum polarization which could be obtained theoretically is equal to one, the theoretical maximum enhancement factor is 1.46×10^5. Experimentally, at a specified field and temperature, the enhancement factor can be estimated from the ratio of NMR signal of a polarized ^{129}Xe gas (S) and a reference signal from a thermally polarized gas (S^{ref}) taking into account the difference of experimental conditions:[48]

$$\varepsilon = \frac{P_z}{P_z^{ref}} = \frac{S}{S^{ref}} \times \frac{N_s^{ref}}{N_s} \times \frac{f^{ref}}{f} \times \frac{p^{ref}}{p} \times \frac{\chi^{ref}}{\chi} \tag{1.4}$$

where N_s is the number of FID accumulated in each experiment, p is the pressure, f is the fractional isotopic abundance of ^{129}Xe and χ is Xe mole fraction in the gas mixture.

To apply this kind of calculation to our system, we have used the same home-made NMR tube for all experiments (thermal or hyperpolarized xenon), in order to have the same volume for all samples in the detection region of the NMR probe. The reference sample, consists of 150 kPa of xenon gas (natural isotopic abundance) containing $\simeq 1\%$ of oxygen to reduce the ^{129}Xe relaxation time. 512 FIDs with a recycle delay of 40 s were accumulated to improve the signal to noise ratio. Table 1.1 summarizes the different characteristics of thermal equilibrium reference sample and the hyperpolarized sample. As shown in this table, ε is close to $38{\times}10^3$, corresponding to a polarization inside the spectrometer of about 26%.

Table 1.1: Experimental parameters used to calculate ^{129}Xe polarization

	Reference sample	Hyperpolarized sample
Total pressure (kPa)	150	126
Temperature (K)	300	300
Xe mole fraction, χ	0.99	0.01348
^{129}Xe isotopic fraction, f	0.264	0.264
#FIDs accumulated, N_s	512	8
Signal integration, S	1	6.8
Enhancement factor, ε	1	37856
^{129}Xe polarization, P_z	$6.83{\times}10^{-6}$	0.258

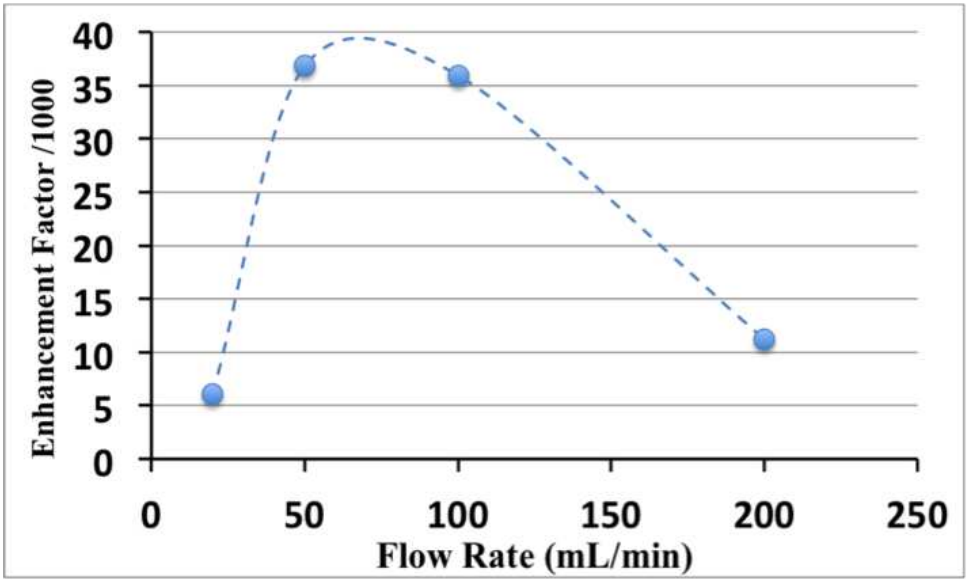

FIGURE 1.4: Enhancement factor of ^{129}Xe polarization as function of the gas flow rate at a total pressure of 126 kPa and a SEOP cell temperature of 390 K.

The flow rate, F, has obviously an effect on the polarization. It modified the average residence time in the cell and thus the pumping time $t_p = V_{cell}/F$. Thus when $F \searrow \longmapsto t_p \nearrow \longmapsto P_{Xe} \nearrow$. In a continuous flow mode, the hyperpolarized xenon directly transit to the NMR spectrometer through the fringe-field via PFA tubing, and therefore T_1 relaxation inevitably take place. When $F \searrow \longmapsto$ relaxation rate $R_1 \nearrow \longmapsto P_{Xe} \searrow$. Another feature of the flow rate effect can be the Rb runaway from the SEOP cell which become important at high flow rate.

Figure 1.4 shows the measured enhancement factor ε of ^{129}Xe polarization as a function of gas mixture flow rate through the SEOP cell heated up to 390 K for a gas mixture containing 2% of xenon at a total pressure P=126 kPa, we observe a sharp increase of in polarization over the range of 50-100 mL/min. At a lower flow the relaxation rate increase as HP ^{129}Xe spend more time in PFA tube before arriving to the detection coil, where at the highest flow rate tested (200 mL/min) the residence time of xenon atoms decreases and hence the enhancement factor is less important.

The increase of SEOP cell temperature leads to a higher rubidium vapor density and by consequence more polarized Rb atoms capable to exchange polarization with xenon. Figure 1.5 shows the enhancement of ^{129}Xe polarization as a function of SEOP cell temperature. In fact, as Rb suffer from oxidation along time due to trace of oxygen and impurities which could be introduced inside the pumping cell, the vapor density cannot remain constant for a given temperature. The effect of this problem is recognized after several days of experiments as the polarization decreases dramatically.

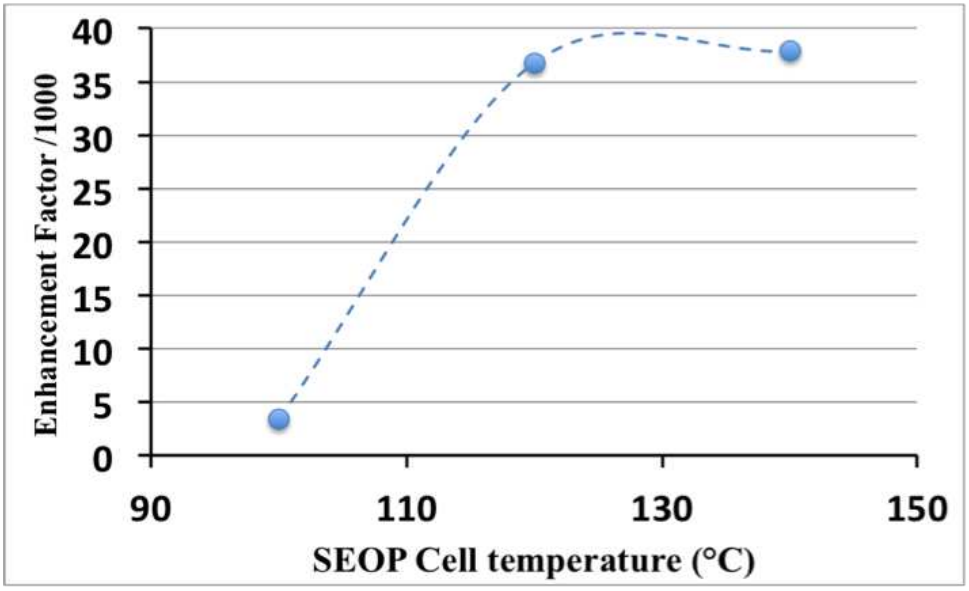

FIGURE 1.5: Enhancement factor of ^{129}Xe polarization as function of the SEOP cell temperature at a total pressure of 126 kPa and a SEOP a flow rate of 50 mL/min.

1.4 Applications of Hyperpolarized xenon NMR

1.4.1 Introduction

Adsorption of gases on solid materials used for determination of specific surface area, pore volume and pore size distributions and pore-connectivity has shown wide application since many years.[56–58] Similarly, adsorption of xenon gas has found applications especially in NMR spectroscopy. But the direct NMR measurement of adsorption of xenon gas has a problem with sensitivity and a long relaxation time make acquisition very long. Hyperpolarized technique overcome these problems by the use of Spin Exchange Optical Pumping (SEOP) methods as previously discussed.

Hyperpolarized ^{129}Xe NMR has numerous applications in many fields of chemistry and pharmaceutical science such as MRI as shown in figure 1.2. The central idea of this method in material science is to probe the porosity and species distribution in porous materials. By considering the limitations of other conventional characterization techniques this technique has shown a numerous applications in many areas of material science. As it combines the very high sensitivity provided by the Spin Exchange Optical Pumping techniques and it works at very low concentration of xenon under continuous flow. The contribution of Xe-Xe interactions vary with change in temperature and the observed ^{129}Xe chemical shift could reflect mainly interactions between xenon atoms and the surface. The various application of this method can be summarized as,

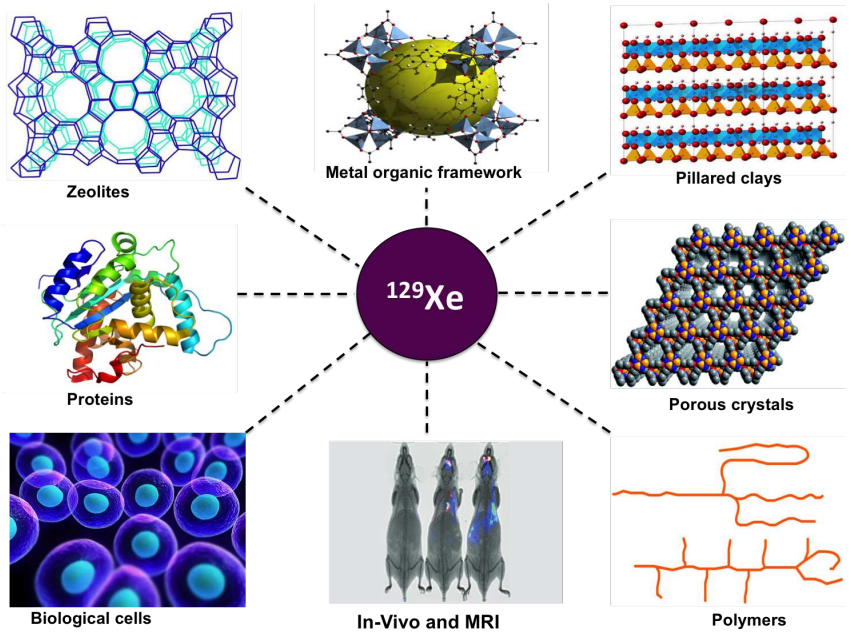

Scheme 1.2: ^{129}Xe is a very versatile NMR probe,used in a wide range of applications from material chemistry to biological cells.

1.4.2 Metal-organic frameworks

The class of porous materials, which are consisting of metal ions or clusters coordinated to organic ligands to form one, two or three-dimensional structures are known as MOF.As xenon used as a probe to study the MOF based materials from many years.[59–64]

Springuel-Huet and coworkers used xenon as a probe to study the framework flexibility of porous hybrid MIL-53(Al).[65] As this hybrid structure exhibits a structural transitions between two possible porous structures, such as large-pore and narrow-pore forms.The Hyperpolarized ^{129}Xe NMR used to study the large-pore narrow-pore transitions induced by adsorption of xenon and xenon adsorption isotherm.The same researchers used Continuous flow hyperpolarized xenon NMR to confirm the flexibility of zeolitic imidazolate frameworks ZIF-8 lattice. Xenon adsorption isotherm studied by varying the temperature and it proves that at low temperature the organic linkers undergo a reorientation leading to a stepwise increase in xenon adsorption and in chemical shift value too.[66]

Eike Brunner and coworkers used ^{129}Xe NMR spectroscopy to study the structural transitions phenomena in Ni_2(2,6-ndc)$_2$(dabco). The chemical shift of ^{129}Xe NMR spectra used to study the structural transition from a narrow pore system with low porosity to a wide pore state.[67] They have used the in-situ variable pressure ^{129}Xe NMR to characterized the zirconium based MOF. The chemical shift value correlates with pore size of studied materials such as UiO-66, UiO-67 and DUT-67.[68,69] with in situ xenon experiments it proved that UiO-66 exhibits the smallest pores and therefore it appears at higher chemical shift whereas UiO-67 and DUT-67 have nearly same pore size and appears nearly same ^{129}Xe chemical shift. Katie Campbell used this method to establish the solid-state porosity of shape-persistent macrocycles with MOF. Hyperpolarized xenon NMR proved that even upon removal of cocrystallized solvent molecules, the macrocycles maintain a porous or channeled structure.[70]

1.4.3 Pillared Clays

Pillared Clays are two-dimensional microporous materials. Due to their high surface area and permanent porosity they are very attractive solids for adsorption and catalysis purposes. To study the porosity in this class of materials xenon used as a probe molecule from researchers working with xenon NMR. Jurgen senker and group used the Hyperpolarized xenon NMR and xenon adsorption isotherm to get the local arrangement within the interlayer space. They studied the effect of organic molecule (Me_2DABCO^{2+}) which used as a pillering molecule on hectorite clays.[71] In this study CF-HP ^{129}Xe MAS NMR methods and Xe physisorption measurements used to probe the changes on the interface with changing surface conditions. This technique shows further applications to investigate the structure and properties of hybrid organic–inorganic layered

materials,[72] and to study the interlayer nannoporosity.[73] In tetraethylammonium-hectorite HP ^{129}Xe NMR adsorption measurments shows the storage capacity of gas. EXSY NMR reveal the arrangement of the hybrid structures with surfactants, identifying the species interacting at the interfaces.[72]

1.4.4 Porous Molecular crystals

Another application of hyperpolarized ^{129}Xe NMR is to study the surface properties and orientation in a single crystal. Piero Sozzani used this technique to study the porous single crystal of tris-o-phenyeledioxycyclotriphosphazene (TPP) molecule.[74] As shown in Figure, 1.6 the c axis of the crystal was inclined at variable θ angles from 0° to 90° with respect to the main magnetic field and the 1D xenon NMR spectrum was acquired at each given inclination. Figure 1.6 shows clearly that the chemical shift difference between 0° (111.9 ppm) to 90° (80.9 ppm) is 31 ppm . This clearly shows that with change in angle the xenon-wall and xenon-xenon interaction predominant which affects to change in chemical shift as well. The presence of a single resonance in each spectrum indicates that all xenon nuclei experience the same environment. This application helps to give an exceptional example to study the orientation in single crystals by xenon NMR.

1.4.5 Polymers

Hyperpolarized xenon NMR could also explore to study the porous polymeric materials and copolymers.[75,76] Piero Sozzani and group used H.P ^{129}Xe NMR to study the glass transition temperature and phase extension of complex particles in each polymer phase.[77] As the main advantage of using CF HP xenon NMR technique is that at the low concentration xenon did not swell the polymers and could only explore the surface-layer of materials within calibrated time. The same technique they have used to study the structural transformation in Al(OH)(1,4-NDC)·2H_2O Al-Based coordination polymers. As the crystal structure of this coordination polymer three-dimensional framework to demonstrate the open pore structure and the easy accessibility of the nanochannels to the gas phase, hyperpolarized (HP) xenon NMR, under extreme xenon dilution, has been applied.[78]

1.4.6 Zeolites

^{129}Xe NMR spectroscopy shows much of its interest for investigating microporous materials such as zeolites.[79,80] One and two dimensional ^{129}Xe Exchange NMR spectroscopy has been used to study the zeolites from many years.[81–83] In the pure gas form ^{129}Xe NMR shows a drawback of very long T_1 relaxation time (upto 45min) but addition of small amount of paramagnetic oxygen

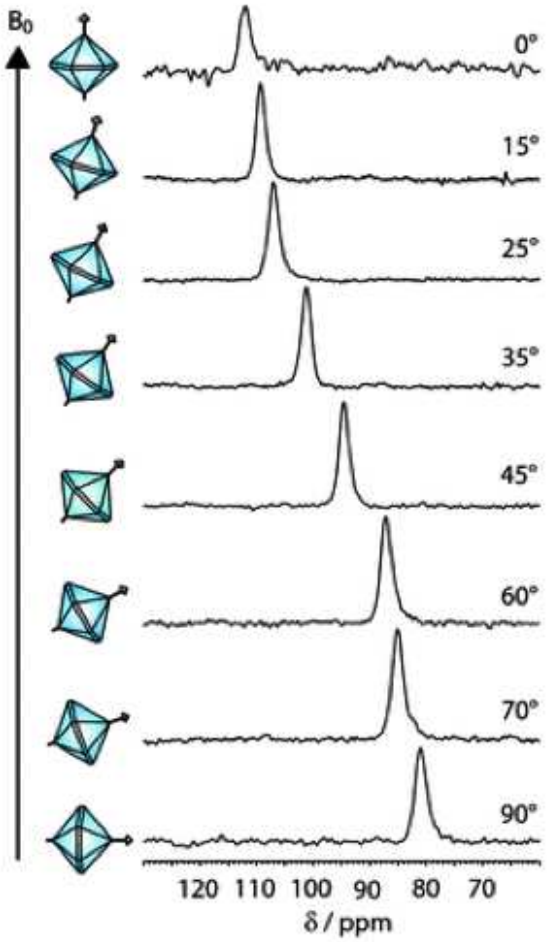

FIGURE 1.6: Continuous flow hyperpolarized ^{129}Xe NMR spectra of the porous molecular single crystal inclined at variable orientation from 0° to 90° with respect to the main magnetic field. Figure adopted from ref.[74]

reduces the relaxation time to 10 ms .[84] Taro Ito and Jacques Fraissard[6] used the isotope ^{129}Xe first time to find the non reactive molecule which particularly sensitive to its environment where they have used Xe as a probe molecule to study the properties of Y zeolite. Another application of ^{129}Xe NMR spectroscopy in the mesoporous silica materials *e.g.*, MCM-41 used to study the distribution and the dynamics of ibuprofen encapsulated in MCM-41 with two different pore diameters.[85] Si/Al ratio is another aspect to be considered while studying the zeolites by HP ^{129}Xe NMR.[86] For MCM-22 when it undergoes dealumination *i.e.*, for sample ITQ-2. 1D ^{129}Xe NMR spectra show an additional signal than the parent zeolites sample. For ITQ-2 these additional signal corresponding to xenon exchanging between the adsorbed phase and the gaseous phase.[87]

The chemical shift of adsorbed Xe on zeolites which are exchanged with divalent cations is another interest studied by Cheung *et al.*.[88] which explained xenon adsorption effect in terms of strongly adsorbed Xe atoms and in the void space of the zeolite pores. Xe adsorbed on divalent cations donates one of the 5p electrons to the empty s-orbital of the cation. The corresponding

bond formation introduces excited electronic states that leads to a large paramagnetic contribution to the ^{129}Xe NMR shift.[88] Gedeon *et al.*[89] used Xe NMR to study the oxidation state and the location of copper in CuY zeolite along with xenon-copper interaction.In a number of studies xenon atoms adsorbed on zeolites exchanged with Cd^{2+}, Zn^{2+}, Ce^{3+}, and La^{3+}[90–92] and loaded with metal particles (Ni, Rh, Ru, Pd, Pt) were investigated.[93,94] To study the xenon chemical shift and the presence of paramagnetic cations eg Ni^{2+} in zeolite Y Bansal and Dybowski observed 14% nickel occupies predominantly positions in the sodalite cages with increasing nickel content a paramagnetic shift arising in samples.[95]

1.5 Chemical shift in 129-Xenon NMR

In 1970 Jameson *et al.*[96] established a relationship between ^{129}Xe NMR shift δ and the density ρ of the pure xenon gas.

$$\delta = \delta_{ref} + \sigma_1 \times \rho + \sigma_2 \times \rho^2 + \sigma_3 \times \rho^3 \tag{1.5}$$

Where δ_{ref} is the shift of the free xenon gas at very low concentration and σ_i are higher order viriel coeficients which describes the influence of the many-bodies collisions of xenon atoms on the resonance position. This equation shows that the observed chemical shift strongly depends on the gas density. This was early exploited by Fraissard[6] and coworkers who developed the above equation for porous material.

The chemical shift of xenon adsorbed on porous materials is a sum of several terms corresponding to the various perturbations involved:

$$\delta = \delta_{ref} + \delta_S + \delta_{Xe-Xe} + \delta_{SAS} + \delta_E + \delta_M \tag{1.6}$$

where,

- δ_{ref} is the reference (gaseous Xe at zero pressure).
- δ_S arises from interactions between xenon and the surface of the pores, provided that the solid does not contain any electrical charges. In this case, it depends only on the dimensions of the cages or channels and on the diffusion of xenon.
- δ_{Xe-Xe} corresponds to the many bodies Xe-Xe interactions, developped in eq.1.5. At low xenon concentration, we assume that δ_S predominate as the probability to have a collision between two or more xenon atoms in the void space become negligible.
- δ_{SAS} is the influence of Strong Adsorption Site (SAS) where each Xe atom spends a relatively long time.

The last two terms are the effect of electric field δ_E and magnetic field δ_M due to the presence of paramagnetic species.

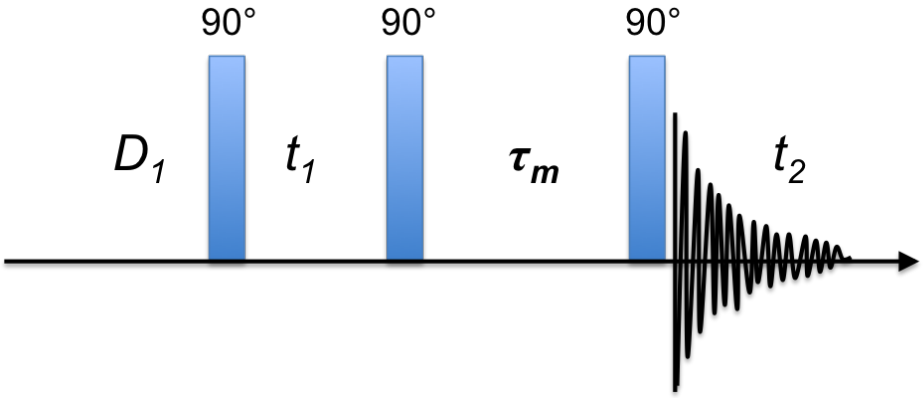

FIGURE 1.7: 2D EXSY pulse sequence

1.5.1 2D EXSY ^{129}Xe NMR

2D EXSY xenon NMR experiment is used to study the structural heterogeneities and structural dynamics in porous material. It gives valuable information about xenon exchange, xenon diffusion and to study the dynamics of xenon exchange between the cages.[81,97,98]

The 2D exchange experiment is based on a stimulated echo pulse scheme. Initially transverse magnetization is prepared by a $\pi/2$ radio frequency pulse. During the evolution period t_1, magnetization vectors acquire a frequency dependent phase. After the second $\pi/2$ pulse the magnetization is longitudinal. The exchange process takes place during the mixing period t_m where the delay is fixed within a 2D experiments. A third $\pi/2$ pulse rotates the longitudinal magnetization into the x-y plane for detection during period t_2. The experiments has to be repeated for a number of equally spaced values of the evolution time t_1 which gives data matrix (t_1,t_2). Off diagonal peaks in the 2D spectrum appear as a result of exchange within a mixing period t_m.[99,100]

A graphical representation of 2D EXSY spectrum is shown in a scheme 1.3 Here we represent the two porosity namely A and B. The 1D spectrum is found in the diagonal. Scheme 1.3 show exchange between xenon gas and porosities A and B. The cross peaks A/B and B/A gives information about exchange within the pores and interconnectivity with therein. One can change the mixing time from low to high mixing time to see the interconnectivity and pore size distribution. Change in a mixing time will help to understand whether its a slow exchange process or exchange took a long time. With respect to the intensities of the diagonal and cross peaks signals the exchange rate constant and exchange process of xenon atoms between two different pores can be determined.[101–103]

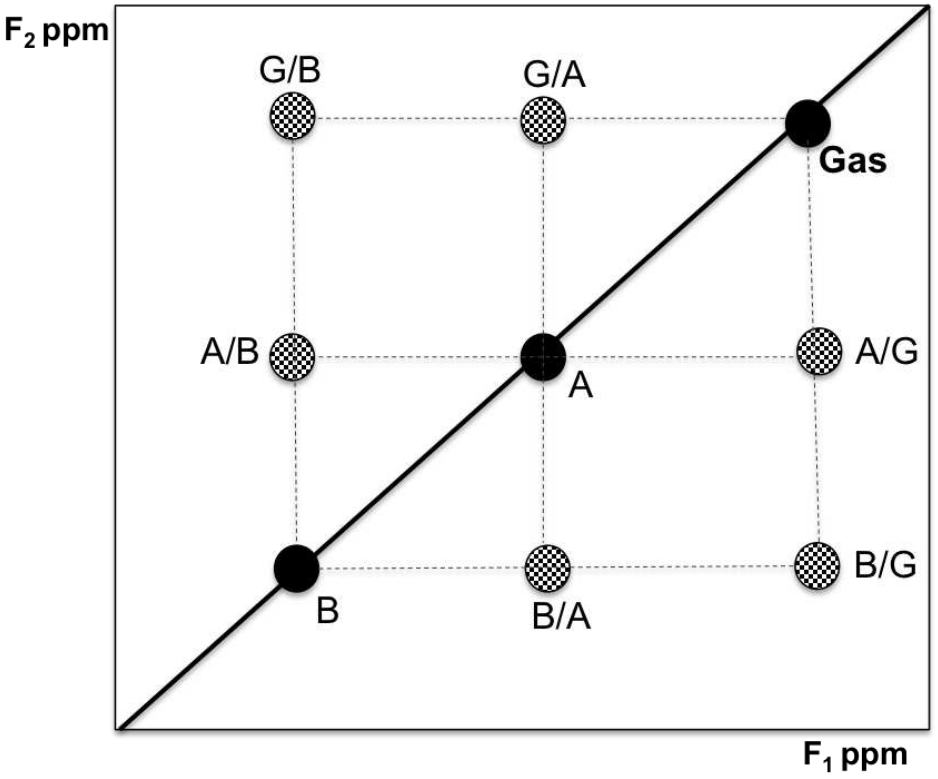

Scheme 1.3: 2D EXSY graphical presentation showing exchange of xenon between the gas phase (G) and the porosity (A) and (B)

1.5.2 Modeling the xenon chemical shit vs. temperature : Theoretical model

To understand the chemical shift in ^{129}Xe NMR, we need considering the time scale of the NMR spectroscopy. Indeed, two species A and B which are in chemical equilibrium, may present very different NMR spectra depending on the exchange rate. Two extreme cases can be ascribed quite easily:

1. When the exchange frequency k_{AB} is much smaller than the difference in their chemical shifts ($k_{AB} \ll \delta_A - \delta_B$) the NMR spectrum presents a resonance line for each of the species, *i.e.*,, at δ_A and δ_B. This is the "slow" exchange regime.

2. When, in the opposite case, the species are in "fast" exchange between two states ($k_{AB} \gg \delta_A - \delta_B$) only an average value of the chemical shift $\overline{\delta}$ is observed.

The spectra are of course much more complex when the exchange is in an intermediate regime: $k_{AB} \approx \delta_A - \delta_B$

In the case of the xenon gas in contact with the porous network of a zeolite, the xenon atoms are either absorbed on the internal surface with a chemical shift δ_a or in the gas phase inside the

pore void space, where the chemical shift is δ_g. In the fast exchange case, the observed chemical shift is thus given by:

$$\delta = \frac{n_a\delta_a + n_g\delta_g}{n_a + n_g} \tag{1.7}$$

where n_a and n_g are the number of atoms in the adsorbed and gas phase, respectively.

Note that the contribution of the free xenon atoms inside cavities to the chemical shift arises from $Xe - Xe$ collisions and is proportional to the density ρ_{Xe} (see eq. 1.5):

$$\delta_g = \sigma_{Xe-Xe}\cdot\rho_{Xe} \tag{1.8}$$

According to the Henry's law, for systems at low relative occupancy and when the temperature and surface area of adsorption are fixed, the number of adsorbed molecules on a surface S is given by:

$$n_a = K(T)P_gS \tag{1.9}$$

while, considering the ideal gas law in the gas phase, n_g is given by

$$n_g = \frac{P_gV_g}{RT} \tag{1.10}$$

where $K(T)$ is the Henry adsorption constant, P_g the gas pressure and V_g the volume of the pore.

At a low partial pressure of xenon, which is the case in our system where in general 2% of xenon is mixed with helium and nitrogen, the collisions between two atoms are negligible, and consequently one can consider $\delta_g = 0$. Therefore the substitution of eq.1.9 and eq.1.10 in eq.1.7 give:

$$\delta = \delta_a\left[1 + \frac{V_g}{SKRT}\right]^{-1} \tag{1.11}$$

The Henry's constant K is temperature dependent:

$$K(T) = \frac{K_0\exp\left(Q/RT\right)}{\sqrt{T}} \tag{1.12}$$

where Q is the effective heat of adsorption and K_0 is a pre-exponent factor which is independent of temperature. Substituting eq.1.12 in eq.1.11 gives

$$\frac{1}{\delta} = \frac{1}{\delta_a} + \frac{V_g}{\delta_aSRK_0\exp\left(Q/RT\right)\sqrt{T}} \tag{1.13}$$

which can be conveniently rewritten:

$$\ln\left[(\frac{\delta_a}{\delta} - 1)\sqrt{T}\right] = \ln\left(\frac{V_g}{SRK_0}\right) - \frac{Q}{RT} \tag{1.14}$$

When the experimental data are plotted according the eq.1.14 as a function of $1/T$, one should obtained a straight line with a slope proportional to the heat of adsorption (Q). The extrapolated values at $T \to \infty$ give an estimate of the S/V_g ratio and thus of the pore size and/or geometry. Unfortunately, this representation is based on a multivariate fit of the experimental data, that is to say that if none of the Q, S, V_g, K_0 or δ_a is independently known, there is no unique solution to the eq.1.14.

Moreover, it is worth noticing that this model is unlikely fully applicable to the case of very small pores as the above derivation assumes an ideal gas in the void pore space.

Bibliography

[1] W. Ramsay and M. W. Travers. On the extraction from air of the companions of argon and neon. In *Report of the Meeting of the British Association for the Advancement of Science*, volume 828, 1898. 5

[2] P. Berthault, G. Huber, and H. Desvaux. Biosensing using laser-polarized xenon NMR/MRI. *Progress in Nuclear Magnetic Resonance Spectroscopy*, 55(1):35–60, 2009. doi:10.1016/j.pnmrs.2008.11.003. 5

[3] A. Oros and N. J. Shah. Hyperpolarized xenon in nmr and mri. *Physics in Medicine and Biology*, 49(20):105–153, 2004. doi:10.1088/0031-9155/49/20/R01. 5

[4] J. Jokisaari. Nmr of noble gases dissolved in liquid crystals. In *NMR of ordered liquids*, pages 109–135. Springer, 2003. 5

[5] Y. Millot, P. P. Man, M.-A. Springuel-Huet, and J. Fraissard. Quantification of electric-field gradients in the supercage of y zeolites by comparing the chemical shifts of 131 xe (i= 3/2) and 129 xe (i= 1/2). *Studies in Surface Science and Catalysis*, 135(1):354–354, 2001. doi:10.1016/S0167-2991(01)81826-7. 5

[6] T. Ito and J. Fraissard. 129xe nmr study of xenon adsorbed on y zeolites. *The Journal of Chemical Physics*, 76(11):5225–5229, 1982. doi:10.1063/1.442917. 5, 21, 23

[7] L. T. Kuhn. *Hyperpolarization Methods in NMR Spectroscopy*. Springer, 2013. doi:10.1007/978-3-642-39728-8. 6

[8] R. A. Green, R. W. Adams, S. B. Duckett, R. E. Mewis, D. C. Williamson, and G. G. R. Green. The theory and practice of hyperpolarization in magnetic resonance using parahydrogen. *Progress in Nuclear Magnetic Resonance Spectroscopy*, 67:1–48, 2012. doi:10.1016/j.pnmrs.2012.03.001. 6

[9] B. M. Goodson, N. Whiting, A. M. Coffey, P. Nikolaou, F. Shi, B. M. Gust, M. E. Gemeinhardt, R. V. Shchepin, J. G. Skinner, J. R. Birchall, M. J. Barlow, and E. Y. Chekmenev. *Hyperpolarization Methods for MRS*. John Wiley Sons, Ltd, 2007. doi:10.1002/9780470034590.emrstm1457. 6

[10] P. Nikolaou, A. M. Coffey, M. J. Barlow, M. S. Rosen, B. M. Goodson, and E. Y. Chekmenev. Temperature-ramped 129xe spin-exchange optical pumping. *Analytical chemistry*, 86(16):8206–8212, 2014. doi:10.1021/ac501537w. 6

[11] I. V. Koptyug, K. V. Kovtunov, S. R. Burt, M. S. Anwar, C. Hilty, S.-I. Han, A. Pines, and R. Z. Sagdeev. Para-hydrogen-induced polarization in heterogeneous hydrogenation reactions. *Journal of the American Chemical Society*, 129(17):5580–5586, 2007. doi:10.1021/ja068653o. 6

[12] B. M. Goodson. Nuclear magnetic resonance of laser-polarized noble gases in molecules, materials, and organisms. *Journal of Magnetic Resonance (San Diego, Calif.: 1997)*, 155 (2):157–216, 2002. doi:10.1006/jmre.2001.2341. 6, 9

[13] K. Golman, O. Axelsson, H. Jóhannesson, S. Månsson, C. Olofsson, and J. Petersson. Parahydrogen-induced polarization in imaging: Subsecond 13c angiography. *Magnetic resonance in medicine*, 46(1):1–5, 2001. doi:10.1002/mrm.1152. 6

[14] C. Gabellieri, S. Reynolds, A. Lavie, G. S. Payne, M. O. Leach, and T. R. Eykyn. Therapeutic target metabolism observed using hyperpolarized 15n choline. *Journal of the American Chemical Society*, 130(14):4598–4599, 2008. doi:10.1021/ja8001293. 6

[15] G. E. Pavlovskaya, Z. I. Cleveland, K. F. Stupic, R. J. Basaraba, and T. Meersmann. Hyperpolarized krypton-83 as a contrast agent for magnetic resonance imaging. *Proceedings of the National academy of Sciences of the United States of America*, 102(51):18275–18279, 2005. doi:10.1073/pnas.0509419102. 6

[16] B. M. Goodson. Using injectable carriers of laser-polarized noble gases for enhancing nmr and mri. *Concepts in Magnetic Resonance Part A*, 11(4):203–223, 1999. doi:10.1002/(SICI)1099. 6

[17] J. C. Leawoods, D. A. Yablonskiy, B. Saam, D. S. Gierada, and M. S. Conradi. Hyperpolarized 3he gas production and mr imaging of the lung. *Concepts in magnetic resonance*, 13:277–293, 2001. doi:10.1002/cmr.1014. 6

[18] S. J. et.al. Metabolic imaging of patients with prostate cancer using hyperpolarized (1-13c) pyruvate. *Science Translational Medicine*, 5:277–293, 2013. doi:10.1126/scitranslmed.3006070. 6

[19] D. Raftery, H. Long, T. Meersmann, P. J. Grandinetti, L. Reven, and A. Pines. High-field nmr of adsorbed xenon polarized by laser pumping. *Physical Review Letters*, 66(5): 584–587, 1991. doi:10.1103/PhysRevLett.66.584. 6, 11

[20] D. Raftery, H. Long, L. Reven, P. Tang, and A. Pines. Nmr of optically pumped xenon thin films. *Chemical physics letters*, 191(5):385–390, 1992. doi:10.1016/0009-2614(92)85396-R. 7

[21] H. W. Long, H. C. Gaede, J. Shore, L. Reven, C. R. Bowers, J. Kritzenberger, T. Pietrass, A. Pines, P. Tang, and J. A. Reimer. High-field cross polarization NMR from laser-polarized xenon to a polymer surface. *Journal of the American Chemical Society*, 115(18): 8491–8492, 1993. doi:10.1021/ja00071a086. 7

[22] T. Pietrass, A. Bifone, and A. Pines. Adsorption properties of porous silicon characterized by optically enhanced 129xe nmr spectroscopy. *Surface science*, 334(1-3):L730–L734, 1995. doi:10.1016/0039-6028(95)80024-7.

[23] Y.-Q. Song, B. M. Goodson, R. E. Taylor, D. D. Laws, G. Navon, and A. Pines. Selective enhancement of nmr signals for α-cyclodextrin with laser-polarized xenon. *Angewandte Chemie International Edition*, 36(21):2368–2370, 1997. doi:10.1002/Anie.199723681. 7

[24] J. Kritzenberger, H. C. Gaede, J. S. Shore, A. Pines, and A. T. Bell. 129xe nmr study of tio2 (anatase)-supported v2o5 catalysts. *The Journal of Physical Chemistry*, 98(40): 10173–10179, 1994. doi:10.1021/J100091a037. 7

[25] C. Bowers, T. Pietrass, E. Barash, A. Pines, R. Grubbs, and A. Alivisatos. Probing cds nanocrystal surfaces with laser-polarized xenon. *The Journal of Physical Chemistry*, 98 (38):9400–9404, 1994. doi:10.1021/j100089a008. 7

[26] W. Brewer and M. Kopp. Brute-force nuclear orientation. *Hyperfine Interactions*, 2(1): 299–305, 1976. doi:10.1007/BF01021151. 7

[27] W. D. Brewer. "brute-force" nuclear orientation: A survey of accomplishments and problems to date. *Journal of Low Temperature Physics*, 27(5-6):651–682, 1977. doi:10.1007/BF00655702. 7

[28] S. Månsson, E. Johansson, P. Magnusson, C.-M. Chai, G. Hansson, J. S. Petersson, F. Ståhlberg, and K. Golman. 13c imaging—a new diagnostic platform. *European radiology*, 16(1):57–67, 2006. 7

[29] E. V. Krjukov, J. D. O'Neill, and J. R. Owers-Bradley. Brute force polarization of 129xe. *Journal of Low Temperature Physics*, 140(5):397–408, 2005. doi:10.1007/s10909-005-7323-4. 7

[30] J. R. Owers-Bradley, A. J. Horsewill, D. T. Peat, K. S. Goh, and D. G. Gadian. High polarization of nuclear spins mediated by nanoparticles at millikelvin temperatures. *Physical Chemistry Chemical Physics*, 15(25):10413–10417, 2013. doi:10.1039/C3CP51274F. 7

[31] A. Abragam. *The principles of nuclear magnetism*. Oxford university press, 1961. ISBN 978-0198520146. 7

[32] R. Wind, M. Duijvestijn, C. Van Der Lugt, A. Manenschijn, and J. Vriend. Applications of dynamic nuclear polarization in 13c nmr in solids. *Progress in Nuclear Magnetic Resonance Spectroscopy*, 17:33–67, 1985. doi:10.1016/0079-6565(85)80005-4. 7

[33] M.-T. Türke and M. Bennati. Saturation factor of nitroxide radicals in liquid dnp by pulsed eldor experiments. *Physical Chemistry Chemical Physics*, 13(9):3630–3633, 2011. doi:10.1039/C0CP02126A. 7

[34] A. Comment, S. Jannin, J.-N. Hyacinthe, P. Miéville, R. Sarkar, P. Ahuja, P. R. Vasos, X. Montet, F. Lazeyras, J.-P. Vallée, P. Hautle, J. A. Konter, B. van den Brandt, J.-P. Ansermet, R. Gruetter, and G. Bodenhausen. Hyperpolarizing gases via dynamic nuclear polarization and sublimation. *Physical Review Letters*, 105:018104, 2010. doi:10.1103/PhysRevLett.105.018104. 7

[35] A. Capozzi, C. Roussel, A. Comment, and J.-N. Hyacinthe. Optimal glass-forming solvent brings sublimation dynamic nuclear polarization to 129xe hyperpolarization biomedical imaging standards. *The Journal of Physical Chemistry C*, 119(9):5020–5025, 2015. doi:10.1021/jp5124053. 8

[36] J. Brossel and A. Kastler. The detection of magnetic resonance of excited levels: depolarization effect of optical resonance and fluorescence radiations. *CR Acad. Sci.*, 229: 1213–1215, 1949. 8

[37] T. G. Walker and W. Happer. Spin-exchange optical pumping of noble-gas nuclei. *Review of Modern Physics*, 69(2):629–642, 1997. doi:10.1103/RevModPhys.69.629. 8

[38] T. G. Walker. Fundamentals of spin-exchange optical pumping. In *Journal of Physics: Conference Series*, volume 294, page 012001, 2011. doi:10.1088/1742-6596/294/1/012001.

[39] W. Happer, E. Miron, S. Schaefer, D. Schreiber, W. A. van Wijngaarden, and X. Zeng. Polarization of the nuclear spins of noble-gas atoms by spin exchange with optically pumped alkali-metal atoms. *Physical Review A*, 29(6):3092–3110, 1984. doi:10.1103/PhysRevA.29.3092.

[40] G. D. Cates, R. J. Fitzgerald, A. S. Barton, P. Bogorad, M. Gatzke, N. R. Newbury, and B. Saam. Rb-129xe spin-exchange rates due to binary and three-body collisions at high xe pressures. *Physical Review A*, 45:4631, 1992. doi:10.1103/PhysRevA.45.4631. 8, 9

[41] D. A. Barskiy, A. M. Coffey, P. Nikolaou, D. M. Mikhaylov, B. M. Goodson, R. T. Branca, G. J. Lu, M. G. Shapiro, V.-V. Telkki, V. V. Zhivonitko, et al. Nmr hyperpolarization techniques of gases. *Chemistry-A European Journal*, 23(4):725–751, 2017. doi:10.1002/chem.201603884. 10

[42] S. Appelt, A. B.-A. Baranga, C. J. Erickson, M. V. Romalis, A. R. Young, and W. Happer. Theory of spin-exchange optical pumping of ^{3}he and 129xenon. *Physical Review A*, 58 (2):1412–1439, 1998. doi:10.1103/PhysRevA.58.1412. 9

[43] M. Bouchiat, J. Brossel, and L. Pottier. Evidence for rb-rare-gas molecules from the relaxation of polarized rb atoms in a rare gas. experimental results. *The Journal of Chemical Physics*, 56(7):3703–3714, 1972. doi:10.1063/1.1677750. 9

[44] R. J. Knize. Spin destruction in rubidium-rubidium and potassium-potassium collisions. *Physical Review A*, 40:6219–6222, 1989. doi:10.1103/PhysRevA.40.6219.

[45] S. Kadlecek, L. Anderson, and T. Walker. Field dependence of spin relaxation in a dense rb vapor. *Physical review letters*, 80(25):5512, 1998. doi:10.1103/PhysRevLett.80.5512. 9

[46] S. Parnell, M. Deppe, J. Parra-Robles, and J. Wild. Enhancement of x 129 e polarization by off-resonant spin exchange optical pumping. *Journal of Applied Physics*, 108(6):064908, 2010. doi:10.1063/1.3478707. 11

[47] M. Haake, A. Pines, J. A. Reimer, and R. Seydoux. Surface-enhanced NMR using continuous-flow laser-polarized xenon. *Journal of the American Chemical Society*, 119 (48):11711–11712, 1997. doi:10.1021/ja9713587. 11

[48] A. L. Zook, B. B. Adhyaru, and C. R. Bowers. High capacity production of $>$ 65% spin polarized xenon-129 for NMR spectroscopy and imaging. *Journal of Magnetic Resonance*, 159(2):175–182, 2002. doi:10.1016/S1090-7807(02)00030-7. 11, 15

[49] R. tycko and J. A. Reimer. Optical pumping in solid state nuclear magnetic resonance. *The Journal of Physical Chemistry*, 100(31), 1996. doi:10.1021/jp953667u. 11

[50] N. Whiting, P. Nikolaou, N. A. Eschmann, M. J. Barlow, R. Lammert, J. Ungar, W. Hu, L. Vaissie, and B. M. Goodson. Using frequency-narrowed, tunable laser diode arrays with integrated volume holographic gratings for spin-exchange optical pumping at high resonant fluxes and xenon densities. *Applied Physics B*, 106(4):775–788, 2012. doi:10.1007/s00340-012-4924-x.

[51] B. Driehuys, G. D. Cates, E. Miron, K. Sauer, and D. K. Walter. Highvolume production of laserpolarized 129xe. *Applied Physics Letters*, 69:1668, 1996. doi:10.1063/1.117022.

[52] A. Nossov, F. Guenneau, M.-A. Springuel-Huet, E. Haddad, V. Montouillout, B. Knott, F. Engelke, C. Fernandez, and A. Gedeon. Continuous flow hyperpolarized 129xe-MAS NMR studies of microporous materials. *Physical Chemistry Chemical Physics*, 5(20):4479–4483, 2003-10-02. doi:10.1039/B305793N.

[53] N. J. Shah, T. Unlu, H.-P. Wegener, H. Halling, K. Zilles, and S. Appelt. Measurement of rubidium and xenon absolute polarization at high temperatures as a means of improved production of hyperpolarized 129xe. *NMR in Biomedicine*, 13(4):214–219, 2000. doi:10.1002/1099-1492(200006)13:4.

[54] P. Nikolaou, A. M. Coffey, L. L. Walkup, B. M. Gust, N. Whiting, H. Newton, S. Barcus, I. Muradyan, M. Dabaghyan, G. D. Moroz, M. S. Rosen, S. Patz, M. J. Barlow, E. Y. Chekmenev, and B. M. Goodson. Near-unity nuclear polarization with an open-source 129xe hyperpolarizer for NMR and MRI. *Proceedings of the National Academy of Sciences*, 110(35):14150–14155, 2013-08-27. doi:10.1073/pnas.1306586110. 11

[55] H. El Siblani. *Applications de la RMN du 129Xe hyperpolarisé á l' analyse de matériaux poreux*. PhD thesis, Université de Caen - Normandie, France, 2016. 11

[56] M. Kruk and M. Jaroniec. Gas adsorption characterization of ordered organic- inorganic nanocomposite materials. *Chemistry of Materials*, 13(10):3169–3183, 2001. doi:10.1021/cm0101069. 18

[57] M. Thommes. Physical adsorption characterization of nanoporous materials. *Chemie Ingenieur Technik*, 82(7):1059–1073, 2010. doi:10.1002/cite.201000064.

[58] S. Storck, H. Bretinger, and W. F. Maier. Characterization of micro-and mesoporous solids by physisorption methods and pore-size analysis. *Applied Catalysis A: General*, 174(1): 137–146, 1998. doi:10.1016/S0926-860X(98)00164-1. 18

[59] N. Klein, H. C. Hoffmann, A. Cadiau, J. Getzschmann, M. R. Lohe, S. Paasch, T. Heydenreich, K. Adil, I. Senkovska, E. Brunner, and S. Kaskel. Structural flexibility and intrinsic dynamics in the m2(2,6-ndc)2(dabco) (m =ni, cu, co, zn) metal–organic frameworks. *J Mater Chem*, 22:10303–10312, 2012. doi:10.1039/c2jm15601f. 19

[60] W. Bohlmann, A. Poppl, M. Sabo, and S. Kaskel. Characterization of the metal−organic framework compound cu3(benzene 1,3,5-tricarboxylate)2 by means of 129xe nuclear magnetic and electron paramagnetic resonance spectroscopy. *The Journal of Physical Chemistry B*, 110(41):20177–20181, 2006. doi:10.1021/jp063074r.

[61] C.-Y. Cheng, T. C. Stamatatos, G. Christou, and C. R. Bowers. Molecular wheels as nanoporous materials: Differing modes of gas diffusion through ga10 and ga18 wheels probed by hyperpolarized 129xe NMR spectroscopy. *Journal of the American Chemical Society*, 132(15):5387–5393, 2010. doi:10.1021/ja908327w.

[62] S. Pawsey, I. Moudrakovski, J. Ripmeester, L.-Q. Wang, G. J. Exarhos, J. L. C. Rowsell, and O. M. Yaghi. Hyperpolarized 129xe nuclear magnetic resonance studies of isoreticular metal-organic frameworks. *The Journal of Physical Chemistry C*, 111(16):6060–6067, 2007. doi:10.1021/jp0668246.

[63] K. Campbell, K. J. Ooms, M. J. Ferguson, P. J. Stang, R. E. Wasylishen, and R. R. Tykwinskiac. Shape-persistent macrocycles self-assembly reactions and characterization by hyperpolarized 129xe nmr spectroscopy. *Canadian Journal of Chemistry*, 89(10):1264–1276, 2011. doi:10.1139/v11-077.

[64] K. J. Ooms and R. E. Wasylishen. 129xe nmr study of xenon in iso-reticular metal–organic frameworks. *Concepts in magnetic resonance*, 103:341–351, 2007. doi:org/10.1016/j.micromeso.2007.01.054. 19

[65] M. A. S. Huet, A. Nossov, Z. Adem, F. Guenneau, C. Volkringer, T. Loiseau, G. Ferey, , and A. Gedeon. 129xe nmr study of the framework flexibility of the porous hybrid mil-53 al. *JACS*, 132:11599–11607, 2010. doi:10.1021/ja103105y. 19

[66] M.-A. Springuel-Huet, A. Nossov, F. Guenneau, and A. Gedeon. Flexibility of ZIF-8 materials studied using 129xe NMR. *Chemical Communications*, 49(67):7403–7405, 2013. doi:10.1039/C3CC43119C. 19

[67] N. Klein, C. Herzog, M. Sabo, I. Senkovska, J. Getzschmann, S. Paasch, M. Lohe, E. Brunner, and S. Kaskel. Monitoring adsorption-induced switching by 129xe nmr spectroscopy in a new metal–organic framework ni2(2,6-ndc)2(dabco). *PCCP*, pages 11778–11784, 2010. doi:10.1039/c003835k. 19

[68] M. Oschatz, H. C. Hoffmann, J. Pallmann, J. Schaber, L. Borchardt, W. Nickel, I. Senkovska, S. Rico-Francés, J. Silvestre-Albero, S. Kaskel, and E. Brunner. Structural characterization of micro- and mesoporous carbon materials using in situ high pressure 129xe NMR spectroscopy. *Chemistry of Materials*, 26(10):3280–3288, 2014. doi:10.1021/cm501102y. 19

[69] K. Trepte, J. Schaber, S. Schwalbe, F. Drache, I. Senkovska, S. Kaskel, J. Kortus, E. Brunner, and G. Seifert. The origin of the measured chemical shift of 129 xe in uio-66 and uio-67 revealed by dft investigations. *Physical Chemistry Chemical Physics*, pages 10020–10027, 2017. doi:10.1039/c7cp00852j. 19

[70] K. Campbell, K. J. Ooms, R. E. Wasylishen, and R. R. Tykwinski. Characterization of porosity in organic and metal−organic macrocycles by hyperpolarized 129xe nmr spectroscopy. *Org Lett*, pages 3397–3400, 2005. doi:10.1021/ol050830n. 19

[71] C. D. Keenan, M. M. Herling, R. Siegel, N. Petzold, C. R. Bowers, E. A. Rossler, J. Breu, and J. Senker. Porosity of pillared clays studied by hyperpolarized 129xe NMR spectroscopy and xe adsorption isotherms. *Langmuir*, 29:643–652, 2013. doi:10.1021/la304502r. 19

[72] S. Bracco, P. Valsesia, L. Ferretti, P. Sozzani, M. Mauri, and A. Comotti. Spectroscopic observations of hybrid interfaces and gas storage in organo-clays. *Microporous and Mesoporous Materials*, 107:102–107, 2008. doi:10.1016/j.micromeso.2007.05.013. 20

[73] P. Sozzani, S. Bracco, A. Comotti, M. Mauri, R. Simonutti, and P. Valsesia. Nanoporosity of an organo-clay shown by hyperpolarized xenon and 2d nmr spectroscopy. *Chemical Communications*, (18):1921–1923, 2006. doi:10.1039/b602040b. 20

[74] A. Comotti, S. Bracco, L. Ferretti, M. Mauri, R. Simonutti, and P. Sozzani. A single-crystal imprints macroscopic orientation on xenon atoms. *Chemical Communications*, (4): 350–352, 2007. doi:10.1039/B612002D. 20, 21

[75] D. V. Soldatov, I. L. Moudrakovski, C. I. Ratcliffe, R. Dutrisac, and J. A. Ripmeester. Sorption of xenon, methane, and organic solvents by a flexible microporous polymer catena-bis(dibenzoylmethanato)-(4,4'-bipyridyl)nickel(ii). *chemistry of Materials*, 15(25):4810–4818, 2003. doi:10.1021/cm030433b. 20

[76] F. Junker and W. S. Veeman. Xenon self-diffusion in organic polymers by pulsed field gradient nmr spectroscopy. *Macromolecules*, 31(20):7010–7013, 1998. doi:10.1021/ma9803842. 20

[77] R. Simonutti, S. Bracco, A. Comotti, M. Mauri, and P. Sozzani. Continuous flow hyperpolarized 129xe NMR for studying porous polymers and blends. *Chemistry of Materials*, 18(19):4651–4657, 2006. doi:10.1021/cm060499h. 20

[78] A. Comotti, S. Bracco, P. Sozzani, S. Horike, R. Matsuda, J. Chen, M. Takata, Y. Kubota, and S. Kitagawa. Nanochannels of two distinct cross-sections in a porous al-based coordination polymer. *Journal of the American Chemical Society*, 130(41):13664–13672, 2008. doi:10.1021/ja802589u. 20

[79] Y. Liu, W. Zhang, S. Xie, L. Xu, X. Han, and X. Bao. Probing the porosity of cocrystallized mcm-49/zsm-35 zeolites by hyperpolarized 129xe nmr. *journal of physical chemistry B*, 112:1226–1231, 2008. doi:10.1021/jp077396m. 20

[80] N. Kato, T. Ued, H. Omi, K. Miyakubo, and T. Eguchi. Characterization of adsorbed xenon in zeolite-a, x, and y by high-pressure 129xe nmr spectroscopy. *physical chemistry chemical physics*, 6:5427–5434, 2004. doi:10.1039/B411798K. 20

[81] I. L. Moudrakovski, C. I. Ratcliffe, and J. A. Ripmeester. Application of129xe 2d-EXSY NMR to intra- and interparticle exchange in zeolites. *Applied Magnetic Resonance*, 8(3): 385–399, 1995. doi:10.1007/BF03162653. 20, 24

[82] T. Onfroy, G. Flavien, S. H. Marie-Anne, and G. Antoine. First evidence of interconnected micro and mesopores in cmk-3 materials. *Carbon journal*, 47(10):2352–2357, 2009. doi:10.1016/j.carbon.2009.04.025.

[83] E. Weiland, M. A. S. Huet, A. Nossov, F. Guenneau, A. A. Quoineauda, and A. Gedeon. Transport properties of catalyst supports studied by pulsed field gradient (pfg) and 2d exchange (exsy) nmr spectroscopy. *New journal of chemistry*, 40:4447–4454, 2016. doi:10.1039/C5NJ02952J. 20

[84] C. J. Jameson, A. K. Jameson, and J. K. Hwang. Nuclear spin relaxation by intermolecular magnetic dipole coupling in the gas phase. 129xe in oxygen. *The Journal of Chemical Physics*, 89(7):4074–4081, 1988. doi:10.1063/1.454842. 21

[85] F. Guenneau, K. Panesar, A. Nossov, M.-A. S. Huet, T. Azais, F. Babonneau, C. T. Peteilh, J.-M. Devoisselleb, and A. Gedeon. Probing the mobility of ibuprofen confined in mcm-41 materials using mas-pfg nmr and hyperpolarised 129xe nmr spectroscopy. *physical chemistry chemical physics*, 15:18805–18808, 2013. doi:10.1039/C3CP52695J. 21

[86] Q. J. Chen, J. L. Guth, A. seive, P. caullet, and J. Fraissard. 129xe and 27al n.m.r. study of high-silica zeolites synthesized in nonalkaline fluoride media: Ga, al-mfi and al-beta. *zeolites*, 11(8):798–803, 1991. doi:org/10.1016/S0144-2449(05)80058-2. 21

[87] M. A. S. Huet, F. Guenneau, A. Gedeon, and A. Corma. Probing xe exchange in delaminated zeolites by hyperpolarized 129xe nmr. *journal of physical chemistry C*, 111(15): 5694–5700, 2007. doi:10.1021/jp066163c. 21

[88] T. T. P. Cheung, C. M. Fu, and S. Wharry. Xenon-129 nmr of xenon adsorbed in y zeolites at 144 k. *Journal of Physical Chemistry*, 92(18):5170–5180, 1988. doi:10.1021/j100329a022. 21, 22

[89] A. Gédéon, J. Bonardet, C. Lepetit, and J. Fraissard. Application of 129xe nuclear magnetic resonance to the study of cu y zeolites: dehydration and redox effects. *Solid state nuclear magnetic resonance*, 5(2):201–212, 1995. doi:10.1016/0926-2040(95)00032-L. 22

[90] A. Gedeon and J. Fraissard. 129xe nmr of agx, cux, znx and cdx zeolites. comparative study of nd10 element-xenon interactions. *Chemical physics letters*, 219(5-6):440–444, 1994. doi:10.1016/0009-2614(94)00098-0. 22

[91] J. G. KIm, T. kompany, R. Ryoo, T. Ito, and J. Fraissard. 129xe n.m.r. of y^{3+}, la^{3+}, and ce^{3+} exchanged x zeolites. *Zeolites*, 14(6):427–432, 1994. doi:org/10.1016/0144-2449(94)90168-6.

[92] Q. Chen, T. Ito, and J. Fraissard. 129xe-nmr study of rare earth-exchanged y zeolites. *Zeolites*, 11(3):239–243, 1991. doi:10.1016/S0144-2449(05)80225-8. 22

[93] E. Scharpf, R. Crecely, B. Gates, and C. Dybowski. Characterization of nina-y zeolite by xe-129 nmr spectroscopy. *Journal of Physical Chem.*, 90(1):9–11, 1986. doi:10.1021/j100273a004. 22

[94] R. Shoemaker and T. Apple. Redox behavior of ruthenium in zeolite y. *Journal of Physical Chem.*, 91(15):4024–4029, 1987. doi:10.1021/j100299a020. 22

[95] N. Bansal and C. Dybowski. Effects of replacing sodium by nickel ions in y zeolite: evidence from xenon-129 nmr spectroscopy. *Journal of Physical Chem.*, 92(8):2333–2337, 1988. doi:10.1021/j100319a046. 22

[96] A. K. Jameson, C. J. Jameson, and H. S. Gutowsky. Density dependence of 129xe chemical shifts in mixtures of xenon and other gases. *The Journal of Chemical Physics*, 53(6):2310–2321, 1970. doi:10.1063/1.1674328. 23

[97] I. Moudrakovski, C. Ratcliffe, and J. Ripmeester. 2d exsy 129 xe nmr: New possibilities for the study of structure and diffusion in microporous solids. *Studies in Surface Science and Catalysis*, 97:243–250, 1995. doi:10.1016/S0167-2991(06)81895-1. 24

[98] Y. Liu, W. Zhang, Z. Liu, S. Xu, Y. Wang, Z. Xie, X. Han, and X. Bao. Direct observation of the mesopores in zsm-5 zeolites with hierarchical porous structures by laser-hyperpolarized 129xe nmr. *The Journal of Physical Chemistry C*, 112(39):15375–15381, 2008. doi:10.1021/jp802813x. 24

[99] J. Jeener and B. H. Meier. Investigation of exchange process by two-dimensional NMR spectroscopy. *The Journal of Chemical Physics*, 71(11):4546–4553, 1979. doi:10.1063/1.438208. 24

[100] R. Larsen, J. Shore, K. Schmidt-Rohr, L. Emsley, H. Long, A. Pines, M. Janicke, and B. Chmelka. Nmr study of xenon dynamics and energetics in na—a zeolite. *Chemical physics letters*, 214(2):220–226, 1993. doi:10.1016/0009-2614(93)90085-F. 24

[101] P. Tallavaara and J. Jokisaari. 2d 129xe EXSY of xenon atoms in a thermotropic liquid crystal confined to a controlled-pore glass. *Physical Chemistry Chemical Physics*, 8(42):4902–4907, 2006. doi:10.1039/B609728F. 24

[102] Y. Bai, P. A. Hill, and I. J. Dmochowski. Utilizing a Water-Soluble Cryptophane with Fast Xenon Exchange Rates for Picomolar Sensitivity nmr Measurements. *Analytical Chemistry*, 84(22):9935–9941, 2012. doi:10.1021/ac302347y.

[103] C.-Y. Cheng, J. Pfeilsticker, and C. R. Bowers. Dramatic enhancement of hyperpolarized xenon-129 2d-NMR exchange cross-peak signals in nanotubes by interruption of the gas flow. *Journal of the American Chemical Society*, 130(8):2390–2391, 2008. doi:10.1021/ja078031i. 24

Chapter 2

Hyperpolarized ^{129}Xe NMR to Study Synthetic Nanosized Zeolites

2.1 Introduction

In this chapter, we are discussing the application of hyperpolarized ^{129}Xe NMR spectroscopy to the study of several synthetic nanosized zeolites. This chapter is divided into two parts,

A) A study of the crystallization mechanism of nanosized FAU-X zeolites by hyperpolarized ^{129}Xe NMR.

B) A study of the effect of cation substitution (IA group) on the adsorption of xenon on nanosized FAU-X zeolites by hyperpolarized ^{129}Xe NMR.

Before going into the details of these study, we make a general introduction on zeolites.

2.1.1 An Introduction about Zeolites

Zeolites are microporous crystalline solids with well-defined structures. In general they contain silicon, aluminum, and oxygen in their framework. When aluminum is incorporated in the structure, a negative charge is present that must be compensated by a positive charge from proton or other cations. The most interesting feature about zeolites is their open, cage-like, "framework" structure and the way they can trap other molecules inside their porous network. These materials can be naturally occurring or be synthetic. There are about 40 natural zeolites, *e.g.*, chabazite, clinoptilolite, and mordenite etc. There are (around 150) synthetic zeolites. In the chemical industry, zeolites are among the most important families of materials with numerous applications. The success of zeolites in chemistry and chemical engineering is attributed to the presence of well-defined micropores which are responsible for molecular sieve effects. In general, zeolites are very versatile catalysts which can be tuned to achieve optimum performance in wide range of catalytic reactions,[1] *e.g.*, The availability of a wide range of different zeolites with various micropore size and connectivity, make possible to conduct shape selective catalysis with these solids. It is thus possible to proceed highly selective catalytic transformation.[1] The synthetic zeolites have been designed for various purposes, *e.g.*, zeolite A (commonly used as a laundry detergent), zeolites ZSM-5 (can be utilized for acid-catalyzed reactions), zeolites X and Y (for catalytic cracking). Different types of zeolite based materials exist which offer improved accessibility to the catalytic active sites located in the microporous crystals. They are wide pore zeolites, nanosized zeolites, zeolite composites and mesoporous zeolite crystals.[2] There are several synthesis strategies used to prepare these zeolite materials. When zeolite crystals are quite big (>500 nm) some problems of molecular diffusion can occur (in catalytic industrial applications). For that purpose, many studies have been done on the zeolite post-modification to introduce mesoporosity or even macroporosity in zeolite materials.[3,4]

2.1.2 Hierarchical Zeolites

When zeolite micropores are connected to mesopores or macropores, they are often referred as "hierarchical". There are many routes to do the hierarchization such as i) post synthesis modification by desilication[5,6] or by dealumination[7,8] or by steaming and chemical treatment[9] ii) one step hydrothermal crystallization in presence of specific organosilane surfactants which act as mesopore modifiers.

Hierarchically porous zeolites offer an effective solution to the mass transform problem associated with conventional zeolites, because they couple in a single system, the catalytic features of micropores and improved access and transport properties of additional porosity (meso- or macropores).

2.1.3 Nanosized Zeolites

Instead of hierarchical zeolites, that can also be expensive and complex in commercial application, it is also possible to decrease the diffusion pathway of molecules by using a direct synthesis of nanosized zeolite crystals with or without organic templates.[10–12] But most of these new synthesis needs an organic template in the synthesis strategy which becomes expensive and their use could be environmentally unfriendly. Recently, several zeolites have been reported in the category of template-free synthesis such as zeolites A,[13] ZSM-5,[14] K-F nanocrystal,[15], and FAU-X nanozeolite.[16] Nevertheless, some challenges are still involved in the synthesis of template-free zeolites, *i.e.*, their processing, characterization, and applications will motivate the synthetic chemist in further development.[17].

Similar to the conventional micron-sized crystals the nanosized zeolites are synthesized under hydrothermal conditions in closed vessels and no reactants are added during the reactions. Thus after the conversion of reactants in the system, the growth stops. In the synthesis of nanosized zeolites, special attention is paid to the preparation of the initial precursor system in order to favor the nucleation process. The initial precursor system in nanozeolites is highly alkaline media and low amount of water. The importance of the nucleation is due to the fact that the number of nuclei in the system determines the ultimate crystal size. Thus, an abundant nucleation leads to very small crystals while if the system yields a few viable nuclei the crystals formed are large.[17]

2.2 Study of the Crystallization in Nanosized FAU Zeolites

2.2.1 Faujasite Zeolites

Faujasite zeolites consist of sodalite cages which are connected through hexagonal prisms. In this type of zeolite, pores are arranged perpendicular to each other. The pores which are formed by 12-membered ring (12 MR.) channels which means that there are 12 cations (Si^{4+} and Al^{3+}) and 12 O^{2-} anions present in the ring. The inner cavity has a diameter of 11.8 Å and is surrounded by 10 sodalite cages. The pore opening diameters for supercage and sodalite cages are 7.5 Å and 2.5 Å, respectively.

For the synthesis of FAU zeolites, sodium aluminate used as alumina source and sodium silicate as a silica source. Faujasite zeolites are commonly separated into two classes: Faujasite X (FAU-X) having a Si/Al ratio between 1 and 1.5 and Faujasite Y (FAU-Y) having a Si/Al ratio above 1.5.

FAU zeolites have enormous potential as cracking catalysts, due to the presence of three-dimensional framework arrangements.[18]

2.2.2 Preparation of Nanosized Zeolite X

The synthesis of nanosized zeolite FAU-X with a particle size of 10-15 nm was performed according to the procedure published elsewhere.[16] The starting chemical composition of the precursor suspension was: $9Na_2O : 1.1Al_2O_3 : 10SiO_2 : 122H_2O$. The precursor suspension was aged for 24 h at room temperature followed by dehydration as shown in the figure 2.1. Thus reaching the

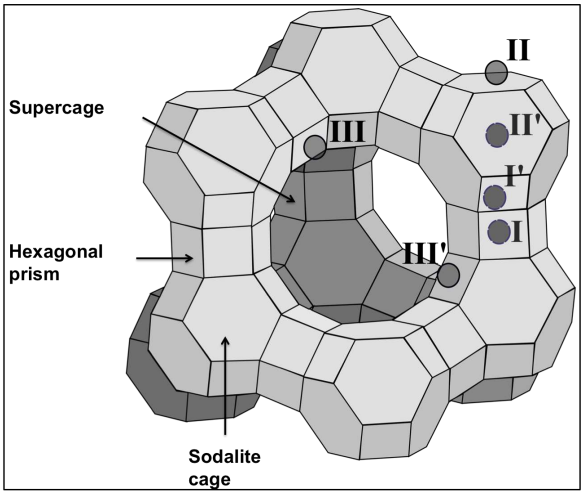

FIGURE 2.1: Faujasite zeolite structure showing the supercage, sodalite cage and hexagonal prism. The corners denote the position of T sites (T= Si or Al). Different cation positions are indicated by Roman numerals.

final chemical composition of the precursor suspension: $9Na_2O : 1.1Al_2O_3 : 10SiO_2 : 50H_2O$, and subsequently subjected to hydrothermal treatment at 323 K for 24 h. The nanosized zeolite was purified by high-speed centrifuge until pH of 8 was reached.

In this section, we studied the development of the porosity of the FAU materials at different stages starting from the mixing of the reactants to the fully crystalline sample.

The synthesis stages involved in this study are as following:

- ☐ **Stage 1**. Preparation of water clear solutions A (sodium aluminate) and B (sodium silicates), followed by their controlled mixing leading to the formation of a clear precursor suspension.

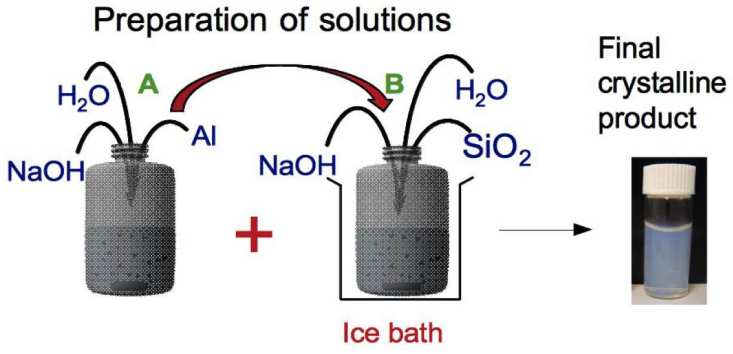

SCHEME 2.1: nanosized Faujasite X zeolite synthesis scheme with A-(sodium aluminate) and B-(sodium silicate) to obtain the crystalline FAU-X zeolite.

- ☐ **Stage 2**. Aging of clear precursor suspension for 24 h at room temperature (RT).

- ☐ **Stage 3**. Control of water content in the clear precursor suspension by dehydration (181 K, P=0.02 mbar) leading to the removal of 60-63% water.

- ☐ **Stage 4**. Maturation of the material using a hydrothermal treatment of the dehydrated precursor suspensions (polypropylene (PP) reactors in a conventional oven at 323 K for 45 min, 3 h and 24 h), called **NaX-45min, NaX-3h and NaX-24h** respectively.

- ☐ **Ion exchange**. The nanosized LiX sample was prepared through ion exchange method. Typically, 1 g of zeolite powder was stirred in 35 mL of lithium nitrate solutions with concentrations of $1\,mol \cdot L^{-1}$. The process was repeated for 3 times at room temperature by separating the supernatant from parent liquid, re-dispersing in metal nitrate solution and carrying on with aforementioned ion exchange process to ensure that the highest possible ion exchange was achieved. The samples after ion-exchanged were then washed thoroughly (pH=8) prior to freeze-drying for further characterization.

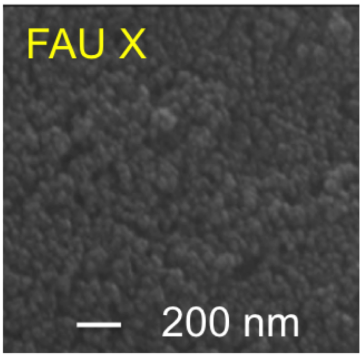

FIGURE 2.2: SEM image for nanosized FAU-X zeolite, with a particle size of 10-15 nm.

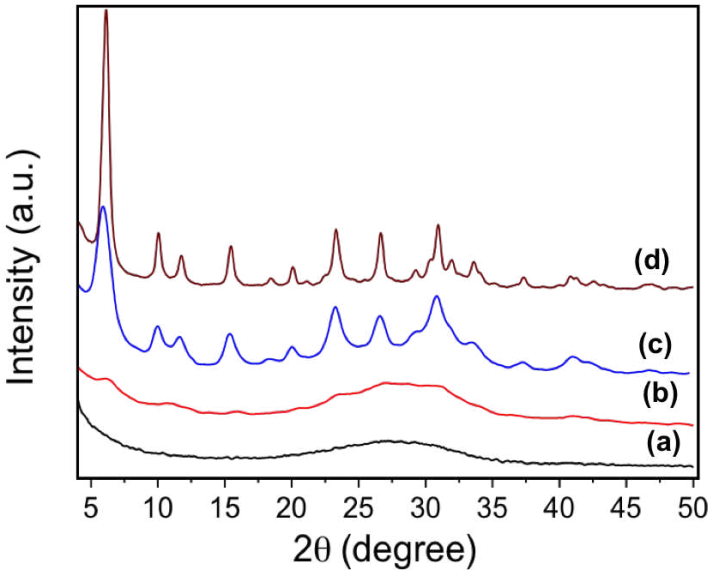

FIGURE 2.3: PXRD pattern showing variation from Initial stage to final stage of crystallinity, (a) stage 1, (b) stage 3, (c) NaX-3h, (d) NaX-24h

2.2.3 Results and Discussion

The crystallinity of the samples extracted at different steps was measured by XRD as shown in the figure 2.3. The diffraction pattern of the sample extracted after stages 1 and 3 contains a broad peak centered at 27° 2θ, which is typical for amorphous aluminosilicate. Further, the XRD pattern of the NaX- 3h sample contains diffraction peaks at 6.1, 11.7, 15.4, 23.5, 26.6 and 30.8° 2θ that correspond to the FAU framework type structure with [hkl] values of [111], [113], [226], [246] and [157], respectively. After continuous hydrothermal treatment (HT) for 24 h, a fully crystalline zeolite sample is obtained.

The porosity and specific surface area of the samples were characterized by nitrogen adsorption measurements and the values are reported in Table 2.1. In that table, the degrees of crystallinity

are also reported. On the first stage, microporosity is not observed and a very small specific area is measured, which is consistent with a totally amorphous sample. Only at stage 3, the sample presents a BET surface area of $350\,m^2 \cdot g^{-1}$, and a little amount of microporosity starts to be created ($0.05\,cm^3 \cdot g^{-1}$), while it is also observed an increase of the mesoporosity. After 3 h, the microporosity is still very low, while the crystallinity measured by XRD reach 50%.

The full microporosity and 100% of crystallinity is obtained only after SI24h. The fully crystallized sample possesses a micro volume of $0.31\,cm^3 \cdot g^{-1}$.

^{29}Si MAS NMR are reported in Figure 2.4. The spectrum obtained for stage 1 show a broad signal corresponding to an amorphous phase. In stage 2, a tiny peak appears at -85 ppm, which can be attributed to the beginning of an arrangement between Si and Al atoms, and increases during the crystallization process.

Finally, a resolved spectrum is obtained for NaX-24h sample with two peaks at -84.7 ppm and -89.5 ppm corresponding to a totally crystallized X zeolite with a Si/Al ratio of 1.06 (see Table 2.1).

Due to the presence of a great amount of sodium during the synthesis, the study of ^{23}Na by NMR can give information about their location and then the type of surroundings. Indeed, ^{23}Na MAS NMR is known to show the position of sodium in the different cavities of faujasite X and Y after dehydration.[19,20] The different sodium locations known in faujasite and their usual labeling are reported in the figure 2.1.

The different stages of crystallization of the NaX zeolite were studied by ^{23}Na MAS NMR and the spectra are presented in the figure 2.5.

In the fully crystallized sample, *i.e.*, NaX-24h, a typical spectrum for NaX is obtained. The modeling of this spectrum, using the DMFIT software[21] and quadrupolar line shapes, is shown in the figure 2.6. It can be used to attribute a location to the sodium in the different faujasite cavities (I for the Hexagonal prism, $II - I'$ for sodalite cages and $III - III'$ for supercages) .[19]

Table 2.1: Properties of the NaX samples at different stages of crystallization

	V_{micro} $(cm^3 \cdot g^{-1})^a$	V_{meso} $(cm^3 \cdot g^{-1})^a$	S_{BET} $(m^2 \cdot g^{-1})^a$	Si/Al^b	crystallinity $(\%)^b$
Stage 1	0.00	0.24	230	-	-
Stage 3	0.05	0.83	350	-	23
NaX-3h	0.03	1.21	360	1.41	50
NaX-24h	0.31	1.23	870	1.06	100
LiX	0.32	1.25	880	1.06	100

^{a} t-plot method. ^{b}Crystallinity determined by NMR

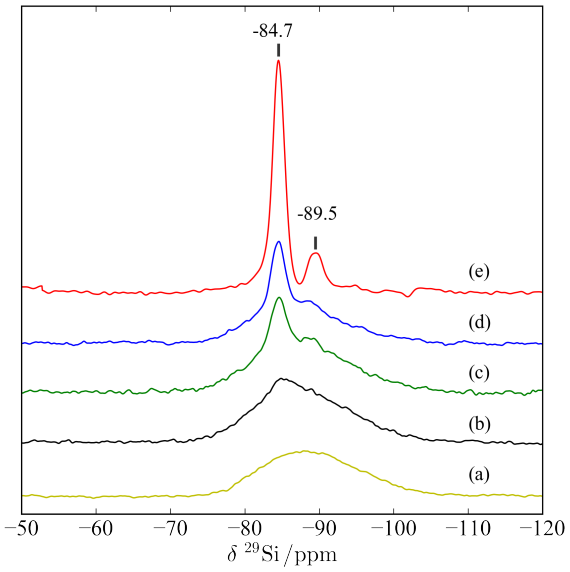

FIGURE 2.4: ^{29}Si MAS NMR of samples at (a) stage 1; (b) stage 2; (c) NaX-45min; (d) NaX-3h and (e) NaX-24h at room temperature.

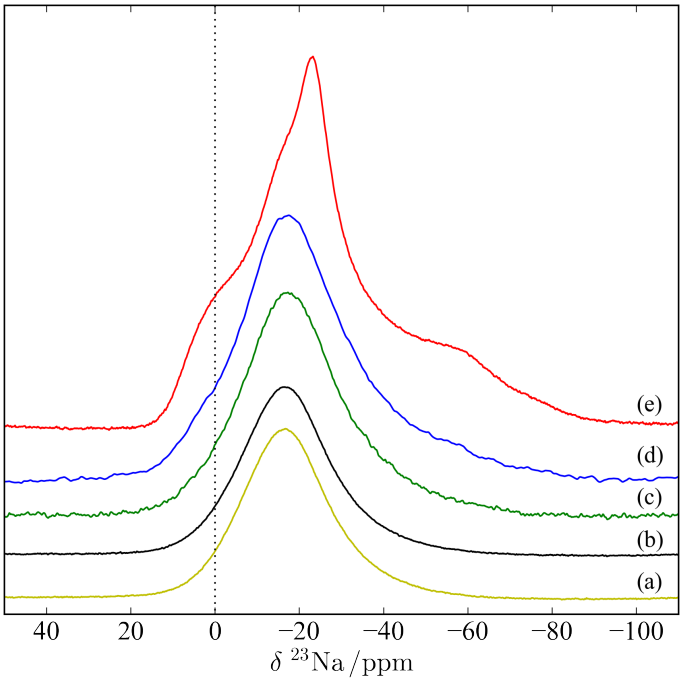

FIGURE 2.5: ^{23}Na MAS NMR of samples at (a) stage 1, (b) stage 3, (c) NaX-45min, (d) NaX-3h and (e) NaX-24h dehydrated at 548 K.

The spectrum obtained for the sample at stage 1 (Fig. 2.5) shows only a broad peak at −15 ppm which may correspond to sodium located in large cavities starting to form. It is interesting that this broad peak is very similar to the line of sodium in the later stage of crystallization. One could conclude that at the early stage, right after mixing of the components, some embryonic

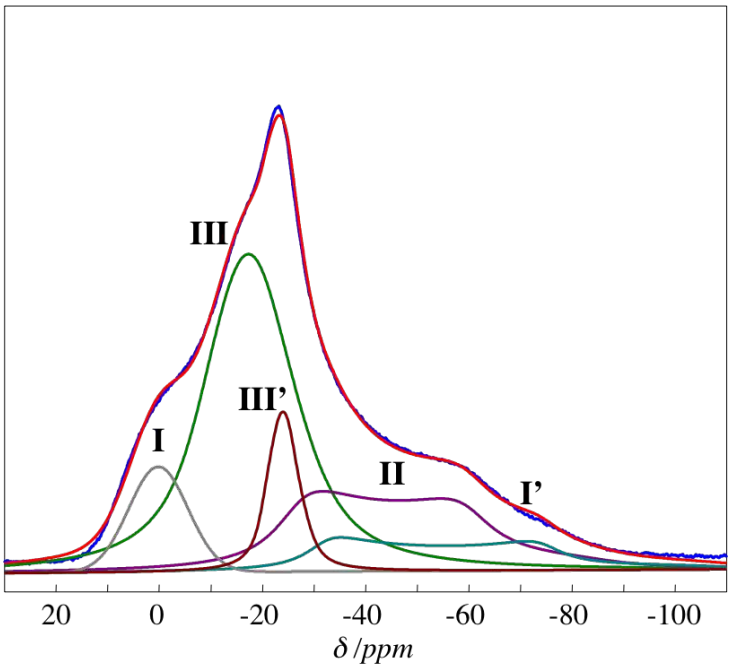

FIGURE 2.6: ^{23}Na MAS NMR Fit for the stage NaX-24h

zeolitic entities (likely the hexagonal prisms) start to form, and sodium can already be close to site III in this phase.

During the crystallization process, shoulders appear at lower and higher frequencies with respect to the peak at -15 ppm. These shoulders are difficult to observe directly, but difference spectra can be realized between the spectra at each step and the one obtained after stage 1. These difference spectra are shown in the figure. 2.7

These difference spectra highlight the presence of two signals, a relatively narrow signal around 0 and, another broader signal with a gravity center around -40 ppm and a typical quadrupolar line shape ranging between -20 ppm to -100 ppm . For NaX at stage 3, the result of the model fitting is given in figure 2.8. With this modeling, and using previous attribution in literature[19], we can say that the two peaks around 0 and -40 ppm , correspond to sodium located in hexagonal prisms and (I) and in sodalite (II), respectively. This proves that the SBU's are present at stage 3, but also in lower concentration in the earlier stage of crystallization (Fig. 2.5).

To go further into the understanding of the first step of the crystallization of these nano-X crystals, continuous flow HP ^{129}Xe NMR experiments by varying the temperature were performed. The xenon adsorption can be studied by two methods by changing the pressure or by temperature. Higher pressure and lower temperature were shown to act in parallel, where the choice of using higher pressure needs a special instrumental setup. The corresponding xenon adsorption spectra for fully crystalline (NaX-24h) sample and for the sample after Li exchange is shown in (Fig. 2.10). As shown in the (Fig. 2.10) xenon adsorption at high temperature shows presence

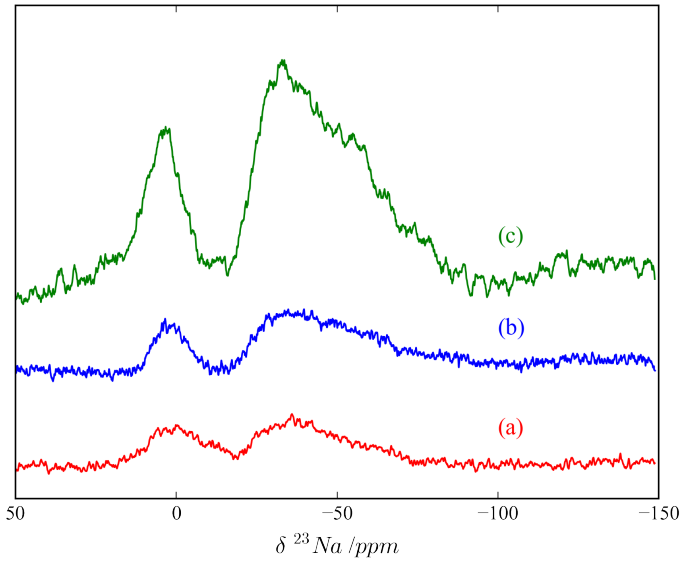

FIGURE 2.7: ^{23}Na difference spectrum between stage 1 and (a) stage 3, (b) NaX-45min and (c) NaX-3h

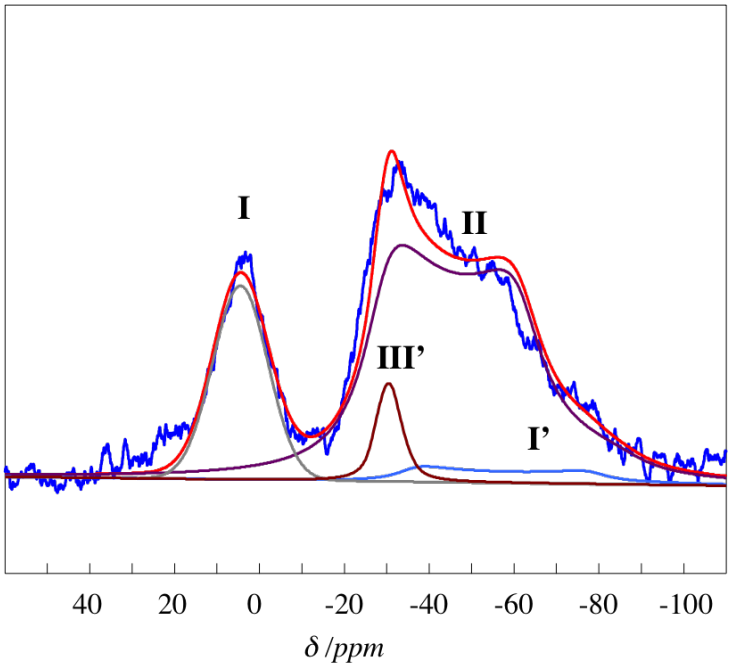

FIGURE 2.8: ^{23}Na MAS NMR Fit of the difference spectrum between stage 1 and NaX-3h

of one peak which is for xenon adsorbed in one cavity, and with decrease in temperature xenon adsorption shows a presence of new peak which clearly seen at 300 K this spectra further used in analysis. A comparison of the spectrum for HP- ^{129}Xe NMR experiments done at 300 K is reported in the figure 2.9.

Signal obtained for the sample at stage 1 (Fig. 2.9-a) shows a broad peak at 80 ppm . Such high chemical shift is only possible if the xenon is confined in a small space. This result indicates that some porosity is formed already at this first stage. This supports the observation also made

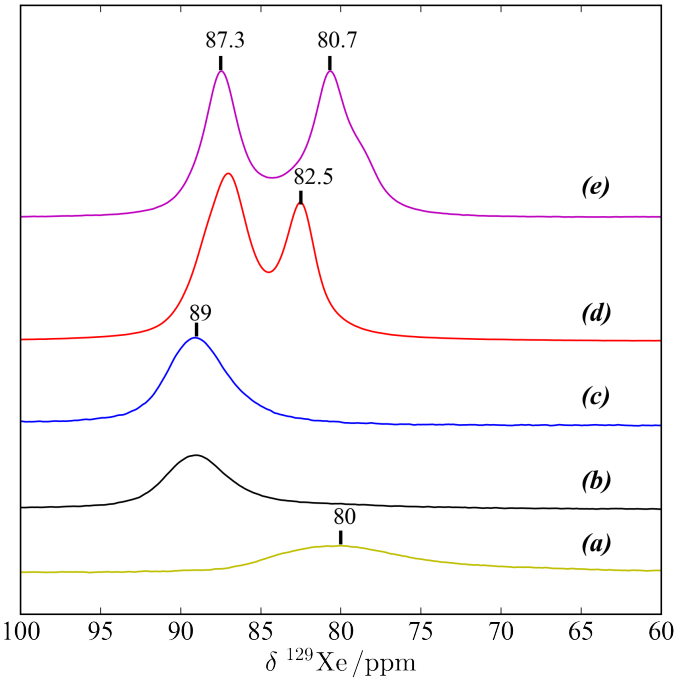

FIGURE 2.9: ^{129}Xe NMR spectra of samples at (a) stage 1, (b) stage 2, (c) NaX-3h, (d) NaX-24h and (e) LiX at 300 K

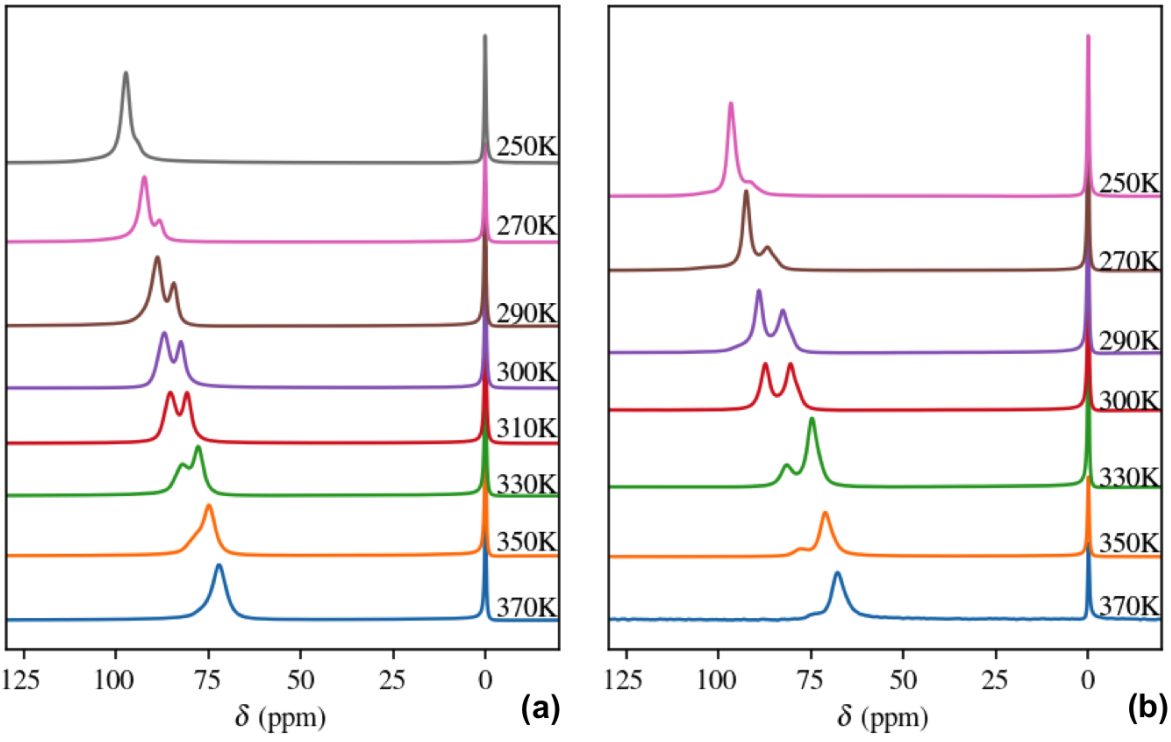

FIGURE 2.10: Variable temperature 1D HP ^{129}Xe NMR spectra of (a) fully crystalline sample (NaX-24h) and (b) fully crystalline sample after Li exchange (LiX)

previously for sodium which also shows that the cations are also confined in some cavities. The broadness of the signal seems to show a rather large heterogeneity in size of those cavities.

At later stages of crystallization between stages 2 and 4 (3h) Figure (2.9-b,c), a narrower signal appears at higher chemical shift around 89 ppm . The corresponding cavities where the xenon is confined are thus smaller. This is in a good agreement with the data obtained for ^{29}Si MAS NMR where a beginning of arrangement between Si and Al atoms is observed after stage 2(figure 2.4).

For the fully crystalline sample, *i.e.*, stage for NaX-24h, the spectrum shows the presence of two peaks (figure 2.9-d). This is a surprising result as in faujasite structure, only the larger supercage cavity can be accessed by the xenon atom. Indeed, its kinetic radius around 4.4 Å generally prevents adsorption in the sodalite cages whose opening is only a six-membered ring (2.5 Å).

One explanation could be that due to the small size of the crystal (10-15 nm), a relative large number of sodalite cages, not fully closed and located for example at the external surface could be entered by the xenon molecules. Thus the two peaks could correspond to xenon confined in the two cavities present in faujasite structure: i) the supercage with chemical shift at 82.5 ppm and ii) the "accessible" sodalite cage at 87.3 ppm .

In an attempt to confirm this interpretation, we performed a lithium-exchanged of the fully crystallized sample. Indeed, it is known that the sodium trapped in sodalite cannot be easily exchanged with other cation, even a smaller cation such as lithium. In the contrary, an easy exchange occurs when sodium is in the supercage. The ^{129}Xe spectrum achieved on this lithium-exchanged sample is reported in Figure (2.9-e). Interestingly, it also shows two main resonances, with the one at 87.3 ppm attributed to open sodalite, which has not shifted with respect to the Na -form of the X zeolite. The resonance at 80.7 ppm can be attributed to supercage. With

Table 2.2: Chemical shift vs temperature

T (K)	Na-X δ ^{129}Xe ppm		Li-X δ ^{129}Xe ppm	
	sodalite cage[a]	supercage[b]	sodalite cage[a]	supercage[b]
370	–	72.2	74.5	68.1
350	78.8	74.9	78.3	71.3
330	82.3	77.8	81.9	74.9
310	85.5	80.8	–	–
300	87.3	82.5	87.3	80.7
290	88.6	84.2	89.1	82.7
270	92.3	88.1	92.6	86.8
250	97.3	94.1	96.7	91.3

[a]Chemical shift of ^{129}Xe adsorbed in sodalite cage; [b]Chemical shift of ^{129}Xe adsorbed in supercage.

respect to the NaX it is shifted to a smaller chemical shift. The latter observation could be explained by an increase of free space in the supercage as lithium cation is smaller than sodium, or by a different electronic interaction with lithium with respect to sodium .

In order to confirm how the sodalite can be accessible to xenon in such nanosized faujasite crystal, 2D-EXSY NMR experiments were performed at 330 K on the crystalline sample, and the spectra are reported in the figure 2.11. On the 2D EXSY spectrum obtained with low mixing time (10 ms), cross-peaks between the gas phase at 0 ppm and the sodalite peak at around 82 ppm are observed. This confirms that the xenon can enter directly in the sodalite from the free gas, without passing by the supercage, as it would be expected if the sodalite were accessible internally through the 6 members ring (even with damaged 6-member rings). With this mixing time, no connectivity between sodalite cage and supercage are observed but signal on the diagonal for the supercage is present. Surprisingly, we do not observe a cross-peak between supercage and the free gas, which may be due to the fact at such low temperature and due to the low partial pressure of the xenon, only the open sodalite (the smallest cavities with the largest van-der-waals interaction) are filled.

With an increase of the mixing time (the same temperature and 100 ms) a cross peak out of the diagonal is visible. But we do not observed a cross peak between supercage-sodalite cage, which gives a non symmetric EXSY spectra. The nature of this non symmetric EXSY can be explained, as we are working with continuous flow ^{129}Xe HP experiments where exchange between two cavities take place very fast. Even due to the nano crystal size where xenon enter into the sodalite cage occupied the sodalite cage where no more exchange can take place between supercage-sodalite cage. Which proves nanosized zeolite present a higher flexibility than when the faujasite have micron size.

2.2.4 Conclusions

Combined ^{29}Si, ^{23}Na and HP-^{129}Xe NMR analyses, complemented by XRD, N_2 sorption analyses, were employed to get more insight on the process of the crystallization of FAU-X nanosized zeolites. This study can be summarized into two main new observations:

i) The microporosity starts to be formed immediately after mixing of the synthesis materials.

ii) In a synthetic nanosized FAU-X zeolite, during crystallization process, hexagonal prism and then sodalite cage formed whereas the supercage is fully formed only at the later stage.

Along with the chemical changes in a system, considerable evolution of a structure is observed by a presence of broad peak for the initial stage in ^{29}Si MAS NMR which fully evolved with stoichiometric zeolite composition.

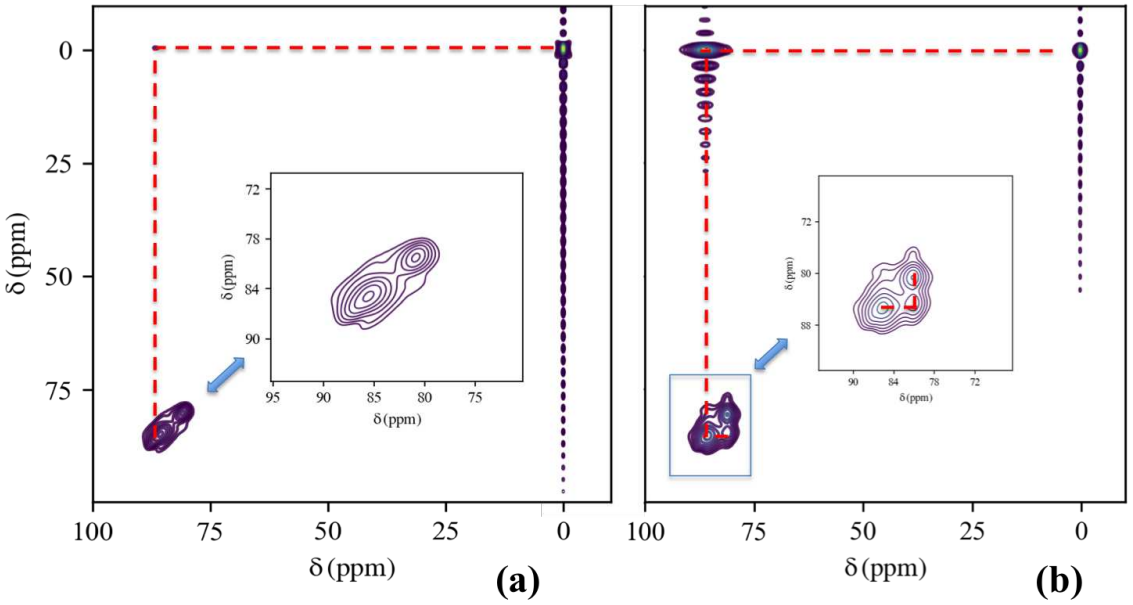

FIGURE 2.11: 2D EXSY with mixing time of (a) 10 ms and (b) 100 ms for FAU fully crystalline sample at 330 K

2D EXSY HP-^{129}Xe NMR spectra allow to analyze the traveling of the xenon molecule between the gas phase and the supercage/sodalite cages. Interestingly, with increasing the mixing time, connectivity between sodalite cage and supercage is well observed, which is due to the small size of zeolite particles and flexibility of the structure.

Apart from these observations related to basic aspects of zeolite crystallization, the present study reveals the high sensitivity of HP ^{129}Xe NMR to study the nanosized zeolite.

2.3 Study of the Cation Substitution in Nanosized FAU-X zeolite

In this section, we are discussing the effect of cation substitution on the adsorption of xenon on nanosized FAU-X zeolites. The cations used for the substitutions are Li^+, K^+, Rb^+ and Cs^+.

2.3.1 Preparation of Nanosized FAU-X Zeolite With Different Cations

For the cation exchange study, the Li-X, K-X, Rb-X, Cs-X nanozeolites were prepared through ion exchange method. Typically, 1 g of zeolite powder was stirred in 35 mL of nitrate solution of the targeted metal cations with concentrations of 0.2 M for Li-X and K-X, and 0.005 M for Rb-X and Cs-X. These concentrations were chosen to be suitable for zeolite structure and to avoid the formation of amorphous materials. The exchange process was repeated for 3 times by separating the supernatant from mother liquid, re-dispersing in metal nitrate solution and carrying on with an aforementioned ion exchange process to ensure that the highest possible ion exchange was achieved. The samples after ion-exchanged were then washed thoroughly (pH=7.5) prior to freeze-drying.

2.3.2 Results and Discussion

A series of classical analysis were performed on the new ion-exchanged sample. The degree of crystallinity and phase purity of FAU zeolite ion-exchanged nanoparticles were characterized by X-ray diffraction. The corresponding patterns for all zeolite samples are reported in the figure 2.12. They are similar to the original sample NaX. Moreover, the line width is preserved after the different Li, K, Rb, and Cs-X samples, revealing that the degree of crystallinity and the phase purity do not change after ion exchange. Besides, Field Emission Scanning Electron Microscopy (FE-SEM) analysis on these five samples was done, in order to characterize general morphology of samples. The micrographs are presented in the figure 2.13. SEM pictures reveal that the size and morphology of zeolite nanoparticles retain stable after ion exchange, without any agglomeration and formation of amorphous particles. All the crystals have a narrow particle size distribution and diameter of 10-20 nm.

The porosity of zeolite nanosized crystals after ion exchange was probed by N_2 sorption analysis. All samples exhibit type-I isotherm at low P/P_0, which is characteristic for microporous materials as shown in the figure 2.14. A high adsorption uptake at P/P_0 >0.8 is due to the textural mesoporosity resulting from the close packing of zeolite nanoparticles. From the N_2 sorption isotherms, it can be seen that the N_2 uptake at low P/P_0 is inversely proportional to the cation size (around 1.3 Å for K^+ to 3.3 Å for Cs^+) (see inset in 2.14). The Na-X zeolite exhibits the highest BET surface area and pore volumes (both V_{micro} and V_{meso}), whereas after exchange

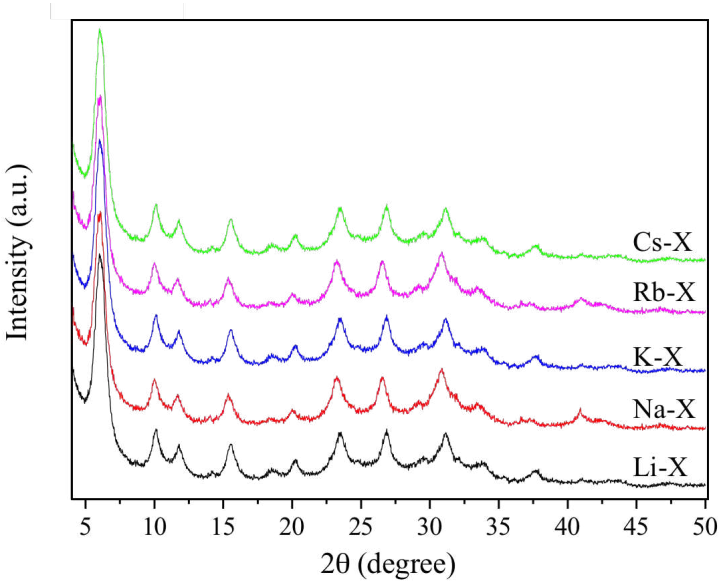

FIGURE 2.12: XRD pattern shows even after the cation exchange crystallinity is well preserved for all the cation exchange zeolites

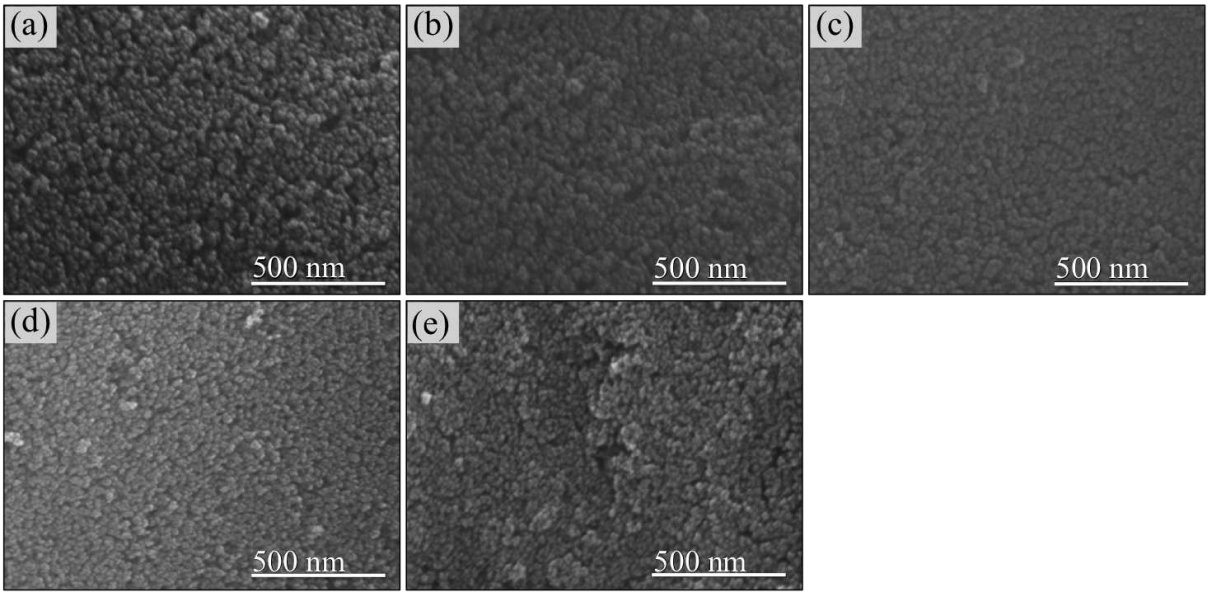

FIGURE 2.13: SEM image shows that, for all the cation exchanged samples, size and morphology remain stable : (a)=Li-X, (b)=Na-X, (c)=K-X, (d)=Rb-X, (e)=Cs-X

a decrease of the surface area is observed for all the other cation content (Table 2.3). The microporosity volume decrease is also in agreement with the increase of the size of the cation. Thus, the results from nitrogen sorption demonstrate that the porosity is slightly affected by the size and the number of cations introduced in zeolite X via ion exchange.

^{23}Na MAS NMR was used on the hydrated sample in order to probe the sodium amount that remains in each ion-exchanged sample. The ^{23}Na spectra on hydrated samples are shown in the figure 2.16. The spectra are normalized with the amount of sample used for each experiment.

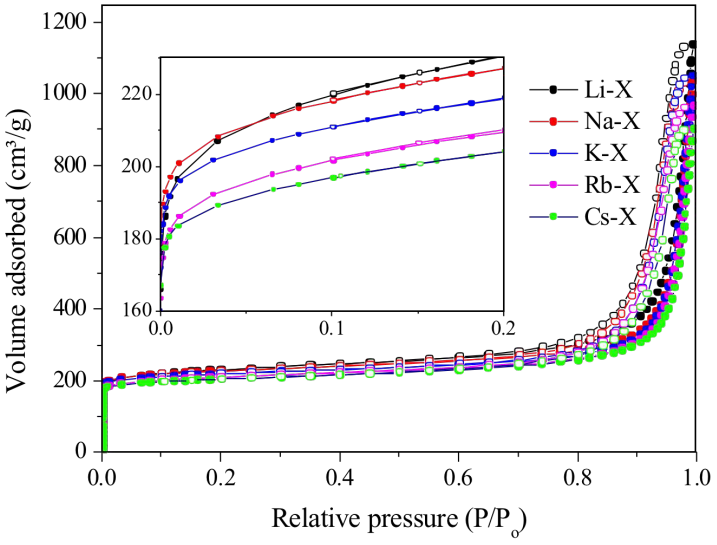

FIGURE 2.14: N_2 sorption isotherms for nanosized X zeolites exchanged with alkaline cations Li-X, Na-X, K-X, Rb-X and Cs-X shows type I isotherm. magnified part reveals a slight change in micro-porosity at low pressure

The loss in mass obtained from the thermogravimetric analysis (TGA) (figure 2.17) can be used

TABLE 2.3: Properties of cation exchange in Nanosized X samples.

	Li-X	Na-X	K-X	Rb-X	Cs-X
V_{micro} $(cm^3 \cdot g^{-1})^a$	0.310	0.310	0.295	0.285	0.280
V_{meso} $(cm^3 \cdot g^{-1})^a$	1.06	1.23	1.14	1.10	1.08
S_{BET} $(m^2 \cdot g^{-1})^a$	830	870	815	805	800
Si/Al^b	1.06	1.06	1.12	1.14	1.13
Sodium (%)^c	20.3	100.0	11.3	46.7	73.5
δ ^{129}Xe (ppm) sodalite cage^d	87.4	87.3	90.9	-	-
δ ^{129}Xe (ppm) supercage^e	80.7	80.3	85.3	89.5	96.3

^{a} *t*-plot method. ^{b}Si/Al ratio determined by NMR for cation exchanged X zeolites. ^{c}Amount of Na % remained in the sample by ^{23}Na MAS NMR. Na-X used as a reference sample. ^{d}Chemical shift of adsorbed ^{129}Xe in sodalite cage ^{e}Chemical shift of adsorbed ^{129}Xe in supercage at 300 K.

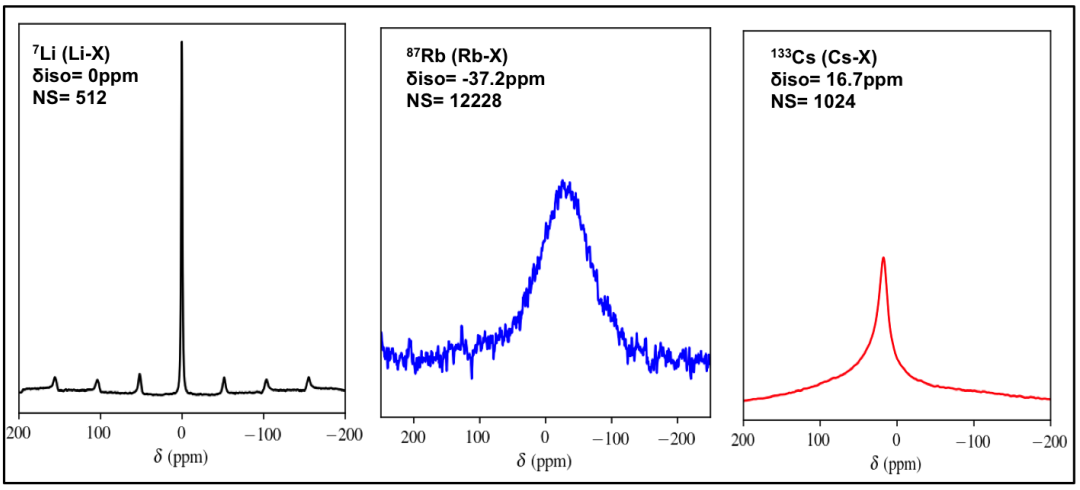

FIGURE 2.15: ^{7}Li,^{87}Rb,^{133}Cs MAS NMR obtained on cation exchange samples

to calculate the amount of Na remained in the sample after cation substitutions. The detailed calculations are shown in Appendix A. All data are reported in Table 2.3. This analysis shows that, after four cycles of ion exchange at room temperature, sodium was partially removed for the Li-X, K-X, Rb-X, and Cs-X zeolites. Indeed, in all cases, never fully exchanged materials are obtained. The highest degree of exchange of Na-X is achieved for K^{+} (88.7 %), followed by Li^{+} (79.7 %), Rb^{+} (53.3 %) and Cs^{+} (26.5 %) as shown in Table 2.3. The different ionic radius of these monovalent cations explain the various degrees of ion exchange of Na in zeolite X.

Additional analysis by ^{7}Li, ^{87}Rb and ^{133}Cs MAS NMR were also performed and all show the presence of lithium, rubidium or cesium cations adsorbed inside the structure as shown in figure 2.15.

A high-resolution magic angle spinning (MAS) NMR experiments were also used to get structural information in nanosized X zeolites. A comparison with all cation substituted samples by ^{27}Al and ^{29}Si MAS NMR spectra is shown in figure 2.18 and 2.19. ^{27}Al MAS NMR spectra show the presence of tetrahedral alumina (AlO_4) sites. No extra framework was observed at 0 ppm even after ion exchange, which is in agreement with the previous observation made by XRD. (figure 2.12) The ^{29}Si MAS spectra show a well-resolved spectrum with two peaks. The one at −85 ppm corresponds to Q^4(4Al) and the other at −89 ppm corresponds to Q^4(3Al,1Si) which is in a good agreement with nanosized X zeolites.[16] Decomposition of the ^{29}Si MAS NMR spectra obtained with the different cation was used to get the Si/Al ratios. The data, shown in Table 2.3, are in good agreement with the initial NaX material and with X faujasite in general, *i.e.*, a Si/Al ratio of around 1.1. Thus, ^{27}Al MAS NMR and ^{29}Si MAS NMR results proved that even after the cation substitution, the framework zeolite structure is preserved.

As presented in the beginning of this chapter (2.2.2), the schematic structure of zeolite X and the potential positions (I, I′, II, II′, III, and III′) to be occupied by its charge compensating

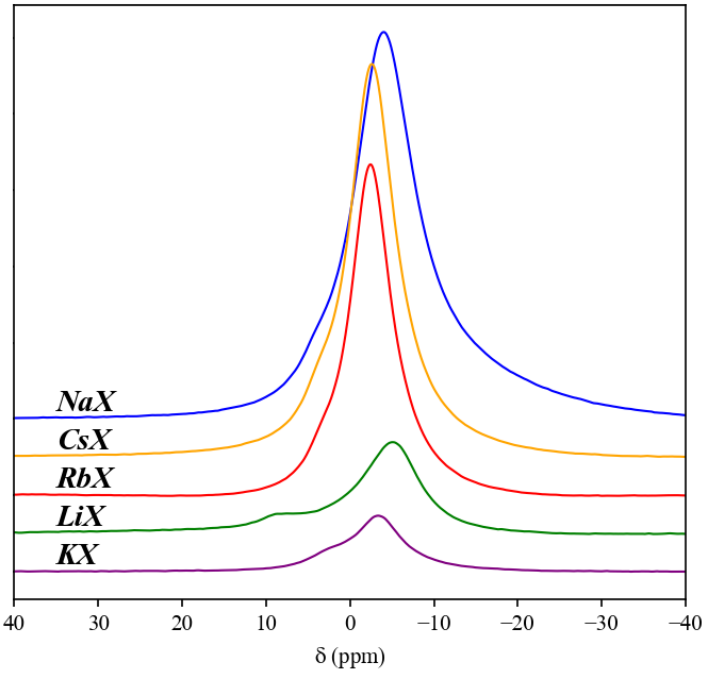

FIGURE 2.16: ^{23}Na MAS NMR obtained on hydrated samples

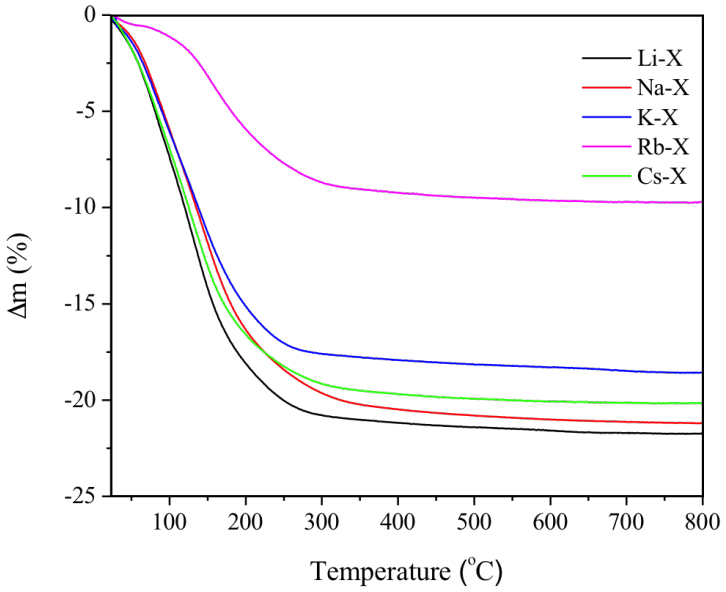

FIGURE 2.17: TGA analysis shows the loss in mass for all cation exchanged zeolites

cations (figure 2.1) can be followed by ^{23}Na MAS NMR but only on the dehydrated form. Thus, in this study, we performed dehydration on all the samples before ^{23}Na MAS NMR experiments to localized sodium after the different ion exchange.

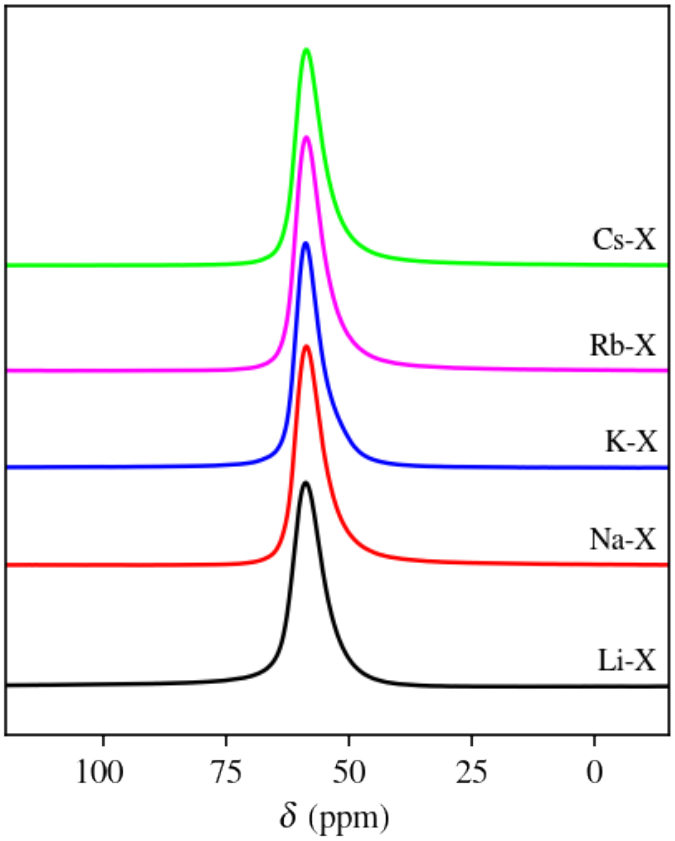

FIGURE 2.18: ^{27}Al MAS NMR obtained on hydrated samples

^{23}Na MAS NMR spectra obtained on dehydrated samples are shown in the figure 2.20. As expected by the size of the cation Rb and Cs and the previous observation on the hydrated form, no huge change occurs in the spectra of these both zeolites. A decrease of the peak corresponding to sodium located in position III at around - 20 ppm is observed, and a change in the shape of the peaks corresponding to the sodalite between −30 and −90 ppm. Thus the presence of Rb and Cs is expected to be located mainly in the supercages.

For the other two samples, some surprising observations can be made. It is usually accepted that in micron sized crystal of faujasite, only the sodium of the supercage can be exchanged.[22] Here, we can observe that almost only sodium in the hexagonal prism, corresponding to the peak at around 0 ppm , remains in KX structure. For lithium, the shape of the peak is comparable to sodium in a very symmetrical environment and could indicate that the lithium and the sodium coexist in the same environment. Indeed, it is clear that the nanozeolite presents unusual comportment regarding the ion exchange.

To get better insights on how the cation substitution affects on this cage, we performed continuous flow HP- ^{129}Xe NMR experiments with variable temperature method. The figure 2.21 shows comparison spectra of all cation exchange samples at 300 K.

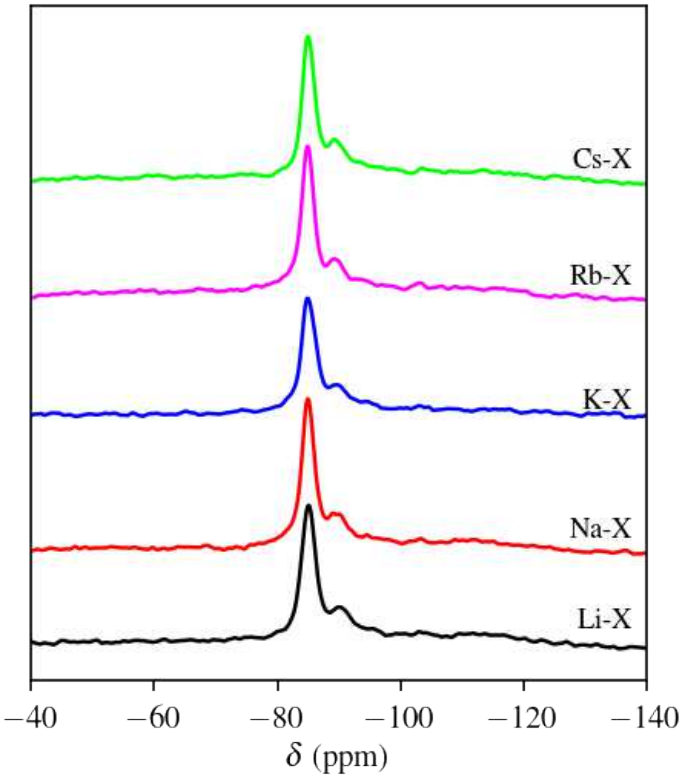

FIGURE 2.19: ^{29}Si MAS NMR obtained on hydrated samples

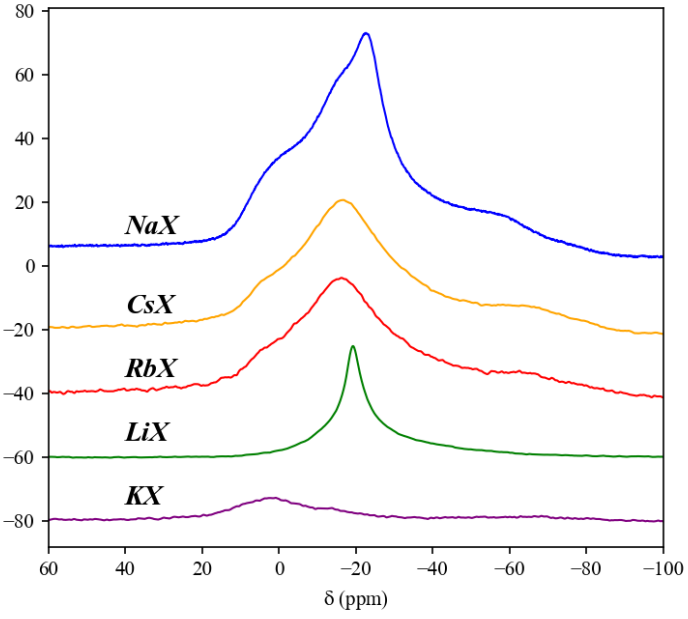

FIGURE 2.20: ^{23}Na MAS NMR on cation exchanged sample dehydrated at 548 K

All the signals at 300 K show the presence of the xenon adsorbed in various cation exchanged samples. In the case of parent zeolite sample Na-X, the presence of two signals belongs to the xenon adsorbed in sodalite cage and that in the supercage as reported in the first part of this

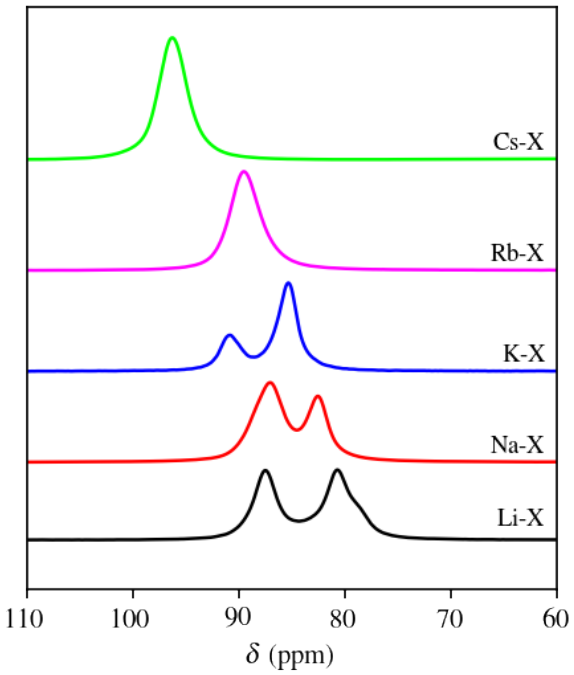

FIGURE 2.21: Comparison of 1D HP-^{129}Xe NMR spectra of cation substituted zeolite X at 300 K. The chemical shift values are reported in Table 2.3. The xenon gas signal (not shown here) at 0 ppm was used as a reference peak.

chapter (Section 2.2.3). For the Li-X sample, we have also observed the presence of xenon in two cages with almost similar chemical shit. As commented with the data obtained by ^{23}Na NMR, the shape of the spectrum is definitely attributed to the presence of lithium and sodium in the same cages. Moreover, the presence of xenon in the sodalite cages is only possible if this cage is opened and still accessible for adsorption of xenon. The sample exchanged with potassium also shows a presence of two signals with the same observations, *i.e.*, xenon adsorbed in sodalite cage and in the supercage. The shift on both peaks is connected with the presence of a bigger cation in these two cages which decrease the volume space accessible to xenon. For the sample Rb-X and Cs-X, the adsorption of xenon seems to be only possible in one cage. We expect that the only cage accessible to xenon for these two sample is the supercage. The ^{23}Na NMR data showed that the substitution of the sodium by these cation takes place in the supercages. Moreover, the shift observed to the higher chemical shift from Li-X to Cs-X is consistent with the increase of the size of the cation. Nevertheless, no peaks of xenon in sodalite are observed. This can be explained by the presence of cesium cation at the entrance of the sodalite or even by a decrease of the flexibility due to stabilization with bigger cations.

In the lithium exchanged sample (Li-X) 2D EXSY spectrum obtained at 330 K with low mixing time, *i.e.*, with 10 ms, cross-peak between the gas phase at 0 ppm and the sodalite peak at around 82 ppm are observed figure 2.27. Thus, as for the Na-X sample, xenon can then enter from the gas phase directly in the sodalite without passing by the supercage. With this mixing time,

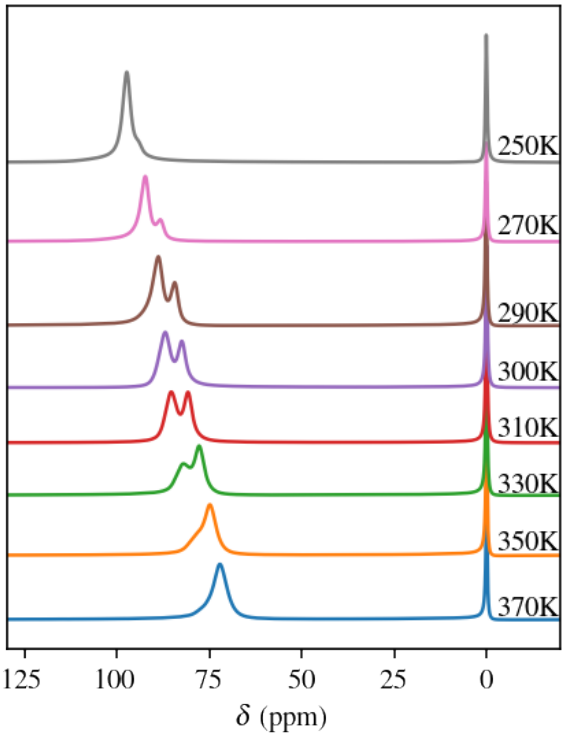

FIGURE 2.22: Variable temperature 1D ^{129}Xe NMR spectra of Na-X.

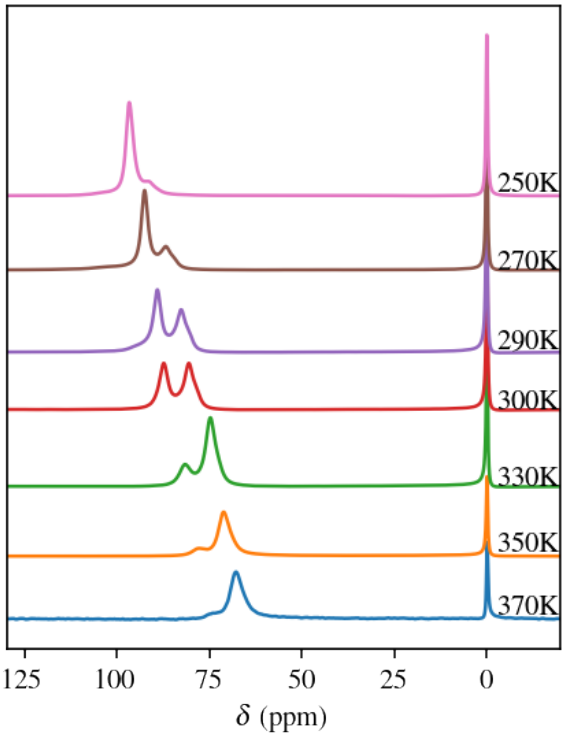

FIGURE 2.23: Variable temperature 1D ^{129}Xe NMR spectra for the sample after Lithium exchange (Li-X).

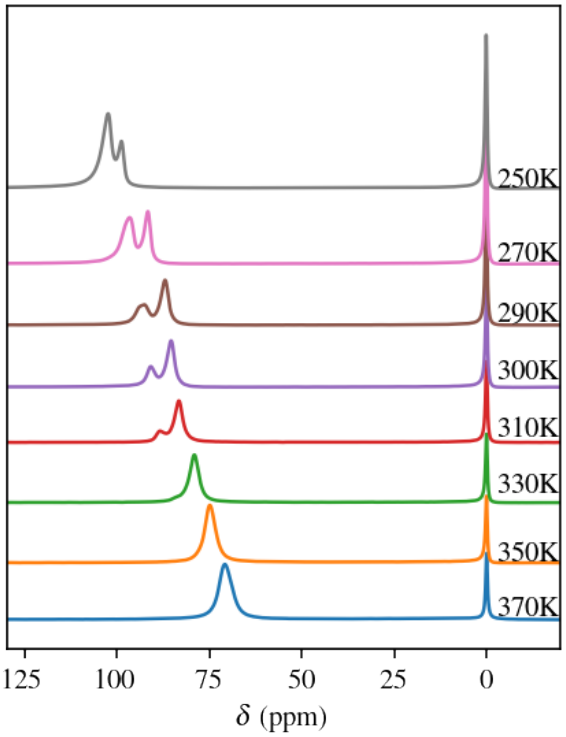

FIGURE 2.24: Variable temperature 1D ^{129}Xe NMR spectra for the sample after Potassium exchange (K-X).

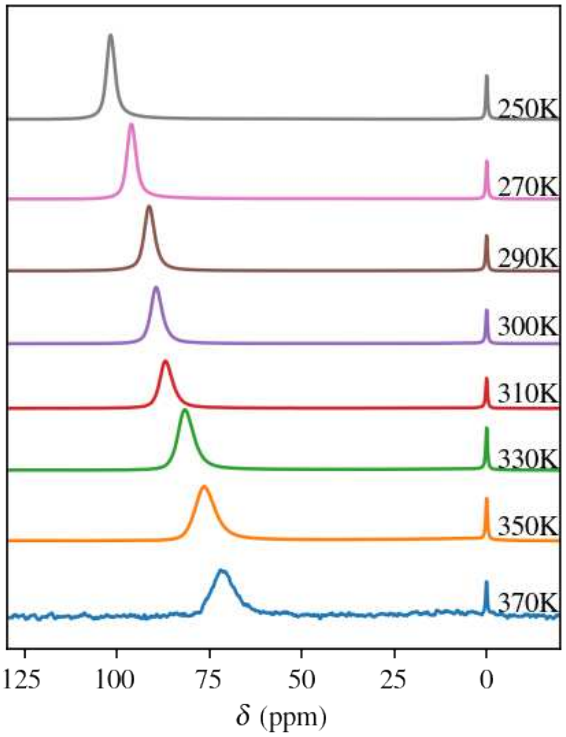

FIGURE 2.25: Variable temperature 1D ^{129}Xe NMR spectra for the sample after Rubidium exchange (Rb-X).

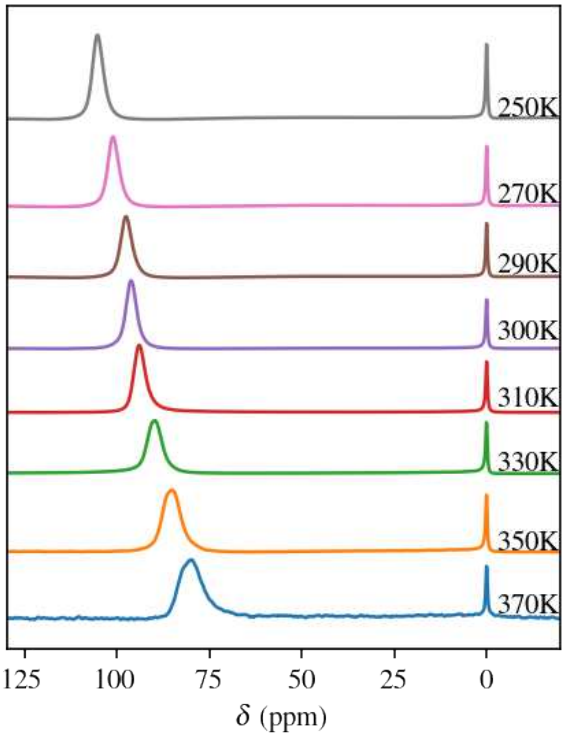

FIGURE 2.26: Variable temperature 1D ^{129}Xe NMR spectra for the sample after Cesium exchange (Cs-X).

no connectivity between sodalite cage and supercage are observed but only the signal on the diagonal for the supercage is present. With an increase of the mixing time (the same temperature and 100 ms) a cross peak out of the diagonal is visible. Similar results were obtained for K-X sample as shown in the figure 2.28

Thus for small cation like Li, Na and K, the same conclusion are that nanosized zeolites present open sodalite and a flexible structure. For Cs-X, and Rb-X EXSY experiment was not realized as only one peak is observed. Nevertheless, this only peak can by explain by the presence of non-negligible number of bigger cations which reduce the accessibility of xenon to the different kind of porosity.

2.3.3 Conclusions

In conclusion, results obtained from various characterization techniques helps to study the effect of cation substitution on nanosized FAU-X zeolites. The cation exchanged nanosized FAU-X zeolite system was studied for the first time in detail by conventional characterization and HP-^{129}Xe NMR. X-ray diffraction analysis showed the degree of crystallinity is well preserved. N_2-sorption and TGA show a presence of microporosity and excellent thermal stability. SEM analysis shows

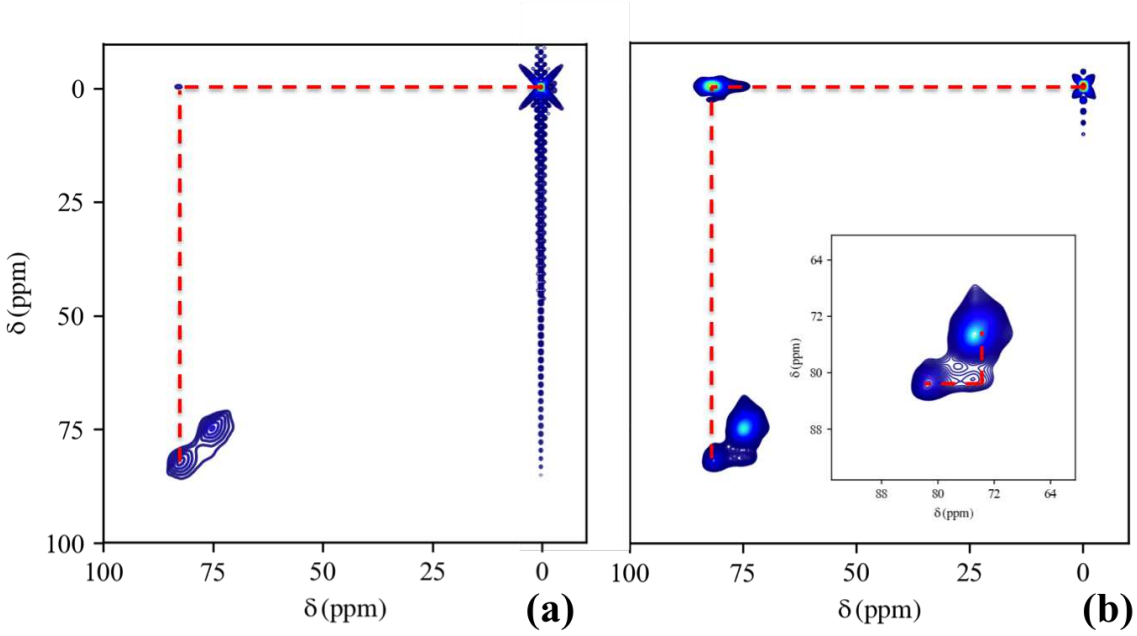

FIGURE 2.27: 2D EXSY Li-X at 330 K with (a) 10 ms and (b) 100 ms mixing time

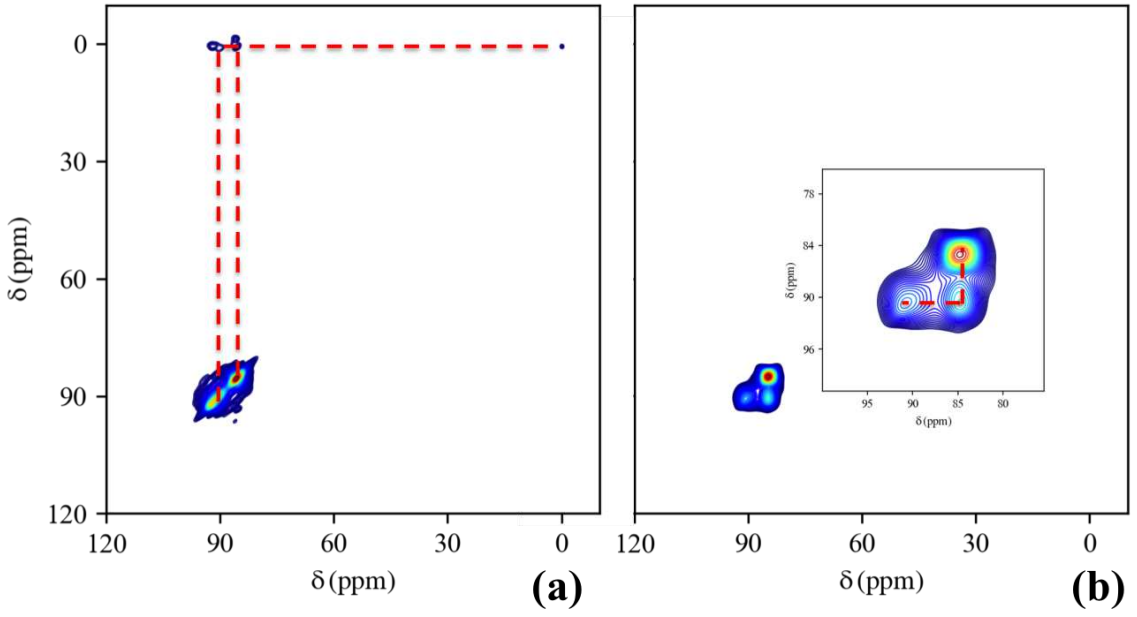

FIGURE 2.28: 2D EXSY K-X at 330 K with (a) 10 ms and (b) 100 ms mixing time

even after the cation exchange, all the samples have a narrow particle size distribution with small crystallites (10-15 nm).

Results obtained from ^{27}Al show the presence of the tetrahedral alumina and Si/Al ratio obtained by ^{29}Si MAS NMR is in a good agreement for all the samples. ^{23}Na MAS NMR on hydrated

and dehydrated samples confirmed the amount of sodium exchange for various cation used and the position of sodium therein.

HP-^{129}Xe NMR experiments conclude the xenon adsorption in both the cavities for Na-X, Li-X, and K-X samples. The presence of two cavities proves the sodalite cage is still accessible which is because of the flexibility of cages in nanosized FAUX zeolites and the size of the cation. In the same way, the presence of one peak in the sample exchanged with Rb^+ and Cs^+ help us to confirm the sodalite cage is blocked by the Rb and Cs cation. The comparison plots of all the exchanged samples at 300 K show the strength of xenon adsorption is Cs>Rb>K>Na∼Li.

Bibliography

[1] J. Weitkamp and L. Puppe. *Catalysis and zeolites: fundamentals and applications*. Springer Science and Business Media, 2013. 39

[2] J. Pérez-Ramírez, C. H. Christensen, K. Egeblad, C. H. Christensen, and J. C. Groen. Hierarchical zeolites: enhanced utilisation of microporous crystals in catalysis by advances in materials design. *Chemical Society Reviews*, 37(11):2530–2542, 2008. doi:10.1039/B809030K. 39

[3] J. C. Groen, J. A. Moulijn, and J. Pérez-Ramírez. Desilication: on the controlled generation of mesoporosity in mfi zeolites. *Journal of Materials Chemistry*, 16(22):2121–2131, 2006. doi:10.1039/B517510K. 39

[4] S. Veldurthi, C.-H. Shin, O.-S. Joo, and K.-D. Jung. Synthesis of mesoporous mgo single crystals without templates. *Microporous and Mesoporous Materials*, 152:31–36, 2012. doi:10.1016/j.micromeso.2011.11.044. 39

[5] D. Verboekend, M. Milina, S. Mitchell, and J. Pérez-Ramírez. Hierarchical zeolites by desilication: Occurrence and catalytic impact of recrystallization and restructuring. *Crystal Growth & Design*, 13(11):5025–5035, 2013. doi:10.1021/cg4010483. 40

[6] D. Verboekend and J. Pérez-Ramírez. Design of hierarchical zeolite catalysts by desilication. *Catalysis Science & Technology*, 1(6):879–890, 2011. doi:10.1039/C1CY00150G. 40

[7] Y. Yue, H. Liu, P. Yuan, C. Yu, and X. Bao. One-pot synthesis of hierarchical fezsm-5 zeolites from natural aluminosilicates for selective catalytic reduction of no by nh3. *Scientific reports*, 5, 2015. doi:10.1038/srep09270. 40

[8] P. Sazama, Z. Sobalik, J. Dedecek, I. Jakubec, V. Parvulescu, Z. Bastl, J. Rathousky, and H. Jirglova. Enhancement of activity and selectivity in acid-catalyzed reactions by dealuminated hierarchical zeolites. *Angewandte Chemie International Edition*, 52(7):2038–2041, 2013. doi:10.1002/anie.201206557. 40

[9] S. Huang, X. Liu, L. Yu, S. Miao, Z. Liu, S. Zhang, S. Xie, and L. Xu. Preparation of hierarchical mordenite zeolites by sequential steaming-acid leaching-alkaline treatment. *Microporous and Mesoporous Materials*, 191:18–26, 2014. doi:10.1016/j.micromeso.2014.02.039. 40

[10] S. Goel, S. I. Zones, and E. Iglesia. Synthesis of zeolites via interzeolite transformations without organic structure-directing agents. *Chemistry of Materials*, 27(6):2056–2066, 2015. doi:10.1021/cm504510f. 40

[11] Hartati, A. Akustia, I. Permana, D. Prasetyoko, M. Yasin, and S. W. Harun. Three-step crystallization in synthesis of zsm-5 without organic template. In *AIP Conference Proceedings*, volume 1718, page 060002, 2016. doi:10.1063/1.4943324.

[12] Y. Wei, T. E. Parmentier, K. P. de Jong, and J. Zečević. Tailoring and visualizing the pore architecture of hierarchical zeolites. *Chemical Society Reviews*, 44(20):7234–7261, 2015. doi:10.1039/C5CS00155B. 40

[13] H. Wang, B. A. Holmberg, and Y. Yan. Synthesis of template-free zeolite nanocrystals by using in situ thermoreversible polymer hydrogels. *Journal of the American Chemical Society*, 125(33):9928–9929, 2003. doi:10.1021/ja036071q. 40

[14] K. P. Dey, S. Ghosh, and M. K. Naskar. Organic template-free synthesis of zsm-5 zeolite particles using rice husk ash as silica source. *Ceramics International*, 39(2):2153–2157, 2013. doi:10.1016/j.ceramint.2012.07.083. 40

[15] S.-F. Wong, H. Awala, A. Vincente, R. Retoux, T. C. Ling, S. Mintova, R. R. Mukti, and E.-P. Ng. Kf zeolite nanocrystals synthesized from organic-template-free precursor mixture. *Microporous and Mesoporous Materials*, 249:105–110, 2017. doi:10.1016/j.micromeso.2017.04.053. 40

[16] H. Awala, J. P. Gilson, R. Retoux, P. Boullay, J. M. Goupil, V. Valtchev, and S. Mintova. Template-free nanosized faujasite-type zeolites. *nature materials*, 14:447–451, 2015. doi:10.1038/NMAT4173. 40, 41, 55

[17] S. Mintova, J. Grand, and V. Valtchev. Nanosized zeolites: Quo vadis? *Comptes Rendus Chimie*, 19(1):183–191, 2016. doi:10.1016/j.crci.2015.11.005. 40

[18] L. Pine, P. Maher, and W. Wachter. Prediction of cracking catalyst behavior by a zeolite unit cell size model. *Journal of Catalysis*, 85(2):466–476, 1984. doi:10.1016/0021-9517(84)90235-5. 41

[19] M. Feuerstein, M. Hunger, G. Engelhardt, and J. Amoureux. Characterisation of sodium cations in dehydrated zeolite nax by 23na nmr spectroscopy. *Solid state nuclear magnetic resonance*, 7(2):95–103, 1996. doi:10.1016/S0926-2040(96)01246-5. 44, 46

[20] S. Caldarelli, A. Buchholz, and M. Hunger. Investigation of sodium cations in dehydrated zeolites lsx, x, and y by 23na off-resonance riact triple-quantum and high-speed mas nmr spectroscopy. *Journal of the American Chemical Society*, 123(29):7118–7123, 2001. doi:10.1021/ja0102538. 44

[21] D. Massiot, F. Fayon, M. Capron, I. King, S. Le Calvé, B. Alonso, J.-O. Durand, B. Bujoli, Z. Gan, and G. Hoatson. Modelling one-and two-dimensional solid-state nmr spectra. *Magnetic Resonance in Chemistry*, 40(1):70–76, 2002. doi:10.1002/mrc.984. 44

[22] H. S. Sherry. The ion-exchange properties of zeolites. i. univalent ion exchange in synthetic faujasite. *The Journal of Physical Chemistry*, 70(4):1158–1168, 1966. doi:10.1021/j100876a031. 57

Chapter 3

Hyperpolarized ^{129}Xe NMR to Study the Recrystallization on Alkaline Treated Zeolites

3.1 Introduction

In this chapter we are discussing about the recrystallization on alkaline treated zeolites in presence of pore directing agents. So far in our previous works aiming at understanding the mesoporous formation during alkaline treatment in presence of organic additives, conventional bulk characterization techniques led to the conclusion that the dissolved zeolite does not undergo any kind of recrystallization.[1] In this chapter for the first time, we demonstrate using the data obtained from ^{1}H and ^{129}Xe NMR spectroscopy that such recrystallization does occur, which lead to the formation of a very thin coating of the mesopore walls. This demonstration is done on a beta (BEA) zeolite treated in presence of TPA^{+} in an alkaline solution. The formation of very tiny nanosized crystals or embryonic phases of silicalite-1 (MFI) zeolite is evidenced, as well as their homogeneous dispersion on the mesoporous surface of the beta zeolite.

Thereby, in the present study we have been using ^{1}H and ^{129}Xe NMR spectroscopy to bring new insight on the recrystallization occurring in the mesopore network in the case of zeolite beta.

Zeolite Beta

Zeolite Beta, a three-dimensional channel system high-silica zeolite with 12-membered ring apertures.[2,3] As shown in figure 3.1 the framework structure of this zeolite contains three intersecting channels. The structure consist of 12-member rings channels of a free aperture of 6.6×6.7 Å viewed along axis [1 0 0] and zigzag 12 membered ring channels of 5.6×5.6 Å viewed along axis [0 0 1].

Due to their large-pore system, large available micropore volume and good hydrothermal stability, Beta type zeolites have been used in several catalytic reactions: fluid catalytic cracking,[4] alkyl aromatics transformation,[5] isobutane alkylation with n-butene[6] etc. Dimitrova *et al.*[7] have studied the reaction over Beta zeolite with variable Si/Al ratio prepared by applying different methods. They found that the porous structure as well as acidity of catalysts varies depending on the preparation method employed. All catalysts were found to posses activity in methanol conversion to DME reaction. Beta zeolite structure has been reported to be an intergrowth of two or three polymorph types.[3]

3.1.1 Alkaline Treatment

100 ml of a mixed aqueous solution of sodium hydroxide (NaOH 0.2 M) and tetra-propyl ammonium bromide (TPABr 0.2 M) was stirred and then heated at a temperature of 338 K. 3.3 g of zeolite beta (BEA framework type[9] , Si/Al = 255) provided by Tosoh (product name: HSZ-980HOA) was added. The mixture was left to react for 30 min at 338 K, after which the solid material was separated via a Büchner filtration and washed with distilled water. The treated

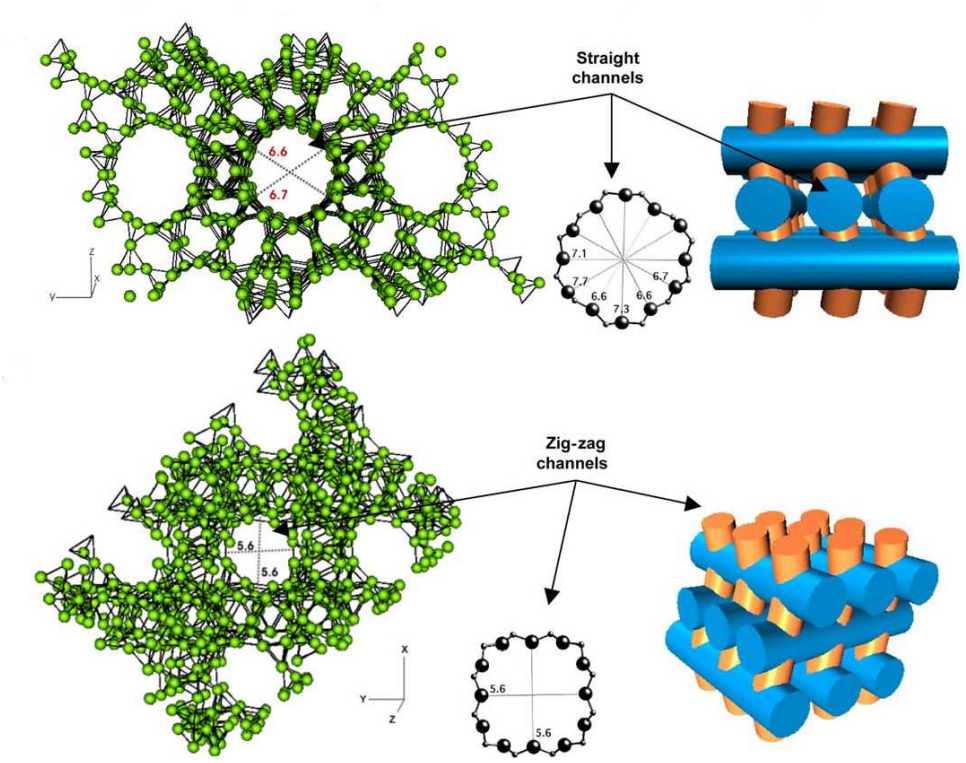

FIGURE 3.1: Stereographic drawing and perspective views of zeolite beta viewed along the [1 0 0] and [0 0 1] axes. The 12-membered ring free pore apertures of straight and zig-zag channels are also shown for a good visualization of its structure. In the stereographic drawings the spheres represent the oxygen atoms and the tetrahedrally coordinated si/Al atoms. Perspective views show the pore network of zeolite Beta containing straight and zigzag channels. The cylinders represent the channels of the zeolite Beta. Figure adapted from [8]

zeolite was eventually dried overnight at 373 K. The resulting sample will be referenced as AT-BEA in the following.

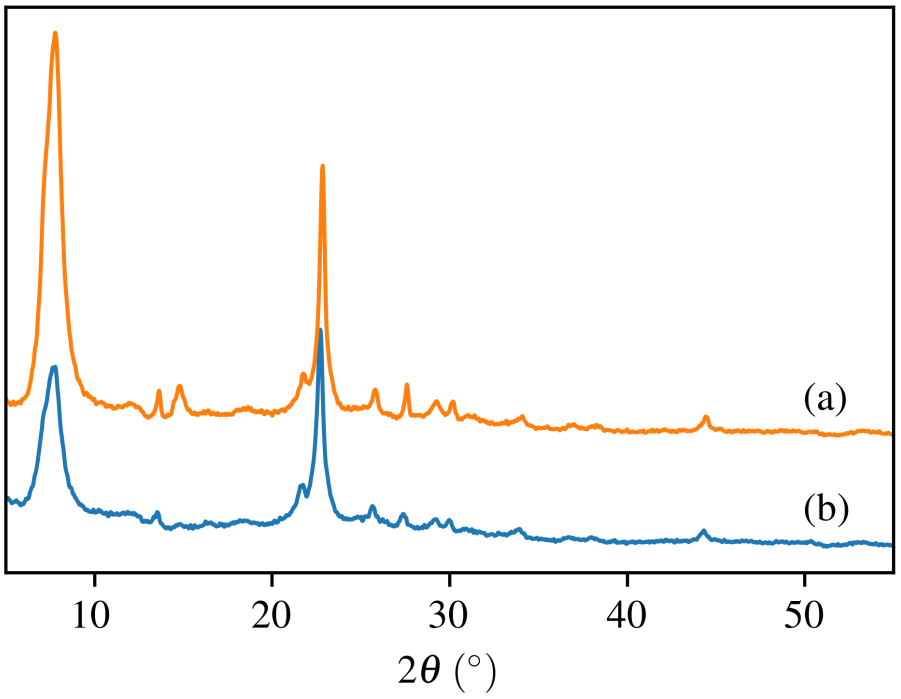

FIGURE 3.2: Powder XRD patterns of the beta zeolite taken before (a) and after (b) the alkaline treatments in presence of tetra-propyl ammonium ions

3.2 Characterization

The Classical characterization such as Powder X-ray diffraction, Thermal analysis, and Nitrogen sorption used. The experimental details are as discussed below,

3.2.1 X-ray diffraction

Powder XRD measurements were performed on a STOE Stadi P instrument in transmission mode using CuK$_\alpha$ radiation. The crystallinity ratio was determined from the intensity of the diffraction peak at approximately 22.8° 2θ.

3.2.2 Thermal analysis

The carbon content of the zeolite was determined by thermal gravimetric analysis (TGA). Combustion was performed by bringing the samples into a temperature-programed oven under an oxygen flow, using a TGA Q500 (TA Instruments) equipped with an automatic sampler. The sample was first heated to 333 K (3 K $\cdot$ min^{-}1) and was kept at that temperature for 30 min.

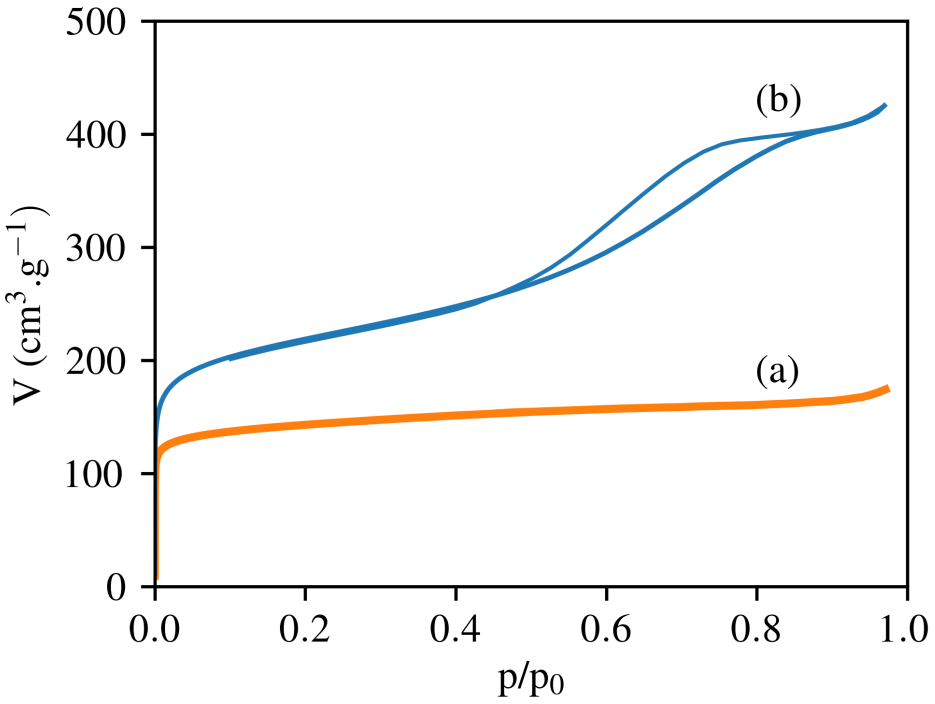

FIGURE 3.3: Nitrogen isotherms at 77 K taken before (a) and after (b) the alkaline treatments in presence of tetra-propyl ammonium ions. Nitrogen-sorption measurements were executed on a Micromeritics TriStar 3000 instrument. Prior to the sorption experiment, the samples were degassed overnight under a flow of N_2 with heating to 573 K (5 K.min$^-$1). The *t*-plot was used to distinguish between micro- and mesopores.

Afterwards, the sample was heated to 1073 K (3 K $\cdot$ min$^-$1) and was maintained at that temperature for 30 min. The amount of carbon was calculated from the mass loss taking into account weight loss due to water desorption below 423 K.

3.2.3 N_2 Sorption

Nitrogen-sorption measurements were executed at 77 K with a Micromeritics TriStar 3000 instrument, controlled by the corresponding software (version 6.03). Sorption was done on a sample previously calcined in static air during 5.5 h at 883 K, using a ramp rate 5 K.min$^-$1. Prior to the sorption experiment, the samples were degassed overnight under a flow of N_2 with heating to 573 K (5 K.min$^-$1). The *t*-plot was used to distinguish between micro- and mesopores (thickness range=0.35–0.50 nm). The mesopore size distribution was calculated using the Barret-Joyner-Halenda (BJH) method applied to the adsorption branch of the N_2 isotherms.

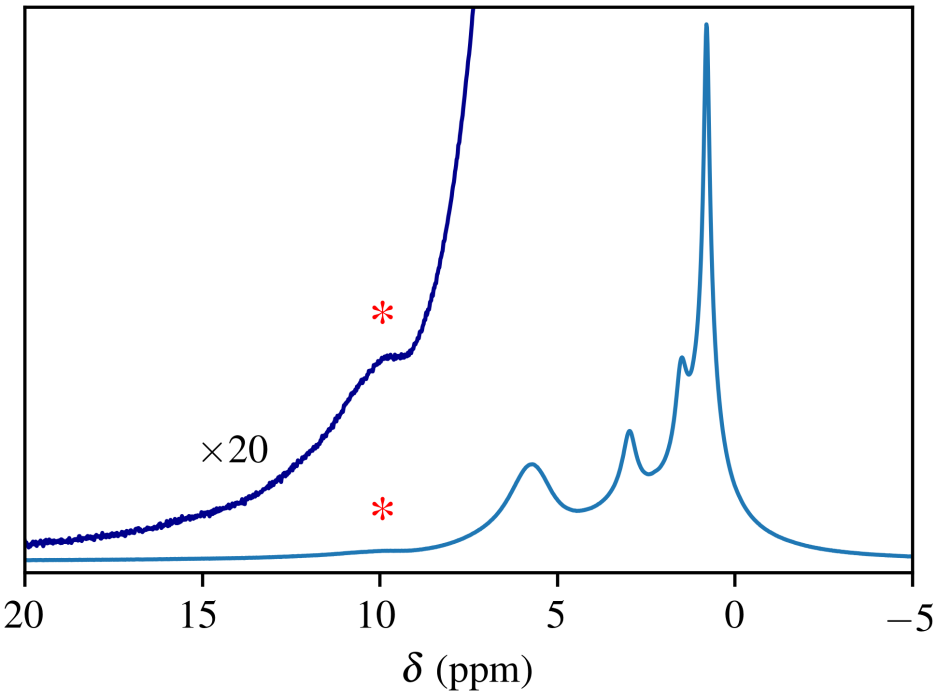

FIGURE 3.4: 1H NMR spectra of the AT-BEA zeolite, a BEA zeolite treated by the alkaline solution containing TPA^+. The top trace is the same spectrum with an intensity multiplication factor of 20. This proton spectrum exhibits typical resonances from the TPA molecules (≈0- 4 ppm), residual water (≈ 5.5 ppm) and from the silanols hydrogen-bounded to siloxy defects (≈ 10.2 ppm denoted with a red star)

3.2.4 ^{1}H NMR spectroscopy

Conventional ^{1}H magic-angle spinning (MAS) and two-dimensional ^{1}H double quantum (DQ) NMR spectra were acquired at 500 MHz on a Bruker Avance III-HD 500 (11.7 T), using 1.9-mm outer diameter zirconia rotors spun at 40 kHz, a radio frequency power of 100 kHz and a recycle delay of 2 s.

For the ^{1}H DQ NMR spectra, the recoupling of the double quantum coherence was performed following the well-known BaBa pulse sequence.[10] The time increment for the indirect t_1 dimension was equal to 50 μs (*e.g.*, twice the rotor spinning period). The recoupling time was set equal to four rotor cycles (100 μs).

The conventional ^{1}H MAS NMR spectrum of the treated zeolite AT-BEA is displayed in Figure 3.4. It shows a group of resonances between 0 and 4 ppm , which are assigned to the protons of the organic TPA^+ molecule. Residual water is observed between 5 and 6 ppm . Finally, a broad isolated resonance is present at 10 ppm . The latter peak is attributed to the hydrogen bond in a defect composed by a siloxy (SiO^-) and silanol (SiOH) in close vicinity.[11] This resonance has been observed in different zeolite frameworks such as assynthesized MFI, containing a tetra propyl ammonium as a organic structure directing agent (OSDA), where the negatively charged

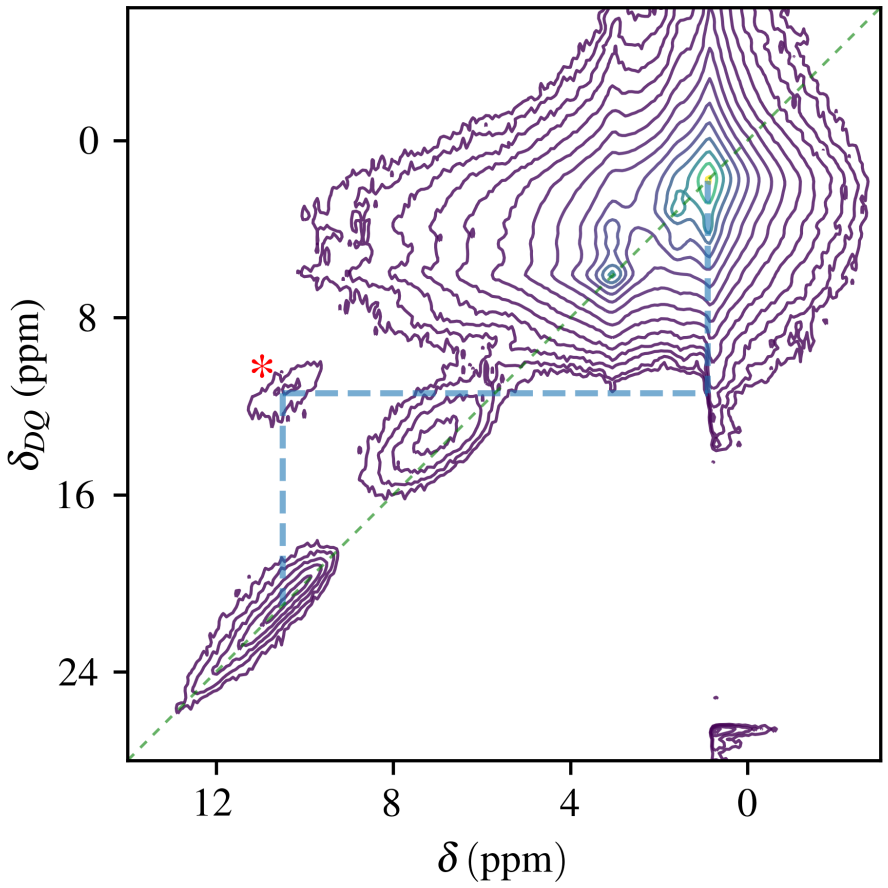

FIGURE 3.5: Two-dimensional ^{1}H double quantum (DQ) NMR spectra of the AT-BEA zeolite recorded using a BABA pulse sequence. The light blue dashed lines indicate the correlation of the siloxy/silanols groups (denoted with a red star) with the TPA^{+} methyl protons. As expected the water peak at 5.5 ppm is almost not seen on the diagonal owing to the high mobility which prevents double-quantum recoupling between the water protons in the current experimental conditions. However, it is observed a feature that could not be seen on the 1D spectrum, *e.g.*, a significant correlation peak corresponding to a resonance around 7 ppm which may be due to silanols created during the alkaline treatment on and in interaction with some residual water molecules.

siloxy defects counterbalance the positive charge of the OSDA.[11–13] Consequently, the existence of a 10 ppm resonance in the alkaline treated BEA zeolite is a strong indication that it is due to the presence of TPA^{+} ions in the sample.

In order to better understand the origin of this resonance at 10 ppm in AT-BEA zeolite, a two-dimensional (2D) double quantum (DQ) ^{1}H NMR experiment has been performed. This NMR experiment allows getting information on the internuclear distances from the measurements of the through-space dipole-dipole couplings. The recoupling of the DQ coherence under magic-angle spinning conditions can be achieved following the back-to-back (BABA) pulse sequence.

As displayed on Figure 3.5, diagonal single-quantum/double-quantum correlation peaks appear for all resonances, which show that all protons have similar neighbors. This is obviously expected

for the internal protons of the TPA molecule; however, the observation that this also occurs for the resonance at 10 ppm , reveals that the silanols hydrogen-bounded to siloxy defects are in close vicinity. In addition, the 10 ppm resonance is clearly correlated to the methyl protons of the TPA^+ molecule. This is very similar to what we have recently observed for silicalite-1 (a pure silicious MFI zeolite[9]), and confirms that the existence of the negatively charged siloxy defects is likely due to the presence of TPA^+ organic ions.[13]

One reason for this observation could be that the silica dissolved from the parent BEA zeolite during the alkaline treatment is subjected to recrystallization in presence of TPA^+ molecules. All the basic elements for nanozeolite crystallization are present at a convenient temperature, *i.e.*, a silica source from the dissolved BEA zeolite (SiO_2), a mineralizing agent (NaOH) and a structure-directing agent (TPA^+). As the tetra-propyl ammonium is generally employed for the crystallization of silicalite-1, we can suggest that some MFI zeolite crystals are produced during such recrystallization. However, the latter is not observed by X-ray diffraction, which may indicate that only a very small amount of such phase is present and/or that the size of the zeolite particles is very small (embryonic phases[14] or nanosized crystals).

3.2.5 HP ^{129}Xe NMR

With all above mentioned characterization method used we have proved and by considering there limitations itself A valuable technique to prove such a hypothesis is ^{129}Xe NMR spectroscopy

A valuable technique to prove such a hypothesis is ^{129}Xe NMR spectroscopy. Indeed, it has been shown that the xenon molecule has a chemical shift very sensitive to the local environment and in particular to the size of the pore in which it is adsorbed.[15,16] Hence, referring to existing literature, one can easily identify the zeolite phases based on the chemical shifts of the xenon molecular probe.[17,18] However, as the amount and size of the zeolitic phases to determine are likely very small, it is important to detect them using sensitivity enhancement techniques, as the ^{129}Xe hyper-polarization by laser pumping (HP ^{129}Xe NMR).[19]

The NMR spectra of HP ^{129}Xe adsorbed on the alkaline treated BEA zeolite recorded at different temperatures are shown in figure 3.7 and in figure 3.6 for the lowest temperature of 235 K. A sharp resonance is always observed upfield which corresponds to the free xenon gas. This line is taken as the chemical shift reference and is set to 0 ppm . At all temperatures, the xenon spectra exhibit a resonance in the 70- 90 ppm range corresponding to the molecules adsorbed in the BEA zeolite channels.[20] Its chemical shift increases as temperature is decreasing (Figure SI-3). Below 270 K, a low-intensity shoulder starts to grow on its left side, and finally, at the lower temperature (235 K) two well-resolved peaks can be observed (Figure 3.6). The chemical shift of this resonance seems characteristic of the silicalite-1 (MFI) zeolite structure.[18,21,22]

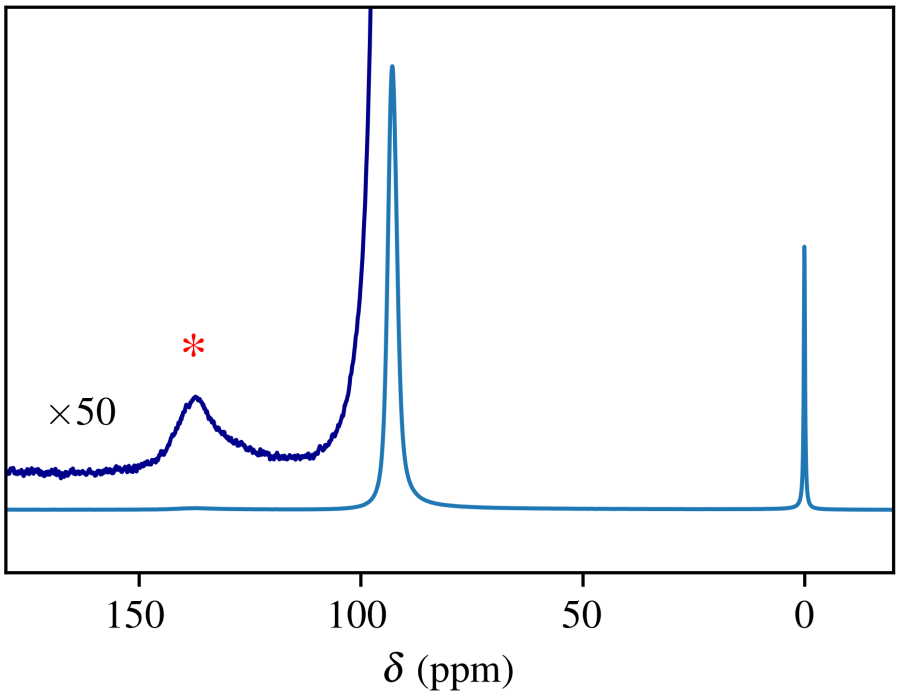

FIGURE 3.6: NMR spectrum of HP ^{129}Xe adsorbed on the treated AT-BEA zeolite recorded at 235 K. An expansion of the spectrum is made in the 180- 100 ppm region to show the small resonance (denoted with the red star) for the xenon adsorbed in the MFI phase.

As reported on Figure 3.8, the evolution of the chemical shift of this resonance is very close to that of a pure silicalite-1 recorded in similar conditions, in line with the aforementioned attribution based on the ^{1}H NMR spectra. The very low intensity of this resonance reflects a very low concentration of the MFI phase with respect to the BEA phase. Clearly, both ^{1}H and ^{129}Xe NMR results suggest the formation of MFI phase during the alkaline treatment of the BEA zeolite in the presence of TPA^{+}. However, these results do not provide information about the location of both phases.

For that purpose, a 2D exchange spectroscopy experiment (EXSY) can be applied to probe the connection between both MFI and BEA phases. In such 2D experiment, any non-diagonal peak (cross-peak) is a proof that ^{129}Xe molecules are exhibiting a slow chemical exchange between two different positions. Only close enough positions are concerned by these cross peaks due to the short mixing times used in the experiment (500 ms) and T_1 relaxation. Figure 3.9 shows cross-peaks at the top of the 2D spectrum, indicating that free xenon has a direct access into both BEA and MFI channels. As well as, a direct connection between MFI and BEA is proved. Moreover, the absence of a diagonal peak corresponding to xenon adsorbed in MFI channels, shows that likely xenon molecules enter and exit MFI phase very rapidly, which suggest that the MFI phase is in the beginning phase of crystallization and distributed in a such way that no direct connection exists between them.

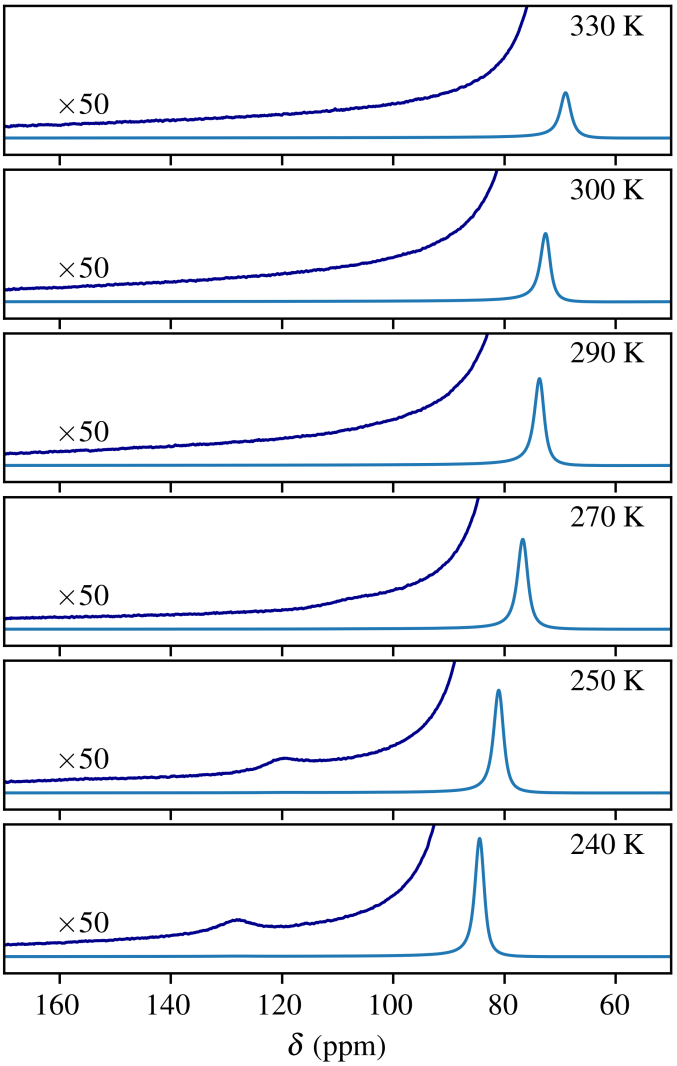

FIGURE 3.7: NMR spectra of HP ^{129}Xe adsorbed on alkaline treated BEA zeolite recorded at variable temperature. The main resonance corresponds to xenon adsorbed in the BEA micropores. On the expansion of the spectra (factor ×50), a small peak on the left (downfield) of the main resonance appears at temperature below 270 K and is attributed to the presence of MFI in the sample. The resonances are shifted with temperature due to a different equilibrium between the surface adsorbed and the gas phase xenon that are in a regime of fast exchange. Note that the narrow line due to the gas phase is at 0 ppm (reference of chemical shift) and thus does not appear on these spectra. It can be shown on Figure 4 in the main text.

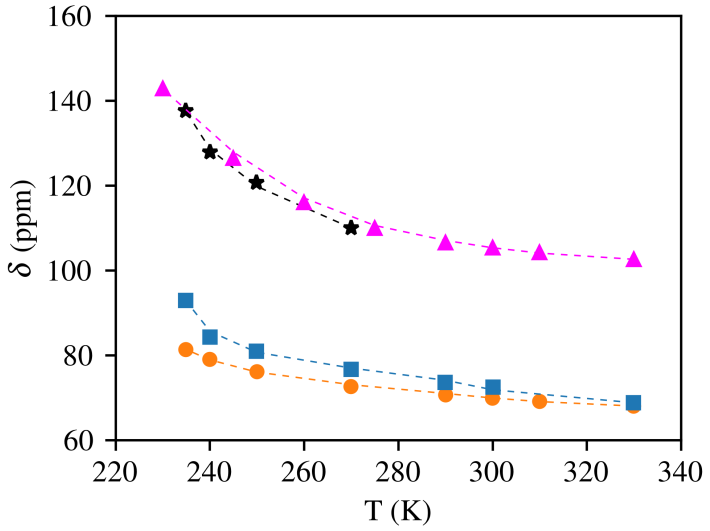

FIGURE 3.8: Xenon chemical shift vs. the temperature of adsorption for the parent BEA zeolites (circles), the main peak (squares) and the smaller peak chemical shift (stars) for alkaline treated sample and finally the chemical shift of a pure silicalite-1 (triangles).

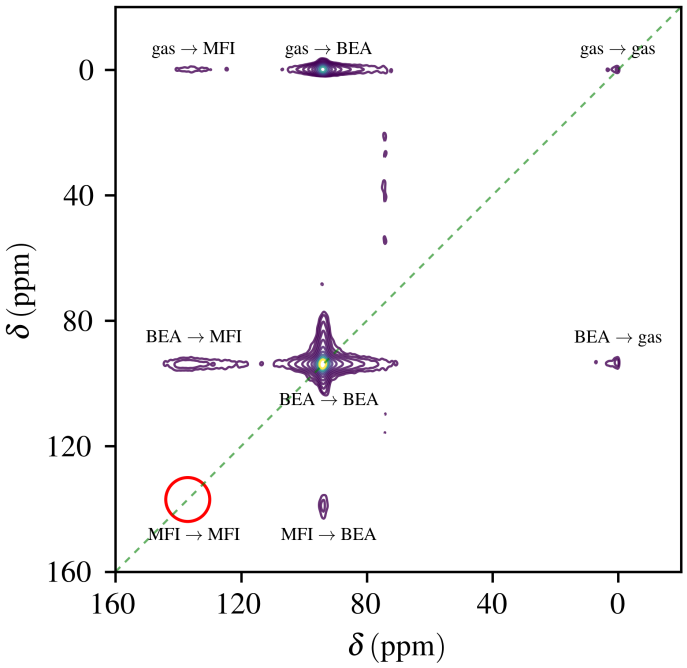

FIGURE 3.9: Exchange NMR (EXSY) spectrum of HP ^{129}Xe adsorbed on AT-BEA zeolite at T=235 K and a mixing period of τ_m= 500 ms . The existence of cross peaks reflects the traveling of the xenon molecules between the free gas phase and the micropores of both the MFI and BEA phases. The red circle indicates the expected position of the diagonal peak that should be present if the xenon was exchanging inside the microporous channels of MFI.

3.3 Result and Discussion

Using ^{1}H and ^{129}Xe NMR spectroscopy, the formation of MFI has been evidenced. ^{1}H NMR shows that MFI is containing TPA^{+} ions in interaction with charge-compensating framework defects, *i.e.*, siloxy groups hydrogen-bonded to silanol groups ($SiO^{-}\cdots HOSi$).[13] As above-mentioned, the media, in which the BEA undergoes alkaline treatment, is very favorable for MFI crystallization. Indeed, the highly silica parent BEA zeolite is partly dissolved giving a source of silica, the media is alkaline and the presence of TPA^{+} plays the role of the structure-directing agents. In this condition, it is thus not surprising that nanocrystals or embryonic phases of MFI can be formed.

HP ^{129}Xe NMR proves unambiguously the presence of tiny MFI particles, which are likely very well dispersed in the solid. ^{129}Xe EXSY experiments additionally shows that the homogeneous dispersion of the MFI phase is close to the opening of the microporous system of the BEA crystal. Indeed, the significant exchange of xenon is observed between BEA and MFI, while no exchange can be detected between MFI phases itself. Explanation is that the MFI particles are very small and homogeneous dispersed on the whole surface of the mesopores created during the alkaline treatment.

It is worth noting that the amount of TPA^{+} determined by TGA (17.5 wt.%) can be converted to a number of unit cells of MFI per grams of AT-BEA zeolite, as four TPA^{+} molecules occupy one unit cell. This calculation gives 1.4 10^{20} u.c./g. Assuming a mono-layer of MFI at the surface of the mesopores, taking the larger surface of the MFI unit cell and assuming a thickness of one unit cell, we obtain a surface of about 560 $m^2.g^{-1}$. Of course, this is a limiting upper value, which assumes an extreme dispersion of the MFI crystals. However it is not very different from the surface of the mesopores determined by nitrogen sorption (350 $m^2.g^{-1}$). This thereby confirms that our interpretation is correct and that the coverage of the mesoporous surface can be complete, with a thickness of the MFI layer between one or two unit cells.

Finally, the formation of MFI when using TPA^{+} as pore-directing agent (PDA), explains nicely why it was found mandatory to use such PDA to prevent an extensive amorphization of highly silicic zeolites during desilication in alkaline media and to create homogeneous size of mesopores.[23]

Indeed, when alkyl-ammonium cations such as TPA^{+} are present during the treatment, they likely prevent a random amorphization of the parent zeolite by forming a 'hydrophobic' assembly of molecules. They interact with the surface producing MFI small cages and prevent hydroxyl anions coming from NaOH to dissolve the material.

3.3.1 Conclusion

In conclusion, the MFI appears as a kind of coating of the mesoporous surface. We anticipate that changing the PDA molecules used during the alkaline treatment could be a way to control the nature of the mesopore coating. This could be profitable for applications, as the interfacial coexistence of both phases can generate interesting surface properties and thus could be beneficial in some catalytic and/or adsorption process.

Bibliography

[1] D. Verboekend, M. Milina, S. Mitchell, and J. Pérez-Ramírez. Hierarchical zeolites by desilication: Occurrence and catalytic impact of recrystallization and restructuring. *Crystal Growth & Design*, 13(11):5025–5035, 2013. doi:10.1021/cg4010483. 69

[2] C. Baerlocher, L. B. McCusker, and D. H. Olson. *Atlas of Zeolite Framework Types*. Elsevier Science B.V., sixth edition edition, 2007. doi:10.1016/B978-044453064-6/50223-1. 69

[3] J. Higgins, R. B. LaPierre, J. Schlenker, A. Rohrman, J. Wood, G. Kerr, and W. Rohrbaugh. The framework topology of zeolite beta. *Zeolites*, 8(6):446–452, 1988. doi:10.1016/S0144-2449(88)80219-7. 69

[4] A. Corma, V. Fornes, F. Melo, and J. Perez-Pariente. Zeolite beta: Structure, activity, and selectivity for catalytic cracking. ACS Publications, 1988. 69

[5] A. B. Halgeri and J. Das. Novel catalytic aspects of beta zeolite for alkyl aromatics transformation. *Applied Catalysis A: General*, 181(2):347–354, 1999. doi:10.1016/S0926-860X(98)00395-0. 69

[6] G. S. Nivarthy, K. Seshan, and J. A. Lercher. The influence of acidity on zeolite h-bea catalyzed isobutane/n-butene alkylation1. *Microporous and mesoporous materials*, 22(1-3): 379–388, 1998. doi:10.1016/S1387-1811(98)00092-4. 69

[7] R. Dimitrova, G. Gunduz, L. Dimitrov, T. Tsoncheva, S. Yialmaz, and E. A. Urquieta-González. Acidic sites in beta zeolites in dependence of the preparation methods. *Journal of Molecular Catalysis A: Chemical*, 214(2):265–268, 2004. doi:10.1016/j.molcata.2003.12.019. 69

[8] P. S. Bárcia, J. A. Silva, and A. E. Rodrigues. Adsorption equilibrium and kinetics of branched hexane isomers in pellets of beta zeolite. *Microporous and mesoporous materials*, 79(1):145–163, 2005. doi:10.1016/j.micromeso.2004.10.037. 70

[9] C. Baerlocher and L. McCusker. Database of zeolite structures. `http://europe.iza-structure.org/IZA-SC/ft.php`. Last accessed: 2017-03-01. 69, 75

[10] M. Feike, D. Demco, R. Graf, J. Gottwald, S. Hafner, and H. Spiess. Broadband Multiple-Quantum NMR Spectroscopy. *J. Magn. Reson.*, 122(2):214–221, 1996. doi:10.1006/jmra.1996.0197. URL http://linkinghub.elsevier.com/retrieve/pii/S1064185896901977. 73

[11] H. Koller, R. F. Lobo, S. L. Burkett, and M. E. Davis. SiO-... HOSi Hydrogen Bonds in As-Synthesized High-Silica Zeolites. *J. Phys. Chem.*, 99(33):12588–12596, 1995. doi:10.1021/j100033a036. 73, 74

[12] H. Koller and M. Weiss. Solid state nmr of porous materials. *Top. Curr. Chem.*, 306: 189–227, 2011.

[13] E. Dib, J. Grand, S. Mintova, and C. Fernandez. Structure-directing agent governs the location of silanol defects in zeolites. *Chemistry of Materials*, 27(22):7577–7579, 2015. doi:10.1021/acs.chemmater.5b03668. 74, 75, 79

[14] K.-G. Haw, J.-M. Goupil, J.-P. Gilson, N. Nesterenko, D. Minoux, J.-P. Dath, and V. Valtchev. Embryonic ZSM-5 zeolites: Zeolitic materials with superior catalytic activity in 1,3,5-triisopropylbenzene dealkylation. *New J. Chem.*, 40(5):4307–4313, 2016. doi:10.1039/C5NJ03310A. URL http://xlink.rsc.org/?DOI=C5NJ03310A. 75

[15] J. Fraissard and T. Ito. 129xe n.m.r. study of adsorbed xenon: A new method for studying zeolites and metal-zeolites. *Zeolites*, 8(5):350 – 361, 1988. doi:10.1016/S0144-2449(88)80171-4. 75

[16] J. Fraissard. Chapter 1. Xenon as a Probe Atom: Introduction, Characteristics, Investigation of Microporous Solids. In T. Meersmann and E. Brunner, editors, *New Developments in NMR*, pages 1–15. Royal Society of Chemistry, Cambridge, 2015. 75

[17] S. Habib, F. Launay, M.-A. Springuel-Huet, F. Guenneau, V. Semmer-Herlédan, N. N. Tusar, V. Kaucicb, and A. Gédéon. Monitoring the crystallization process of a zeolite structure on sba-15 mesopore walls. *New J. Chem*, 30:1163–1170, 2006. doi:10.1039/B603843C. 75

[18] S. Habib, F. Launay, H. E. Zakhem, M. Mazaj, F. Guenneau, P. Beaunier, D. Brouri, N. N. Tusar, V. Kaucic, and A. Gédéon. ZSM-5/SBA-15 microporous/mesoporous composites prepared by a microwave-assisted zeolitisation of al-SBA-15 mesoporous solids. *Materials Research Bulletin*, 48(3):1288–1295, 2013. doi:10.1016/j.materresbull.2012.12.030. 75

[19] D. Raftery, H. Long, T. Meersmann, P. J. Grandinetti, L. Reven, and A. Pines. High-field nmr of adsorbed xenon polarized by laser pumping. *Physical Review Letters*, 66(5):584–587, 1991. doi:10.1103/PhysRevLett.66.584. 75

[20] S. C. Laha, A. Sakthivel, K. Komura, S.-J. Huang, P.-H. Wu, S.-B. Liu, Y. Sasaki, M. Kobayashi, and Y. Sugi. Highly stable mesoporous aluminosilicates with a dual pore system: Simultaneous formation of mesophase with zeolitic building units. *Chemistry letters*, 38(6):548–549, 2009. doi:10.1246/cl.2009.548. 75

[21] V. V. Terskikh, I. L. Moudrakovski, H. Du, C. I. Ratcliffe, and J. A. Ripmeester. The 129xe chemical shift tensor in a silicalite single crystal from hyperpolarized 129xe NMR spectroscopy. *J. Am. Chem. Soc.*, 123(42):10399–10400, 2001. doi:10.1021/ja0114106. 75

[22] Y. Liu, W. Zhang, Z. Liu, S. Xu, Y. Wang, Z. Xie, X. Han, and X. Bao. Direct observation of the mesopores in zsm-5 zeolites with hierarchical porous structures by laser-hyperpolarized 129xe nmr. *The Journal of Physical Chemistry C*, 112(39):15375–15381, 2008. doi:10.1021/jp802813x. 75

[23] D. Verboekend, G. Vilé, and J. Pérez-Ramírez. Mesopore formation in usy and beta zeolites by base leaching: Selection criteria and optimization of pore-directing agents. *Crystal Growth & Design*, 12(6):3123–3132, 2012. doi:10.1021/cg3003228. 79

Appendix A

Characterization techniques

This section describes the characterization techniques that have been employed for the characterization of zeolites. These includes the methods used to determine the crystallinity (XRD), textural properties (N_2 sorption methods), thermal decomposition (TGA), zeolite structure (NMR). The instrumental details and characterization procedure is discussed below,

X-Ray Diffraction

X-ray diffraction on zeolites is a convenient tool to identify a zeolite structure and ensure phase purity. Most often, the zeolite is analyzed in the form of a powder and the obtained powder X-ray diffractogram used as a "fingerprint" unique to the particular crystalline phase. The well-known powder diffractograms are obtained as a slice of the ring plotted as the distance from the center and out (2θ) versus the intensity. The position of the diffraction gives information regarding size and shape of the unit cell while the diffraction intensity is derived from the specific atom and its location within the unit cell.

The X-ray diffraction (XRD) patterns of the solid phases were collected by a PANalytical X'Pert Pro MPD diffractometer using Cu-Kα monochromatic radiation ($\lambda = 1.5418$Å) This instrument is equipped with a copper tube with a 45 kV voltage and 40 mA current. A graphite receiving monochromator, a scintillation counter equipped with pulse height discriminator and sample holder complete the XRD diffractometer. The samples were scanned in the range of Bragg angles 2θ = 4-50° with a step size 0.02°.

N_2 Sorptions

A key parameter for any catalyst is the surface area accessible for reactants. A conventional way of measuring this is by low temperature (77 K) adsorption of N_2. This technique is based on stepwise adsorption of N_2 initially building a submono layer as the N_2 pressure above the sample increases multilayer formation begins. Since the desorption energy of the nitrogen desorbing from

the surface vs. nitrogen desorbing from a multilayer is different it is possible to derive at which point a monolayer is reached.

The porosity and specific surface area of the samples were characterized by Nitrogen adsorption measurements with a Micromeritics ASAP 2010 instrument. For the purpose of removing the possible physisorbed moisture and organics each sample was initially degassed at 275°C under vacuum overnight prior to the measurement. The external surface area and micropore volume were estimated by alpha-plot method using silica-1000 ($22.1 m^2/g$ assumed) as a reference. The micropore and mesopore size distributions of solids were estimated by the Nonlocal Density Functional Theory (NLDFT) and Barret-Joyner-Halenda (BJH) on the desorption branch methods, respectively.

Thermogravimetric analysis (TGA)

Thermogravimetric analysis is the method of thermal analysis in which mass of the sample is measured over time as the temperature changes. This measurements provides information bout physical phenomena, such as phase transition, absorption and desorption as well as the chemical phenomena such as chemisorptions, thermal decomposition and solid gas reactions (*e.g.*, oxidation or reduction). The thermogravimetric data collected from a thermal reaction is compiled into a plot of temperature versus mass or percentage of initial mass this plot is referred to as a TGA curve.

Thermal analysis of solid phases was measured by Thermogravimetric analysis (TGA) using SETSYS instrument (SETARAM) analyzer. Heating rate of 5 $°C.min^{-1}$ under 40 $ml.min^{-1}$ flow of air used for analysis.

FE-SEM

The crystal size and homogeneity of the samples were determined by field emission scanning electron microscope (FE-SEM). using a MIRA LMH (TESCAN) equipped with a field emission gun using an accelerating voltage of 30.0 kV.

^{29}Si, ^{23}Na, and ^{27}Al MAS NMR

^{29}Si, ^{23}Na, and ^{27}Al MAS NMR were performed in Bruker Avance III 500 MHz spectrometer using 4 mm o-ring zirconia rotors. For ^{29}Si MAS NMR, 2 μs pulse (30°) were performed with a recycle delay of 20s. For ^{23}Na and ^{27}Al MAS NMR, selective pulse of 1.5 and 1.7 μs, respectively were used and 1s of recycling delay. Sample was dehydrated at 275°C under vacuum for ^{23}Na in order to decrease the mobility of sodium and localized it in the framework. TMS, NaCl 0.1M and $Al(NO_3)_3$ 0.1M were used as reference for ^{29}Si, ^{23}Na and ^{27}Al, respectively.

The framework n_{Si}/n_{Al} ratio of zeolite samples studied in this thesis is calculated directly from the ^{29}Si MAS NMR intensities using the formula:

$$n_{Si}/n_{Al} = \frac{\sum_{n=0}^{4} I_{Si}(nAl)}{\sum_{n=0}^{4} 0.25 \cdot n \cdot I_{Si}(nAl)} \tag{A.1}$$

where, the terms $I_{Si}(nAl)$ are the intensities of the Si(nAl) lines.

HP-^{129}Xe NMR

Hyperpolarized ^{129}Xe NMR experiments were performed at 110.6 MHz Bruker Avance III-HD 400 (9.4 T) spectrometer, 128 scans were summed to record each spectrum using single 90° excitation pulse with a pulse length of 12.5 μs and a recycle delay of 1 s. The hyper-polarized xenon gas was obtained using a home-built xenon polarizer based on the spin-exchange optical pumping (SEOP) technique, capable to deliver a continuous flow of HP- ^{129}Xe directly to the sample inside the NMR spectrometer.

Prior to each experiment all the samples were compressed into pellets at a pressure 100 MPa, then crashed and sieved into small particles of 200-500 μm diameters. Approximately 0.5 g sample was introduced into a home-designed 10 mm O.D. NMR tube and dehydrated under high-vacuum at 548 K overnight. ^{129}Xe NMR spectra were acquired under continuous recirculating flow at $50\,\mathrm{mL} \cdot \mathrm{min}^{-1}$ of a gas mixture at a pressure of 0.15 MPa and containing 90 % He, 6 % N_2, and 4% of natural abundance xenon. For all variable temperature (VT) measurements and after each temperature change performed at a speed of $5\,\mathrm{K} \cdot \mathrm{min}^{-1}$, a waiting delay of about 20 min was generally necessary to ensure a homogeneous temperature all over the sample, and this stability was checked by directly monitoring the xenon chemical shifts.

2D-EXSY HP ^{129}Xe NMR

2D Exchange spectroscopy (EXSY) HP-^{129}Xe NMR spectra were recorded using a basic three pulses ($\pi/2 - t_1 - \pi/2 - \tau_m - \pi/2 -$ observe) sequence with a minimum of sixteen different phase combinations in order to select a $0 \mapsto 1 \mapsto 0 \mapsto -1$ coherence transfer pathway. The time increment in the indirect t_1 dimension was 0.5 s. To observe exchange cross peaks with a significant intensity, without losing the signal of xenon due to relaxation, the mixing period (τ_m) was varied from 5 ms to 200 ms .

To find the amount of Na % remained in a sample

i) First to find weight of dry sample,

$$\frac{\texttt{loss in a mass (TGA)}}{100} \times \texttt{weight of a sample} = \texttt{A}$$

$\therefore$ weight of the sample - A = weight of the dry sample (B)

Now, normalize the weight of the dry sample with standard sample (here Na-X is used as a standard sample).

$$\therefore \frac{\texttt{dry sample weight}}{\texttt{standard sample weight}} = \texttt{normalization factor(C)}$$

ii) Amount of Na % in dry sample,

$$\frac{\texttt{Na \% integration by NMR}}{\texttt{Normalization factor(C)}} = \texttt{Na \% remain in a sample}$$

List of Figures

List of Schemes

List of Tables

Abstract

Study of novel porous materials by ^{129}Xe NMR

The zeolites are 'molecular sieves' known for their numerous applications in adsorption, ion exchange, and catalysis. In this thesis, we focused on the study of some questions related to zeolite synthesis and post-synthesis, which are not yet resolved by other techniques. NMR was the primary tool in this work, as it gives access to local structural information on nanocrystals even when diffraction techniques found their limits. NMR can also be used to study porosity using probe molecules adsorption, and in particular, xenon is known as a good molecule for this purpose. Indeed, the isotope ^{129}Xe can be hyperpolarized to increase the detection sensitivity, and interestingly it presents a wide chemical shift range depending on its confinement and thus the porosity of studied material. Two studies are reported in this manuscript: (i) In the first study, the initial steps during the crystallization of nano-faujasite (FAU) type materials were investigated using classical NMR (mainly by ^{29}Si and ^{23}Na MAS NMR) and advanced NMR (^{129}Xe HP NMR). It was shown that crystallization starts at much earlier synthesis stages than those observed by other classical techniques (XRD, SEM, N_2 adsorption...). The first SBU seems to be the hexagonal prisms, prior to the sodalite cages, which rapidly form confined environment and then supercages. Moreover, it has been proved by ^{129}Xe HP NMR and 2D EXSY that nano-faujasite zeolite presents opened sodalite cages and a more flexible structure than in micro-faujasite zeolite. (ii) The second study is an investigation on the recrystallization phenomena occurring during hierarchization process of zeolite and which could explain the homogenous distribution of the mesopore sizes. As a remarkable result, it has been shown in this work that during the hierarchization of beta zeolite with TPAOH, the recrystallization lead to the formation of tiny MFI particles, formed at the surface of the mesopores (^{1}H MAS NMR, ^{129}Xe HP NMR and 2D EXSY).

Key words: Zeolite, Porosity, Structure, Solid-state NMR, ^{129}Xe NMR, hyperpolarization, 2D EXSY.

Résumé

Etude de nouveaux matériaux poreux par Résonance Magnétique Nucléaire du ^{129}Xe

Les zéolites sont des «tamis moléculaires» connus pour leurs nombreuses applications en adsorption, échange d'ions et catalyse. Dans cette thèse, nous nous sommes concentrés sur l'étude de quelques questions liées à la synthèse et à la post-synthèse de la zéolithe, qui ne sont pas encore résolues par d'autres techniques. La RMN a été l'outil principal dans ce travail, donnant accès à des informations structurales locales sur les nanocristaux même lorsque les techniques de diffraction trouvent leurs limites. Elle peut également être utilisée pour étudier la porosité en utilisant l'adsorption de molécules sondes, et en particulier, le xénon est connu comme une bonne molécule pour cet objectif. En effet, l'isotope ^{129}Xe peut être hyperpolarisé pour augmenter la sensibilité de détection, et il présente une large plage de déplacement chimique en fonction du confinement et donc de la porosité du matériau étudié. (I) Dans la première étude, les étapes initiales de la cristallisation de nano-faujasite (FAU) ont été étudiées en utilisant la RMN classique (principalement par ^{29}Si and ^{23}Na MAS RMN) et la RMN avancée (^{129}Xe). RMN HP). Il a été montré que la cristallisation commence à des stades de synthèse bien antérieurs à ceux observés par d'autres techniques classiques (XRD, SEM, adsorption de N_2 ...). La première SBU semble être les prismes hexagonaux, avant les cages sodalite, qui forment rapidement un environnement confiné puis des supercages. De plus, il a été démontré par RMN ^{129}Xe HP et 2D EXSY que la zéolithe nano-faujasite présente des cages sodalite ouvertes et une structure plus souple que dans la zéolite de type micro-faujasite. (ii) La seconde étude est une recherche sur les phénomènes de recristallisation survenant au cours du processus de hiérarchisation de la zéolithe et qui pourrait expliquer la distribution homogène des tailles de mésopores. Comme résultat remarquable, il a été montré dans ce travail que lors de la hiérarchisation de la zéolithe bêta avec le TPAOH, la recristallisation conduisait à la formation de minuscules particules de MFI, formées à la surface des mésopores (RMN ^{1}H MAS, RMN ^{129}Xe HP et 2D EXSY).

Key words: Zeolithes, Porosité, Structure, RMN à l'état solide, RMN du ^{129}Xe, hyperpolarisation, 2D EXSY.

Abstract:
The zeolites are 'molecular sieves' known for their numerous applications in adsorption, ion exchange, and catalysis. In this thesis, we focused on the study of some questions related to zeolite synthesis and post-synthesis, which are not yet resolved by other techniques.
NMR was the primary tool in this work, as it gives access to local structural information on nanocrystals even when diffraction techniques found their limits. NMR can also be used to study porosity using probe molecules adsorption, and in particular, xenon is known as a good molecule for this purpose. Indeed, the isotope ^{129}Xe can be hyperpolarized to increase the detection sensitivity, and interestingly it presents a wide chemical shift range depending on its confinement and thus the porosity of studied material.
Two studies are reported in this manuscript: (i) In the first study, the initial steps during the crystallization of nano-faujasite (FAU) type materials were investigated using classical NMR (mainly by ^{29}Si and ^{23}Na MAS NMR) and advanced NMR (^{129}Xe HP NMR). It was shown that crystallization starts at much earlier synthesis stages than those observed by other classical techniques (XRD, SEM, N_2 adsorption…). The first SBU seems to be the hexagonal prisms, prior to the sodalite cages, which rapidly form confined environment and then supercages. Moreover, it has been proved by ^{129}Xe HP NMR and 2D EXSY that nano-faujasite zeolite presents opened sodalite cages and a more flexible structure than in micro-faujasite zeolite.
(ii) The second study is an investigation on the recrystallization phenomena occurring during hierarchization process of zeolite and which could explain the homogenous distribution of the mesopore sizes. As a remarkable result, it has been shown in this work that during the hierarchization of beta zeolite with TPAOH, the recrystallization lead to the formation of tiny MFI particles, formed at the surface of the mesopores (^{1}H MAS NMR, ^{129}Xe HP NMR and 2D EXSY).

Key words: Zeolite, Porosity, Structure, Solid-state NMR, ^{129}Xe NMR, hyperpolarization, 2D EXSY.

Résumé:
Les zéolites sont des «tamis moléculaires» connus pour leurs nombreuses applications en adsorption, échange d'ions et catalyse. Dans cette thèse, nous nous sommes concentrés sur l'étude de quelques questions liées à la synthèse et à la post-synthèse de la zéolithe, qui ne sont pas encore résolues par d'autres techniques.
La RMN a été l'outil principal dans ce travail, donnant accès à des informations structurales locales sur les nanocristaux même lorsque les techniques de diffraction trouvent leurs limites. Elle peut également être utilisée pour étudier la porosité en utilisant l'adsorption de molécules sondes, et en particulier, le xénon est connu comme une bonne molécule pour cet objectif. En effet, l'isotope ^{129}Xe peut être hyperpolarisé pour augmenter la sensibilité de détection, et il présente une large plage de déplacement chimique en fonction du confinement et donc de la porosité du matériau étudié.
(I) Dans la première étude, les étapes initiales de la cristallisation de nano-faujasite (FAU) ont été étudiées en utilisant la RMN classique (principalement par ^{29}Si et ^{23}Na MAS RMN) et la RMN avancée (^{129}Xe). RMN HP). Il a été montré que la cristallisation commence à des stades de synthèse bien antérieurs à ceux observés par d'autres techniques classiques (XRD, SEM, adsorption de N_2 ...). La première SBU semble être les prismes hexagonaux, avant les cages sodalite, qui forment rapidement un environnement confiné puis des supercages. De plus, il a été démontré par RMN ^{129}Xe HP et 2D EXSY que la zéolithe nano-faujasite présente des cages sodalite ouvertes et une structure plus souple que dans la zéolite de type micro-faujasite.
(ii) La seconde étude est une recherche sur les phénomènes de recristallisation survenant au cours du processus de hiérarchisation de la zéolithe et qui pourrait expliquer la distribution homogène des tailles de mésopores. Comme résultat remarquable, il a été montré dans ce travail que lors de la hiérarchisation de la zéolithe bêta avec le TPAOH, la recristallisation conduisait à la formation de minuscules particules de MFI, formées à la surface des mésopores (RMN ^{1}H MAS, RMN ^{129}Xe HP et 2D EXSY).

Mots clés: Zéolithes, Porosité, Structure, RMN à l'état solide, RMN du ^{129}Xe, hyperpolarisation, 2D EXSY.